A theoretical study on the effect of curvature on near-field radiative transfer

Karthik Sasihithlu

Submitted in partial fulfillment of the
requirements for the degree
of Doctor of Philosophy
in the Graduate School of Arts and Sciences

COLUMBIA UNIVERSITY

2014

ABSTRACT

A theoretical study on the effect of curvature on near-field radiative transfer

Karthik Sasihithlu

The dissertation focuses on the theoretical analysis of near-field electromagnetic wave effects in thermal radiative transfer i.e. wave effects like interference, diffraction, and tunneling effects, that become important when analyzing energy transfer via electromagnetic waves over sub-wavelength distances. In particular, the focus will be on the enhanced thermal radiative transfer between bodies made of polar dielectric materials which support surface phonon polaritons (SPPs). When two such bodies are brought in close proximity to each other, the enhanced near-field radiation due to tunneling of SPPs can exceed the classical black body limit by several orders of magnitude. This enhanced radiation at nano-scale gaps finds applications in near-field thermophotovoltaics, heat assisted magnetic recording and near-field radiative cooling.

While the dependence of near-field radiative transfer on the gap between two planar objects is well understood, the effect of curvature on near-field radiative transfer is unclear. In particular, the relevance of an approximate method to predict the near-field interaction between curved bodies (called the proximity approximate method) is disputed. Hence, the computation of near-field radiative transfer between curved bodies, such as between two spherical bodies, become important. The existing method for computing near-field radiative transfer between two spheres is highly inefficient in probing small gaps where the near-field enhancement is most observed. The objective of this work is not only to simplify this computational framework which would enable us to probe smaller gaps and understand the effect of curvature on near-field radiative transfer better, but also to provide a method to

extend this to unequal sized spheres with large size disparities, so that comparison can be made with existing experimental measurements for near-field radiative transfer between a sphere and a plane.

In this regard a simplified form of vector translation addition theorem has been proposed which is valid for general near-field electromagnetic scattering problems. The range of validity of this approximation for the translation addition theorem has been discussed and recursion relations have been derived for computing the translation coefficients under this approximation. A method for normalizing the translation coefficients has also been proposed, and the computation of these normalized translation coefficients has been shown to depend only on ratios of successive orders of Bessel and Hankel functions which are computationally inexpensive. An analysis of the dependence of normalized translation coefficients on the size ratio of the two spheres has allowed us to extend the computation of near-field radiative transfer calculations to spheres with large size disparities.

Based on the computations, I have shown that the surface phonon polariton mediated radiative transfer between two spheres of effective radius $R = (R_1 R_2)/(R_1 + R_2)$, where R_1 and R_2 are the radii of the individual spheres, and minimum gap d scales as R/d as the non-dimensional gap $d/R \to 0$. I have proposed a modified form of proximity approximation to satisfy the continuity requirement between far-field and near-field radiative transfer between the spheres. The validity of this modified form of proximity approximation at different frequencies has also been discussed. This method can be applied to approximate the near-field radiative transfer between, not just spherical surfaces, but other general curved surfaces such as between cylindrical or conical surfaces.

Table of Contents

List of Figures

Acknowledgments

Sometime during my undergraduate years at NITK Surathkal, I started harboring ambitions of pursuing a research career in the basic sciences. However, having chosen to opt for a degree in Mechanical engineering, I felt I had a long shot at realizing this without significantly altering my academic track. To my good fortune, I got admitted to the graduate program in the Mechanical engineering department at Columbia University where a strong emphasis is placed on interdisciplinary research. However, due to lack of opportunities back then, I very nearly had to shelve my plans for a Ph.D. and instead look for a job after getting my M.S. degree. It was at this crucial (and perhaps even dire) stage that Prof. Arvind Narayanaswamy agreed to give me an opportunity to work under him towards a Ph.D. I am deeply indebted to him for providing me with a path to realize my dreams and reposing faith in me. I've thoroughly enjoyed my stint in his group, which, looking back I realize how lucky I have been to say this. His guidance, numerous discussions and the arguments I've had with him, and the joy and satisfaction in seeing some of my ideas bear fruition probably have a large part to do with this. Credit also goes to my colleagues: Carlo, Ning, Yi, and over the last year, Jeff, for maintaining a friendly atmosphere in the lab. These things become crucial especially when staying so far away from family and home.

My experience at Columbia University and New York has contributed to my growth, both personally and academically, far more than I imagined. I sincerely hope that this experience has given me a foundation for a successful career in research. Finally, I cannot thank my parents enough for supporting me all through.

Part I

Introduction

Chapter 1

Introduction

Thermal radiation can be considered to be a fluctuating electromagnetic field arising from spontaneous energy state transitions of particles of matter (molecules, atoms, ions, and electrons) [1; 2]. These spontaneous transitions can be viewed as charge fluctuations due to thermal energy in the material. The emitted radiation energy encompasses a broad range of wavelengths and has a continuous spectrum with the peak of the distribution determined by the temperature of the body. Due to the intimate relationship between the emitted radiation from a body and its physical-chemical characteristics, the study of thermal radiation has attained primary significance. By analyzing the emitted thermal radiation one can infer the characteristics of the constituents in the object using the fact that different elements in the environment absorb and emit very specific wavelengths of radiation as was first shown by Gustav Kirchhoff in 1860 (some credit it to Ångström) [3]. The condition under which the emitted/absorbed radiation would be independent of its chemical characteristics was also first postulated by him. Such a radiation was termed 'blackbody radiation'. Some of the other early works that led to important developments of the field of thermal radiative transfer includes that by Josef Stefan [4] who, on the basis of previous experimental measurements, showed that the power radiated by a blackbody is proportional to the fourth power of its absolute temperature. Further characteristics of this blackbody radiation were analyzed by Wilhelm Wein who in 1893 showed that the peak of the radiation shifted towards smaller

wavelengths with increasing temperature. He also showed that the spectral radiative energy should be a function of the form $f(\nu/T)$, i.e, the radiation at any specific frequency would depend only on the temperature of the body. The form of this function, which is valid for any frequency and temperature, was first found out by Max Planck in 1901 [5] who introduced the new idea of "quanta of light" to arrive at it, as opposed to the classical concepts with which it was being analyzed till then.

The analysis of thermal radiative energy transfer can be pursued from the viewpoint of classical electromagnetic theory using Maxwell's equations or using quantum theory. While the *propagation* of thermal radiation can be explained using electromagnetic wave theory, the description of emission and absorption of radiation from matter requires the use of quantum theory. When the length scales of energy transport are much larger than the wavelength of radiation, the description of energy transport via electromagnetic waves can be further simplified as it can be analyzed in the realm of geometric optics wherein the waves are described as collection of rays carrying energy in a small volume associated with a solid angle in the direction of rays. However, when the length scales are comparable to the wavelength of radiation, in order to take into account wave effects like interference, diffraction, and tunneling of waves, the energy transport has to be necessarily analyzed using electromagnetic wave theory. In particular, when two objects with dissipative electromagnetic properties given by the dielectric function, are brought in close proximity to each other, a characteristic gap dependence in radiative transfer is observed which can only be obtained theoretically by using an electrodynamic basis for radiative transfer theory. This effect has gained all the more prominence since it has been proven experimentally that for small gaps the radiative heat transfer increases beyond Planck's blackbody limit by several orders of magnitude [6; 7; 8]. This behavior, which is of primary motivation for this work, has been explained in more detail in the ensuing paragraph.

Consider two planar black surfaces at temperatures T_A and T_B separated by a gap d in vacuum which exchange energy at the rate of $\dot{Q}$ Wm^{-2}. According to Stefan's law $\dot{Q}$ is given

by:

$$\dot{Q} = \frac{\pi^2 k_B^4}{60\hbar^3 c^2}(T_A^4 - T_B^4) \tag{1.1}$$

where k_B is the Boltzmann's constant, $\hbar$ is the Planck's constant divided by 2π and c is the velocity of light in free space. This, as we notice, is independent of the gap d between them. However, as shown in Fig. 1.1, at the interface between any object and vacuum there are evanescent modes present which decay exponentially from the surface. When two such surfaces are brought close enough, energy gets exchanged from one body to another via photon tunneling through these evanescent modes. For closely spaced objects separated by vacuum (these situations arise frequently in miniature devices such as between head and a writing disk in a hard drive [9], or in scanning tunneling microscopes [10]) the contribution via photon tunneling can be the dominant form of photonic energy transfer. This phenomenon of the spacing dependence in radiative transfer has been experimental verified using different configurations like (1) between two planar surfaces [11; 12; 13; 14], (2) scanning probe tip and planar surface [15; 10; 16; 17], and (3) between a microsphere and a planar surface [18; 19; 20; 21; 22].

Earliest theoretical analysis of the gap dependence in the radiative transfer between two identical flat surfaces of arbitrary material was pursued in 1967 by Cravalho et al. [23]. They analyzed radiative transfer using electromagnetic theory to take into account the wave interference and tunneling effects and modified the expression for time averaged flux of blackbody radiation to arrive at an expression for the gap-dependent radiative transfer. However, the number of modes that they included in their analysis of radiative transfer via wave tunneling was limited to $n\omega/c$ where n is the refractive index of the two surfaces (taken to be real). Polder and Van Hove [24] in 1971, for the first time, analyzed the radiative energy transfer between two closely spaced identical flat surfaces of arbitrary properties by employing principles of fluctuational electrodynamics developed by Rytov [2]. By using the fluctuation-dissipation theorem (discussed in Chapter 2) they were able to deal with the actual source of the radiation - fluctuation currents in the body. However, they presented their results only for metallic bodies, as did Loomis and Maris [25] who showed that the

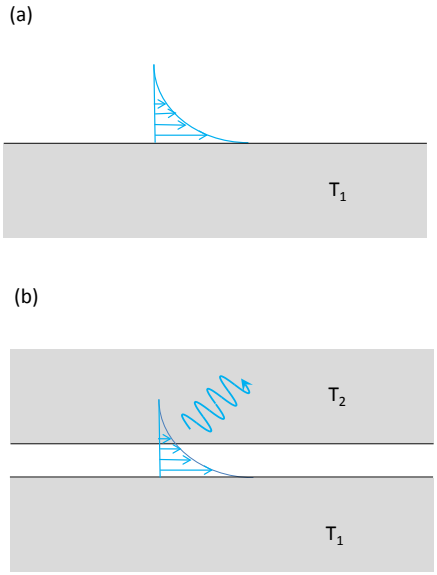

Figure 1.1: (a) Evanescent waves exist at the interface between a metal/dielectric and vacuum with decay length approximately $\lambda/2$ (b) When another metal/dielectric surface at a different temperature is brought in close proximity to this interface, energy gets transferred via tunneling of these evanescent modes. T_1 and T_2 denote the different temperatures of two bodies.

radiative transfer between metallic bodies due to evanescent waves varies as $1/l^2$ (for small gaps) where l is the spacing between the metallic structures. This work was extended to dielectric surfaces that support surface phonon polaritons by Mulet et al. [26] where the contribution from such surface waves was shown to greatly enhance the radiative transfer between polar dielectrics. Some of the most recent theoretical works extend this formulation to study the behavior of near-field radiative transfer between planar structures of other materials like that between two metamaterials [27; 28], anisotropic materials [29; 30], and the influence of surface roughness characteristics [31].

Other than planar structures there have also been studies of the behavior of near-field radiative transfer between bodies of other geometrical shapes like that between two dipoles [32; 33], between a dipole and a flat surface [34; 35] and recently to other more experimentally feasible geometries such as between two micro spheres [36] and between a micro sphere and a planar surface [37; 38]. The theoretical method developed in [36] was based on computations of spherical Bessel and Hankel functions which lead to numbers too large or too small for a given floating point format on a computer. This posed severe restraints in the analysis of near-field radiative transfer for small gaps where the near-field enhancement is most visible. Gaps up to $d/R = 0.01$ were analyzed for two equal sized spheres of radius R and compared with proximity approximation theory (details of the proximity approximation method will be given in subsequent chapters). In addition, while in principle the theory could be extended to spheres of any sizes, computational analysis could only be performed between two similarly sized spheres. The method to calculate the near-field radiative transfer between a sphere and a plane [37; 38] has been developed similar to that outlined for two spheres in [36] except that in place of an expansion technique based on vector spherical waves, a combination of spherical and cylindrical waves are used in Ref. [37] and a combination of spherical and planar waves are used in Ref. [38] (but with a one-reflection approximation). Based on these computations, the predictions from the proximity approximation method was compared with and it was concluded that the proximity approximation method does not hold true in Ref. [37] but it was found to be relevant in Ref. [38]. The

formalism for computing radiative transfer between arbitrary bodies has also been detailed in several recent publications. Kruger et al. [38] arrived at an expression for the autocorrelation function of the electric field outside an arrangement of arbitrary number of objects in terms of their individual scattering properties, from which the net energy radiated from the objects can be found out. However the computation of scattering properties of bodies with arbitrary shape was not addressed and for demonstration purposes simple geometries for which the correlation function can be obtained through expansion of fields using appropriate geometry-dependent basis functions was shown. A similar problem of analyzing radiative energy exchange among arbitrary bodies at different temperatures was considered by Ben-Abdallah et al. [39] but under the dipole approximation. Messina and Antezza [40] arrived at an expression for radiative heat transfer exchange between two bodies of arbitrary shape and dielectric properties in terms of the bodies' scattering matrices. By assuming that the bodies are enclosed by planar strips they were able to use a plane-wave expansion of the electric and magnetic fields. A different approach was taken by Rodriguez et al. [41] who formulated the radiative heat transfer between bodies of arbitrary shape in terms of surface currents located on the interfaces of the objects. By doing so, it enabled them to use efficient boundary-element method techniques to arrive at solutions for bodies with complicated geometries. Applying this method for the two-sphere configuration, data was presented for radius $R = 0.2\,\mu$m and for separation gaps of order $d \approx R$. It should be pointed out that approaches specialized for certain geometries such as those developed in [36; 37] are expected to outperform such a generic approach as developed in [41] when applied to these specific geometries. A similar surface-integral-equation approach for arriving at an expression for energy and momentum transfer between arbitrarily shaped bodies was also detailed in [42].

1.1 Motivation and outline of thesis

The primary aim of this work is to further the understanding of near-field effects in radiative transfer when two objects exchanging radiation are placed in close proximity to each

other. Some of the areas where such near-field effects become important are in thermal photovoltaics [43; 44; 45; 46], thermal rectification devices [47], nanopatterning [48], thermally assisted magnetic recording [9], thermal imaging [49] and noncontact radiative cooling [50]. In particular, I have analyzed the role of curvature in near-field radiative transfer and the relevance of proximity approximation in estimating the radiative transfer between curved bodies. This has been accomplished by: (a) arriving at simplifications to the computational method for determining near-field radiative transfer between two spheres given in Ref. [36] and using these simplifications to compute the radiative transfer between two equal sized spheres at gaps smaller than those published in literature, (b) proposing and verifying a modification to the proximity approximation method to ensure continuity between near-field and far-field radiative transfer between two spheres, (c) highlighting the dependence of near-field radiative transfer on the relevant spatial parameters in the problem, (d) enable extension of the computations to the case of unequal sized spheres with large size disparities.

Understanding the near-field effects in radiative transfer has another important consequence. The analysis of near-field forces between objects (like Casimir force and van der Waals force) can be split into a temperature dependent part (from fluctuation of charges due to thermal energy) and a temperature independent part (from fluctuation of charges in their ground states; also called as zero-point fluctuations). The temperature dependent part, which has the same origin as the near-field radiative energy transfer, is much smaller than that due to zero-point fluctuations at room temperature, and hence difficult to measure experimentally. Hence a study of the near-field radiative energy transfer between the objects would also throw light on the behavior of the temperature dependent part of the near-field forces as well.

The dissertation has been organized as follows : In Chapter 2 the fundamentals of near-field radiative transfer which are relevant to this work are explained briefly and references which expound on these concepts are listed. In Chapter 3, the method for computing radiative transfer between spherical bodies is explained. In particular, the equations in Ref. [36] have been explained in greater detail and, wherever appropriate, the derivations are

shown. In Chapter 4, the basics of translation addition theorem, which is central to this work, are presented and a method to normalize the translation coefficients is explained. Recursion relations for the normalized translation coefficients, which are necessary for efficient computation of the translation coefficients, are derived. In Chapter 5, a simplified form of the translation addition theorem is derived which is valid in the limit $d \ll R_1, R_2$. Here, d is the minimum surface to surface gap between the two spheres and R_1, R_2 are the radii of the two spheres. In Chapter 6, the behavior of the normalized translation coefficients with varying radius ratio R_2/R_1 is analyzed and a method which takes advantage of this behavior to compute near-field radiative transfer between two unequal sized spheres with large size disparities is explained. In Chapter 7, the convergence criterion for the vector eigenfunction expansion of the electromagnetic field while computing the near-field radiative transfer is derived and the role of the translation theorem in attaining this convergence is detailed. Using the simplifications detailed in Chapters 4, 5 and 6, the near-field radiative transfer between (a) two equal spheres and (b) two unequal sized spheres are calculated and the results are presented and analyzed in Chapter 8. The difference in the spatial dependence of the far-field and the near-field radiative transfer is highlighted. In Chapter 9, the proximity approximation theory is introduced and the need for modification of this theory for the case of near-field radiative transfer between two finite objects (like that between two spheres) is explained. In the end the main contributions of this work has been summarized and possible future work has been listed.

Chapter 2

Fundamentals of near-field radiative transfer

2.1 Basics of electromagnetism

Electric and magnetic fields are produced by charges. Maxwell's equations describe quantitatively how charges act as sources of electric and magnetic fields. The differential form of Maxwell's equations is given by:

$$\boldsymbol{\nabla} \cdot \boldsymbol{E} = \rho/\varepsilon_0 \tag{2.1}$$

$$\boldsymbol{\nabla} \cdot \boldsymbol{B} = 0 \tag{2.2}$$

$$\boldsymbol{\nabla} \times \boldsymbol{E} = -\frac{\partial \boldsymbol{B}}{\partial t} \tag{2.3}$$

$$\boldsymbol{\nabla} \times \boldsymbol{B} = \mu_0 \boldsymbol{J} + \frac{1}{c^2}\frac{\partial \boldsymbol{E}}{\partial t} \tag{2.4}$$

The quantities ρ and $\boldsymbol{J}$ represent the total charge and total current in the medium; ε_0 and μ_0 are the electric permittivity and magnetic permeability of free space; c is the velocity of light in vacuum and given by $c = 1/\sqrt{\mu_0 \varepsilon_0}$. When dealing with wave propagation in a medium, it is useful to rewrite the Maxwell's equations in terms of the fields $\boldsymbol{D}$ and $\boldsymbol{H}$ where $\boldsymbol{D}$ and

$\boldsymbol{H}$ are given by the constitutive equations:

$$\boldsymbol{D} = \varepsilon_0 \boldsymbol{E} + \boldsymbol{P}_{\text{field}} \tag{2.5}$$

$$\boldsymbol{H} = \boldsymbol{B}/\mu_0 + \boldsymbol{M}_{\text{field}} \tag{2.6}$$

with the fields $\boldsymbol{P}_{\text{field}}$ and $\boldsymbol{M}_{\text{field}}$ representing the polarization and the magnetization fields respectively. This enables us to describe the fields using just the free charges in the medium. The Maxwell's equations in terms of the fields $\boldsymbol{D}$ and $\boldsymbol{H}$ can be written as:

$$\boldsymbol{\nabla} \cdot \boldsymbol{D} = \rho_{\text{free}} \tag{2.7}$$

$$\boldsymbol{\nabla} \cdot \boldsymbol{B} = 0 \tag{2.8}$$

$$\boldsymbol{\nabla} \times \boldsymbol{E} = -\frac{\partial \boldsymbol{B}}{\partial t} \tag{2.9}$$

$$\boldsymbol{\nabla} \times \boldsymbol{H} = \boldsymbol{J}_{\text{free}} + \frac{\partial \boldsymbol{D}}{\partial t} \tag{2.10}$$

where, ρ_{free} and $\boldsymbol{J}_{\text{free}}$ denote the source terms due to free charges. For waves propagating in vacuum, $\rho_{\text{free}} = \boldsymbol{J}_{\text{free}} = 0$.

The polarization field $\boldsymbol{P}_{\text{field}}$ can be related to the electric field $\boldsymbol{E}$ using $\boldsymbol{P}_{\text{field}} = \varepsilon_0 \chi_e \boldsymbol{E}$, where χ_e denotes the susceptibility of the medium to get polarized by the electric field $\boldsymbol{E}$. Using this we can express the displacement field $\boldsymbol{D}$ in Eq. 2.5 in terms of $\boldsymbol{E}$ as: $\boldsymbol{D} = \varepsilon \boldsymbol{E}$, where $\varepsilon = \varepsilon_0 \varepsilon_r$ with ε_r representing the relative permittivity or the dielectric function of the medium and related to χ_e as: $\varepsilon_r = 1 + \chi_e$. The materials chosen in this work are assumed to be non-magnetic, so that we have $\boldsymbol{B} = \mu_0 \boldsymbol{H}$.

For time harmonic fields $\boldsymbol{E}(\boldsymbol{x}, t) = \text{Re}[\hat{\boldsymbol{E}}(\boldsymbol{x}) e^{i\omega t}]$ and $\boldsymbol{B}(\boldsymbol{x}, t) = \text{Re}[\hat{\boldsymbol{B}}(\boldsymbol{x}) e^{i\omega t}]$, the Maxwell's equations can then be written as:

$$\boldsymbol{\nabla} \cdot \hat{\boldsymbol{D}} = \rho_{\text{free}} \tag{2.11}$$

$$\boldsymbol{\nabla} \cdot \hat{\boldsymbol{B}} = 0 \tag{2.12}$$

$$\boldsymbol{\nabla} \times \hat{\boldsymbol{E}} = -i\omega \hat{\boldsymbol{B}} \tag{2.13}$$

$$\boldsymbol{\nabla} \times \hat{\boldsymbol{H}} = \boldsymbol{J}_{\text{free}} + i\omega \hat{\boldsymbol{D}} \tag{2.14}$$

The hat notation ' $\hat{}$ ' has been dropped from the following equations, recognizing that we will be dealing with only time harmonic fields in this work. In vacuum (where $\rho_{\text{free}}, \boldsymbol{J}_{\text{free}} = 0$, $\mu = \mu_0$, $\varepsilon = \varepsilon_0$), combining Eq. 2.13 and Eq. 2.14 gives us the vector wave equation:

$$\boldsymbol{\nabla} \times \boldsymbol{\nabla} \times \boldsymbol{X}(\boldsymbol{r}, \omega) - k^2 \boldsymbol{X}(\boldsymbol{r}, \omega) = 0 \tag{2.15}$$

where, $\boldsymbol{X}(\boldsymbol{r}, \omega)$ can be either the electric or the magnetic field at position vector $\boldsymbol{r}$ and k is the wave propagation constant given by $k = \omega/c$. The independent divergence-free solutions of the vector wave equation in spherical coordinates are given by [36; 51; 52]:

$$\boldsymbol{M}_{nm}^{(p)}(k\boldsymbol{r}) = z_n^{(p)}(kr)\boldsymbol{V}_{nm}^{(2)}(\theta, \phi) \tag{2.16}$$

$$\boldsymbol{N}_{nm}^{(p)}(k\boldsymbol{r}) = \zeta_n^{(p)}(kr)\boldsymbol{V}_{nm}^{(3)}(\theta, \phi) + \frac{z_n^{(p)}(kr)}{kr}\sqrt{n(n+1)}\boldsymbol{V}_{nm}^{(1)}(\theta, \phi) \tag{2.17}$$

where $\boldsymbol{M}_{nm}^{(p)}(k\boldsymbol{r})$ (not to be confused with the magnetization field in Eq. 2.6) and $\boldsymbol{N}_{nm}^{(p)}(k\boldsymbol{r})$ are vector spherical waves of order (n, m). n and m are integers. n can take values from 0 to ∞. For each n, $|m| \leq n$. The superscript p refers to the radial behavior of the waves. For $p = 1$, the $\boldsymbol{M}$ and $\boldsymbol{N}$ waves are regular waves and remain finite at the origin and $z_n^{(1)}(kr)$ is the spherical Bessel function of order n. For $p = 3$, the $\boldsymbol{M}$ and $\boldsymbol{N}$ waves are outgoing spherical waves that are singular at the origin and $z_n^{(3)}(kr)$ is the spherical Hankel function of the first kind of order n. The radial function $\zeta_n^{(p)}(x) = \frac{1}{x}\frac{d}{dx}\left(xz_n^{(p)}(x)\right)$. $\boldsymbol{V}_{nm}^{(1)}(\theta, \phi)$, $\boldsymbol{V}_{nm}^{(2)}(\theta, \phi)$, and $\boldsymbol{V}_{nm}^{(3)}(\theta, \phi)$ are vector spherical harmonics of order (n, m) and are given by:

$$\boldsymbol{V}_{nm}^{(1)}(\theta, \phi) = \hat{\boldsymbol{r}} Y_{nm} \tag{2.18a}$$

$$\boldsymbol{V}_{nm}^{(2)}(\theta, \phi) = \frac{1}{\sqrt{n(n+1)}}\left(-\hat{\boldsymbol{\phi}}\frac{\partial Y_{nm}}{\partial \theta} + \hat{\boldsymbol{\theta}}\frac{im}{sin\theta}Y_{nm}\right) \tag{2.18b}$$

$$\boldsymbol{V}_{nm}^{(3)}(\theta, \phi) = \frac{1}{\sqrt{n(n+1)}}\left(\hat{\boldsymbol{\theta}}\frac{\partial Y_{nm}}{\partial \theta} + \hat{\boldsymbol{\phi}}\frac{im}{sin\theta}Y_{nm}\right) \tag{2.18c}$$

The vector spherical waves $\boldsymbol{M}$ and $\boldsymbol{N}$ given in Eq. 2.16 and Eq. 2.17 are mutually orthogonal and are related to each other as: $\boldsymbol{\nabla} \times \boldsymbol{M} = k\boldsymbol{N}$. They also form a complete set.

Hence any solution to the vector wave equation can be expanded in an infinite series of $\boldsymbol{M}$ and $\boldsymbol{N}$ waves as [51; 52; 53]:

$$\boldsymbol{E}(\boldsymbol{r}) = \sum_{\substack{m=-n \\ n=1}}^{\substack{n=\infty \\ m=n}} \left[A_{nm}^{(p)} \boldsymbol{M}_{nm}^{(p)}(k\boldsymbol{r}) + B_{nm}^{(p)} \boldsymbol{N}_{nm}^{(p)}(k\boldsymbol{r}) \right] \tag{2.19}$$

$$\boldsymbol{H}(\boldsymbol{r}) = \frac{ik}{\omega\mu} \sum_{\substack{m=-n \\ n=1}}^{\substack{n=\infty \\ m=n}} \left[A_{nm}^{(p)} \boldsymbol{N}_{nm}^{(p)}(k\boldsymbol{r}) + B_{nm}^{(p)} \boldsymbol{M}_{nm}^{(p)}(k\boldsymbol{r}) \right] \tag{2.20}$$

where, $A_{nm}^{(p)}$, $B_{nm}^{(p)}$ are coefficients which are found from boundary conditions.

An alternate but equivalent definition for the $\boldsymbol{M}$ and $\boldsymbol{N}$ waves in terms of the solutions of the scalar Helmholtz equation is given in Chapter 4. Apart from $\boldsymbol{M}$ and $\boldsymbol{N}$ there is one more solution to the vector Helmholtz equation (i.e. a possible solution to the Maxwell's equations) given by:

$$\boldsymbol{L}_{nm}^{(p)}(k\boldsymbol{r}) = \boldsymbol{r} Y_{nm} z_n^{(p)}(kr) \tag{2.21}$$

If we have to satisfy $\boldsymbol{\nabla} \cdot \boldsymbol{E} = 0$, which is the case in source free regions, then $\boldsymbol{L}$ need not be used since this cannot contribute to a divergence free solution. Only $\boldsymbol{M}$ and $\boldsymbol{N}$ are then used.

2.2 Optical properties of dielectric materials

The behavior of near-field radiative transfer between two closely spaced bodies is dependent on the material properties of the two objects. In particular, for polar dielectrics like SiO_2 (which is the material chosen for much of the study), SiC, and BN, the presence of resonances in the dielectric function of the material has a large influence on the near-field radiative transfer. The presence of resonances in the dielectric function of the material is described in this section using the Drude-Sommerfeld model of an electron [54]. It must be pointed out that this model for dielectric function has been used here for explanatory purposes only. For the computations, experimentally obtained values of the dielectric function of SiO_2, which are listed in Ref. [55], have been used.

Consider the motion of a bound electron with charge q under the action of an electric field $\boldsymbol{E}(t)$. The equation of motion for this can be modeled as a spring-mass-damper system given by:

$$m\left(\ddot{\boldsymbol{x}} + \Omega^2 \boldsymbol{x} + \Gamma \dot{\boldsymbol{x}}\right) = q\boldsymbol{E}(t) \tag{2.22}$$

Here, $m\Omega^2$ and $m\Gamma$ denote the spring constant and the damping coefficient respectively. In the Fourier space, denoting the Fourier transform of $\boldsymbol{x}(t)$ and $\boldsymbol{E}(t)$ by $\tilde{\boldsymbol{x}}(\omega)$ and $\tilde{\boldsymbol{E}}(\omega)$ respectively, Eq. 2.22 can be written as:

$$m\left(-\omega^2 + \Omega^2 - i\Gamma\omega\right)\tilde{\boldsymbol{x}}(\omega) = q\tilde{\boldsymbol{E}}(\omega) \tag{2.23}$$

The solution of this equation is given by:

$$\tilde{\boldsymbol{x}}(\omega) = \frac{q\tilde{\boldsymbol{E}}(\omega)}{m\left(\Omega^2 - \omega^2 - i\Gamma\omega\right)} \tag{2.24}$$

The dipole moment is given by $\tilde{\boldsymbol{p}} = q\tilde{\boldsymbol{x}}$ and if there are N typical electrons in unit volume, then we have total polarization $\tilde{\boldsymbol{P}}$ to be $\tilde{\boldsymbol{P}} = Nq\tilde{\boldsymbol{x}} = \varepsilon_0\chi_e\tilde{\boldsymbol{E}}$ where, the susceptibility $\chi_e(\omega)$ is given by:

$$\chi_e(\omega) = \frac{Nq^2}{\varepsilon_0 m}\frac{1}{\left(\Omega^2 - \omega^2 - i\Gamma\omega\right)} \tag{2.25}$$

The susceptibility $\chi_e(\omega)$ is a measure of the propensity of a medium to get polarized. $\chi_e(\omega)$ is related to the dielectric function or the relative permittivity of the medium as: $\varepsilon_r(\omega) = 1 + \chi_e(\omega)$. The permittivity $\varepsilon_r(\omega)$ is a measure of the extent to which the medium permits the electric field to enter into it. In a dielectric, polarization (dipoles) will act to reduce the electric field inside it. Since there are no molecules in vacuum to get polarized, it will allow the electric field to completely enter it. Hence for vacuum $\varepsilon_r(\omega) = 1$ and $\chi_e(\omega) = 0$. We can then write the expression for $\varepsilon_r(\omega)$ (replacing the term $\sqrt{\frac{Nq^2}{\varepsilon_0 m}}$, which denotes the plasma frequency of the material, by ω_p) as:

$$\varepsilon_r(\omega) = 1 + \frac{\omega_p^2}{\left(\Omega^2 - \omega^2 - i\Gamma\omega\right)} \tag{2.26}$$

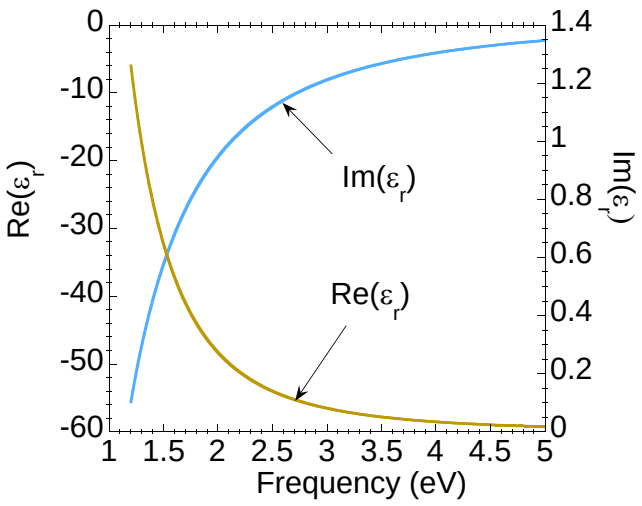

Figure 2.1: Real and imaginary part of the dielectric function from Eq. 2.26 as a function of ω over the visible and near-UV range.

To understand the behavior of the function ε_r with varying frequency ω, consider first the case where there is no restoring force ($\Omega = 0$), which is typically the case for a free-electron in a metal. Eq. 2.26 reduces to:

$$\varepsilon_r(\omega) = 1 - \frac{\omega_p^2}{(\omega^2 + i\Gamma\omega)} \tag{2.27}$$

The dielectric function given in Eq. 2.27 is plotted in Fig. 2.1 for the frequency range in visible and near-ultraviolet spectrum ($\approx$ 1.2 eV to 5 eV). The parameters ω_p and Γ are chosen to be 9.026 eV and 0.0267 eV (which are the parameters for gold [56]). The real part of the dielectric function is observed to be negative over the visible range which implies that the electric field is hardly able to penetrate the material. This is the reason why most metals are strong reflective in the visible frequency range. The imaginary part of the dielectric function is indicative of the dissipation of energy associated with the motion of electrons in metals.

Consider now the case when you introduce a restoring force into the oscillating electron model (Ω is finite). This is the case in dielectrics where the electrons are bound. The equation for the dielectric function in this case is given by Eq. 2.26. The dielectric function for such a model has been plotted in Fig. 2.2. When a restoring force is introduced, the presence

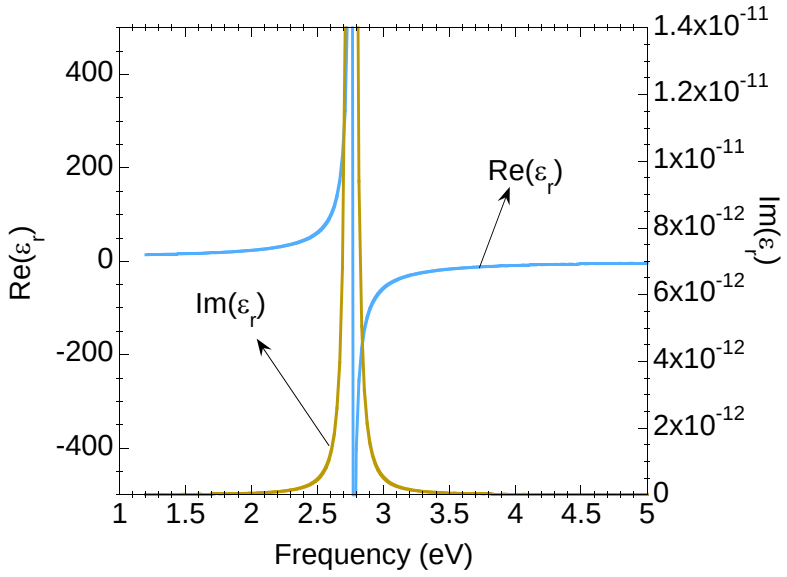

Figure 2.2: Real and Imaginary part of the dielectric function as a function of frequency over the visible range accounting for bound electrons; The parameters chosen are $\omega_p = 9.026$ eV, $\Gamma = 0.0267$ eV, and $\Omega = 2.7544$ eV

of the natural frequency of the spring-mass oscillator system introduces the possibility of resonance when the frequency of the exciting electric field ω is equal to the the natural frequency of the system Ω. This resonance behavior can be observed in Fig. 2.2. It must be mentioned that the model of dielectric function given in Eq. 2.26 has been chosen only to explain the presence of resonances in dielectric function of materials, since, such resonances are observed in the dielectric function of silica, which is the material used for the analysis of near-field radiative transfer between two spheres in this work. A more accurate model for the dielectric function, which includes contribution from other sources of polarization (inter-band electronic transitions, for example), can be obtained from Ref. [57].

The dielectric function of silica is plotted in Fig. 2.3 as a function of frequency in eV. The presence of resonance at two different frequencies can be observed, one at 0.061 eV and the other at 0.144 eV. These frequencies lie in the infra-red region which are ideal for enhancement of radiative energy transfer at room temperature (≈ 300 K).

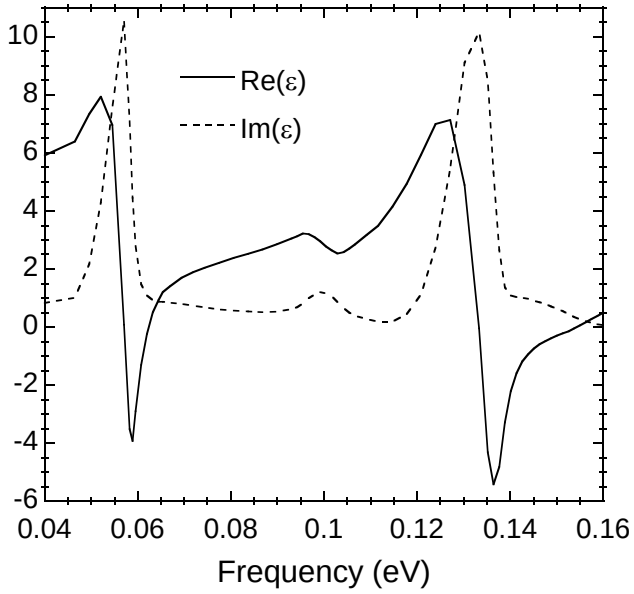

Figure 2.3: Real and Imaginary part of the dielectric function of silica as a function of frequency in eV.

2.3 Properties of surface-polaritons

As mentioned in Chapter 1, the enhancement in near-field radiative transfer between two polar dielectric surfaces is primarily from tunneling of surface polaritons which are confined at the interface with vacuum. Hence it would be of interest to understand the conditions under which surface polaritons exist and their properties. These are dealt with in this section. The explanation follows closely the description given in Ref. [57].

2.3.1 Necessary conditions for surface polaritons to exist in planar interfaces

Consider an interface between a medium with complex frequency dependent dielectric function $\varepsilon_1(\omega)$ and vacuum with dielectric function $\varepsilon_2(\omega) = 1$. The interface is chosen to coincide with the plane $z = 0$ of a Cartesian coordinate system, as indicated in Fig. 2.4. We are

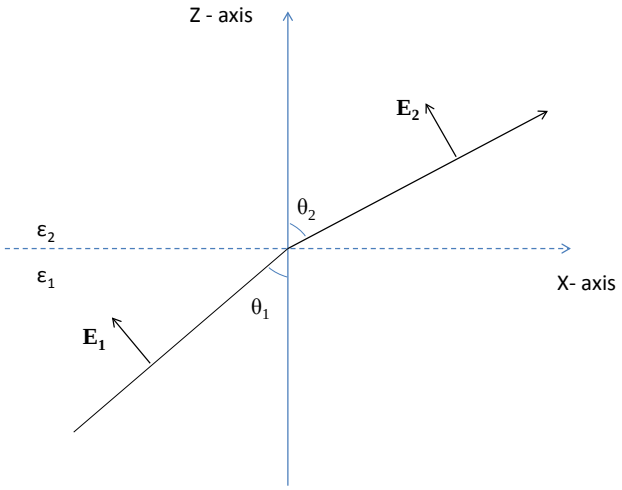

Figure 2.4: Interface between two medium with material characterized by dielectric function $\varepsilon_1(\omega)$ and $\varepsilon_2(\omega)$

primarily looking for homogeneous solutions of the Maxwell's wave equation (i.e those solutions of the wave equation that can exist on their own without external excitations) which are localized at the interface of the two-layered system. A field is localized at the interface when it exponentially decays on either side of the interface.

The wave equation is given by:

$$\boldsymbol{\nabla} \times \boldsymbol{\nabla} \times \boldsymbol{E}(\boldsymbol{r}, \omega) - \frac{\omega^2}{c^2} \varepsilon(\omega) \boldsymbol{E}(\boldsymbol{r}, \omega) = 0 \tag{2.28}$$

with $\varepsilon(\omega) = \varepsilon_1(\omega)$ when $z < 0$ and $\varepsilon(\omega) = \varepsilon_2(\omega)$ when $z > 0$. A transverse magnetic (TM or p-polarized) wave in the two media is represented by:

$$(E_{xi}\hat{\boldsymbol{x}} + E_{zi}\hat{\boldsymbol{z}}) e^{ik_x x + ik_{zi} z - i\omega t}; \;\; i = 1, 2 \tag{2.29}$$

where k_x and k_z denote the components of the wave propagation constant $k = \sqrt{\varepsilon(\omega)}\omega/c$ along the interface and along the z-axis respectively. Note that k_x does not change across a interface. No solution for localized modes exist for TE (s-polarized) waves [57]. For the field *inside* the two media we can write:

$$k_x^2 + k_{zi}^2 = \varepsilon_i \omega^2 / c^2; \;\; i = 1, 2 \tag{2.30}$$

Since the free-charge ρ_f inside the two media is zero, we also have $\boldsymbol{\nabla} \cdot \boldsymbol{D} = 0$ so that:

$$k_x E_{xi} + k_{zi} E_{zi} = 0; \;\; i = 1, 2 \tag{2.31}$$

The following boundary conditions have to be satisfied at the interface:

- Tangential field across the interface should be continuous

$$E_{x1} - E_{x2} = 0; \tag{2.32}$$

- Normal component of the displacement field should be continuous

$$\varepsilon_1 E_{z1} - \varepsilon_2 E_{z2} = 0; \tag{2.33}$$

Equations 2.31, 2.32, and 2.33 form a set of four homogeneous equations for the four unknowns E_{xi}, E_{zi}, $i = 1, 2$. A solution exists only if: $\dfrac{k_{z2}}{k_{z1}} = \dfrac{\varepsilon_2}{\varepsilon_1}$. Combining this with Eq. 2.30, we can solve for k_x which gives us the dispersion relation which relates the wave-vector in the propagation direction k_x to the frequency ω as:

$$k_x^2 = \frac{\varepsilon_1 \varepsilon_2}{\varepsilon_1 + \varepsilon_2} \frac{\omega^2}{c^2} \tag{2.34}$$

We can also solve for normal wave vector k_{zi} giving us:

$$k_{zi}^2 = \frac{\varepsilon_i^2}{\varepsilon_1 + \varepsilon_2} \frac{\omega^2}{c^2}; \;\; i = 1, 2 \tag{2.35}$$

The above discussion holds true for any eigenmode solution of the wave equation at the interface of two media. In particular, we need solutions that are localized at the interface of the media (i.e exponentially decaying in z-direction) and propagating in the x-direction. Therefore, ignoring losses in the medium [i.e. $\mathrm{Im}(\varepsilon_1) = 0$; when there are losses in the medium the radiating and confined modes cannot be as easily differentiated], we need k_x to be real and k_{zi} to be imaginary such that $\mathrm{Im}(k_{zi}) > 0$ [< 0] for $z > 0$ [< 0]. Since $\varepsilon_2 = 1$, both these conditions are satisfied in Eq. 2.34 and 2.35 when:

$$\varepsilon_1(\omega) < -1 \tag{2.36}$$

Referring to the plot of dielectric function of silica shown in Fig. 2.3 we observe that there are two frequency bands where the real part of the dielectric function satisfies Eq. 2.36 and hence can support surface modes.

2.3.2 Dispersion relation for surface polaritons

From Eq. 2.34 the dispersion relation for a SiC - vacuum interface is given by:

$$k_x = \frac{\omega}{c}\sqrt{\frac{\varepsilon_1(\omega)}{\varepsilon_1(\omega)+1}} \tag{2.37}$$

To plot the dispersion relation, we ignore losses and use only the real part of the dielectric function of SiC in Eq. 2.37. Figure 2.5(a), which shows the dispersion curve for the SiC-vacuum interface, and Figure 2.5(b), which shows the plot of real part of the dielectric function of SiC, have been borrowed from Ref. [58] with permission. We note the following from Eq. 2.37: when $\varepsilon_1 \gg 1$ then $k_x \approx \frac{\omega}{c}$ which is termed as the light-line in Fig. 2.5(a). Significant deviation from the light line will be observed only when $\varepsilon_1 \to -1$. When $0 > \varepsilon_1 > -1$, then k_x is imaginary and hence cannot be shown on the dispersion curve. The frequency where $\varepsilon_1 = 0$ is termed the longitudinal optical mode and denoted by ω_{LO}. The natural frequency in the Drude model of the dielectric function of SiC is termed the transverse optical mode ω_{TO} and the frequency where $\varepsilon_1 = -1$ is indicated by ω_{res} in the figure. We observe that there are two branches in the dispersion curve, a higher frequency (or energy) one corresponding to $\omega > \omega_{LO}$ and a lower frequency one corresponding to $\omega < \omega_{TO}$. Since for the higher frequency curve, $k_x < \omega/c$ these correspond to propagating waves. The lower energy curve corresponds to confined surface waves.

From the dispersion curve for the surface phonon polariton, it is clear that it is possible for modes with large values of k_x to exist on the surface of the SiC-vacuum interface for frequencies close to ω_{res}. The physical reason for the increased momentum (represented by k_x) can be understood from Heisenberg's uncertainty principle: since we are confining the wave to the surface, the momentum has to naturally increase. When two SiC surfaces are brought in proximity to each other, energy gets transferred from one surface to another via tunneling of these modes. This is the reason why we observe a large increase in radiative heat transfer when two polar-dielectric surfaces separated by vacuum are brought in close proximity to each other [34].

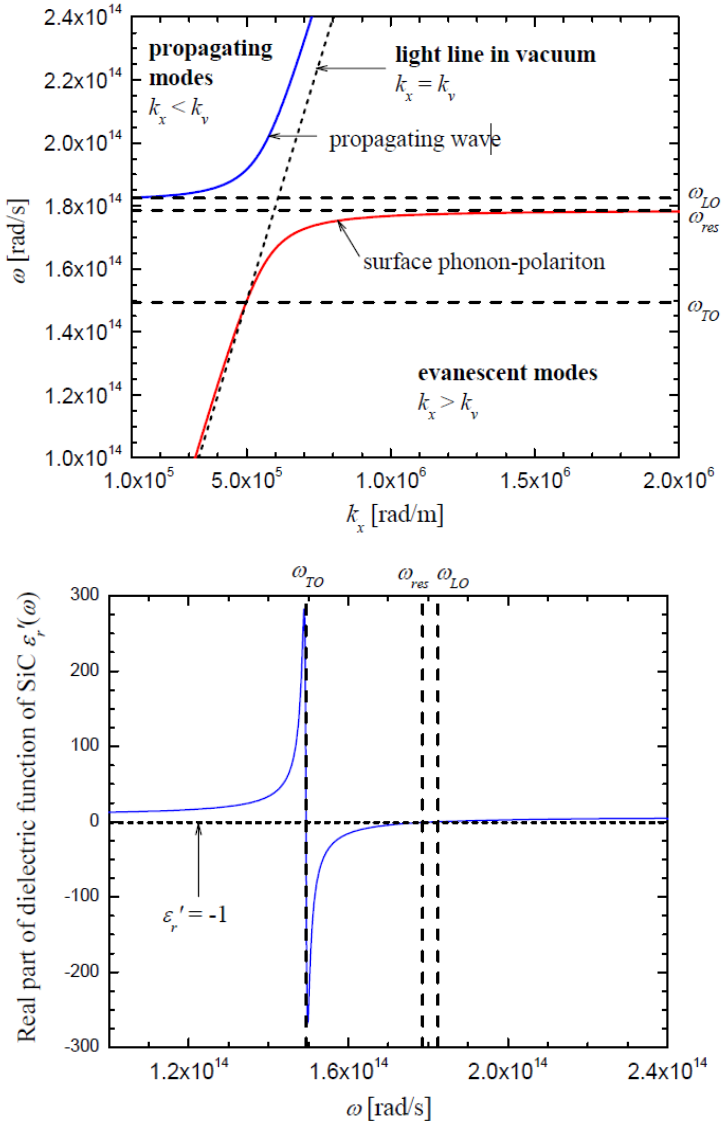

Figure 2.5: **(a)** Dispersion curve for SiC-Vacuum system. Here $k_v = \omega/c$ **(b)** Plot of real part of dielectric function of SiC. The figures have been borrowed from Ref. [58] with permission.

2.4 Green's functions

The primary purpose of employing Green's functions is to get a solution for inhomogeneous boundary value problems. The Green's function $G(\boldsymbol{r}, \boldsymbol{r'})$ gives the field at an observation point $\boldsymbol{r}$ from a source of unit strength concentrated at $\boldsymbol{r'}$ taking into account the boundary conditions for the given problem [59; 60]. Generally, depending on whether the field is a scalar (like electrostatic potential from a unit charge, or the gravitational potential from a unit mass) or a vector (like the electric field from a unit current source) the Green's function is a scalar or a dyad (tensor). Some of the Green's functions we frequently encounter are [59]:

1. For Poisson's equation $\boldsymbol{\nabla}^2 G(\boldsymbol{r} - \boldsymbol{r'}) = \delta(\boldsymbol{r} - \boldsymbol{r'})$ with free-space boundary condition:

$$G(\boldsymbol{r} - \boldsymbol{r'}) = \begin{cases} \dfrac{1}{2\pi} \ln[\boldsymbol{r} - \boldsymbol{r'}] & \text{for 2D space} \\ -\dfrac{1}{4\pi} \dfrac{1}{|\boldsymbol{r} - \boldsymbol{r'}|} & \text{for 3D space} \end{cases} \tag{2.38}$$

2. For Helmholtz's equation $\boldsymbol{\nabla}^2 G(\boldsymbol{r} - \boldsymbol{r'}) + k^2 G(\boldsymbol{r} - \boldsymbol{r'}) = \delta(\boldsymbol{r} - \boldsymbol{r'})$ with free-space boundary condition:

$$G(\boldsymbol{r} - \boldsymbol{r'}) = \begin{cases} -\dfrac{i}{4} h_0^{(1)}(k|\boldsymbol{r} - \boldsymbol{r'}|) & \text{for 2D space} \\ -\dfrac{e^{ik(\boldsymbol{r} - \boldsymbol{r'})}}{4\pi|\boldsymbol{r} - \boldsymbol{r'}|} & \text{for 3D space} \end{cases} \tag{2.39}$$

where $h_0^{(1)}$ denotes the zeroth order cylindrical Hankel function of the first kind.

2.4.1 Dyadic Green's functions

In this work, we will be mainly dealing with Green's functions in a dyadic form since we are trying to find the electromagnetic field in the presence of non-magnetic macroscopic dielectric materials. The electromagnetic fields are governed by the inhomogeneous vector Helmholtz equation, which can be obtained from the Maxwell's equations (see Sec. 2.1) and given by [61;

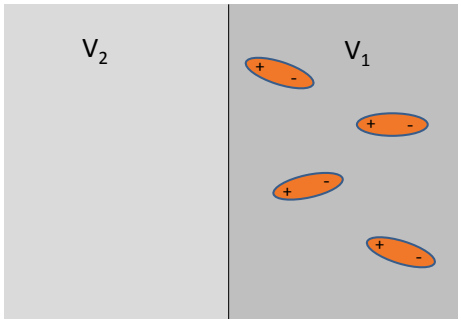

Figure 2.6: Interface between two planar bodies V_1 and V_2 with the fluctuating dipole sources being assumed to be confined in V_1

59]:

$$\boldsymbol{\nabla} \times \boldsymbol{\nabla} \times \boldsymbol{E}(\boldsymbol{r}, \omega) - \frac{\omega^2}{c^2} \varepsilon(\boldsymbol{r}, \omega) \boldsymbol{E}(\boldsymbol{r}, \omega) = i\mu_0 \omega \boldsymbol{J}(\boldsymbol{r}, \omega) \tag{2.40}$$

The solution of this equation in Green's function formalism can be written as:

$$\boldsymbol{E}(\boldsymbol{r}, \omega) = i\omega\mu_0 \int_V \overline{\overline{\boldsymbol{G}}}_e(\boldsymbol{r}, \boldsymbol{r'}, \omega) . \boldsymbol{J}(\boldsymbol{r'}, \omega)\, d^3 r' \tag{2.41}$$

where, $\overline{\overline{\boldsymbol{G}}}_e(\boldsymbol{r}, \boldsymbol{r'}, \omega)$ is the Dyadic Green's function (DGF) which will be in tensor form. The DGF satisfies the equation:

$$\boldsymbol{\nabla} \times \boldsymbol{\nabla} \times \overline{\overline{\boldsymbol{G}}}_e(\boldsymbol{r}, \boldsymbol{r'}\omega) - \frac{\omega^2}{c^2} \varepsilon(\boldsymbol{r}, \omega) \overline{\overline{\boldsymbol{G}}}_e(\boldsymbol{r}, \boldsymbol{r'}, \omega) = \delta(\boldsymbol{r} - \boldsymbol{r'}) \boldsymbol{I} \tag{2.42}$$

($\boldsymbol{I}$ is the unit dyad/tensor) along with the boundary conditions of the problem. This method was first used by Levine and Schwinger [62] in 1950 while analyzing electromagnetic wave diffraction effects.

For a bulk medium, where the medium is an infinitely extended homogeneous dielectric, the DGF is the solution of the equation:

$$\boldsymbol{\nabla} \times \boldsymbol{\nabla} \times \overline{\overline{\boldsymbol{G}}}_0(\boldsymbol{r}, \boldsymbol{r'}\omega) - \frac{\omega^2}{c^2} \varepsilon(\omega) \overline{\overline{\boldsymbol{G}}}_0(\boldsymbol{r}, \boldsymbol{r'}, \omega) = \delta(\boldsymbol{r} - \boldsymbol{r'}) \boldsymbol{I} \tag{2.43}$$

and should satisfy the Sommerfeld radiation condition at infinity [61; 59; 63]. The solution of this equation is given by [61; 59]:

$$\overline{\overline{\boldsymbol{G}}}_0(\boldsymbol{r}, \boldsymbol{r'}\omega) = -\left[\boldsymbol{I} + \frac{1}{k^2} \boldsymbol{\nabla}\boldsymbol{\nabla}\right] G(\boldsymbol{r}, \boldsymbol{r'}\omega) \tag{2.44}$$

where, $k^2 = \frac{\omega^2}{c^2}\varepsilon(\omega)$ and $G(\boldsymbol{r}, \boldsymbol{r'}\omega)$ is the solution of the scalar Helmholtz equation given in Eq. 2.39. So the DGF for the vector Helmholtz equation in bulk medium is given by:

$$\overline{\overline{\boldsymbol{G}}}_0(\boldsymbol{r}, \boldsymbol{r'}\omega) = \frac{1}{4\pi}\left[\boldsymbol{I} + \frac{1}{k^2}\boldsymbol{\nabla}\boldsymbol{\nabla}\right]\frac{e^{ik|\boldsymbol{r}-\boldsymbol{r'}|}}{|\boldsymbol{r}-\boldsymbol{r'}|} \tag{2.45}$$

In case of an interface (for simplicity consider a planar interface) like the one shown in Fig. 2.6, the effect of the interface is to impose additional boundary conditions on the electric field and hence on the DGF too. The effect of the interface can be considered by adding suitable solutions of the *homogeneous* Helmholtz equation to the bulk solution that we have already obtained. If we assume that the sources are only confined in V_1 ($\boldsymbol{r'} \in V_1$) as shown in Fig. 2.6 we have:

$$\overline{\overline{\boldsymbol{G}}}_e(\boldsymbol{r}, \boldsymbol{r'}, \omega) = \begin{cases} \overline{\overline{\boldsymbol{G}}}_0(\boldsymbol{r}, \boldsymbol{r'}, \omega) + \overline{\overline{\boldsymbol{G}}}_1(\boldsymbol{r}, \boldsymbol{r'}, \omega) & \text{for } \boldsymbol{r} \in V_1 \\ \overline{\overline{\boldsymbol{G}}}_1(\boldsymbol{r}, \boldsymbol{r'}, \omega) & \text{for } \boldsymbol{r} \in V_2 \end{cases} \tag{2.46}$$

where, $\overline{\overline{\boldsymbol{G}}}_1(\boldsymbol{r}, \boldsymbol{r'}, \omega)$ is the yet to be determined scattering DGF for the regions V_1 and V_2 (they are not the same for V_1 and V_2) which are the solutions to the equations:

$$\boldsymbol{\nabla} \times \boldsymbol{\nabla} \times \overline{\overline{\boldsymbol{G}}}_1(\boldsymbol{r}, \boldsymbol{r'}\omega) - \frac{\omega^2}{c^2}\varepsilon_j(\omega)\overline{\overline{\boldsymbol{G}}}_1(\boldsymbol{r}, \boldsymbol{r'}, \omega) = 0; \;\; j = 1, 2 \tag{2.47}$$

To find the scattered DGF, the bulk and the scattered DGF are expanded in fundamental modes of the vector Helmholtz equation, with the unknown coefficients of the expansion to be determined by applying appropriate boundary conditions to each mode. For planar surfaces, the DGF is expanded in vector planar waves, for spheres we adopt vector spherical waves. But the procedure is similar for both the cases. For more details refer to [64; 61; 65].

Similar to the way the electric field was defined in Eq. 2.41, we can define the magnetic field using:

$$\boldsymbol{H}(\boldsymbol{r}, \omega) = \int_V \overline{\overline{\boldsymbol{G}}}_h(\boldsymbol{r}, \boldsymbol{r'}, \omega).\boldsymbol{J}(\boldsymbol{r'}, \omega)\, d^3r' \tag{2.48}$$

where, $\overline{\overline{\boldsymbol{G}}}_e$ and $\overline{\overline{\boldsymbol{G}}}_h$ are related to each other by $\boldsymbol{\nabla} \times \overline{\overline{\boldsymbol{G}}}_e(\boldsymbol{r}, \boldsymbol{r'}\omega) = \overline{\overline{\boldsymbol{G}}}_h(\boldsymbol{r}, \boldsymbol{r'}\omega)$. Finding the net radiative transfer requires us to compute the Poynting vector given by: $\boldsymbol{S} = \boldsymbol{E} \times \boldsymbol{H}^*$,

where the '*' denotes complex conjugate. This requires us to find expressions of the type $\langle E_{i\omega} H^*_{j\omega} \rangle$ where the angled brackets denote ensemble average and i and j denote the three cartesian coordinates $i \neq j$. In terms of $\overline{\overline{\boldsymbol{G}}}_e$ and $\overline{\overline{\boldsymbol{G}}}_h$, this ensemble average can be written as:

$$\langle E_i(\boldsymbol{r_1}, \omega) H^*_j(\boldsymbol{r_1}, \omega) \rangle = i\omega\mu_0 \int_V d^3r \int_{V'} d^3r' G_{e_{il}}(\boldsymbol{r_1}, \boldsymbol{r}, \omega) G^*_{h_{jm}}(\boldsymbol{r_1}, \boldsymbol{r'}, \omega) \times \langle J_l(\boldsymbol{r}, \omega) J_m(\boldsymbol{r'}, \omega) \rangle \tag{2.49}$$

The topic of finding $\langle J_l(\boldsymbol{r}, \omega) J_m(\boldsymbol{r'}, \omega) \rangle$ is discussed in the next section.

2.5 Fluctuation dissipation theorem

The fluctuation-dissipation theorem (FDT) establishes for an arbitrary dissipative physical system the relationship between the spectral density of spontaneous equilibrium fluctuations and its dissipative properties. The development of FDT started with the investigation of the source for the 'noise' in electric circuits. The close relation between electric noise and thermal radiation lies in the fact that the radiation is composed of electromagnetic waves generated by thermal electric fluctuations in the body. For a long time a unified approach for such closely related physical phenomena was absent, possibly due to the fact that the frequency of electromagnetic oscillations in the above two phenomena was widely differently. Nyquist [66] first derived a formula, called Nyquist formula or the Nyquist theorem relating the spectral intensity of fluctuating electromotive force to the impedance of the electric circuit which was valid in the classical limit ($\hbar\omega \ll k_B T$). Further development of the theory of thermal fluctuations resulted in generalizations of this formula. In 1951, H.B. Callen and T.A. Welton [67] derived the FDT, which generalized Nyquist's formula to dissipative systems of arbitrary physical nature. In 1953, Rytov [68] developed a theory of thermal electromagnetic fields based on the FDT which was then subsequently used by Lifshitz [69] to develop his theory of van der Waals forces. According to this theory the fluctuating electromagnetic field is described as generated by random detached currents spread in the medium. To calculate the energy carried by this fluctuating field, the spatial correlation of

the spectral amplitudes of these random currents is needed. This is given by the FDT [67; 70; 71] as:

$$\langle J_l(\boldsymbol{r},\omega)J_m(\boldsymbol{r'},\omega)\rangle = \frac{2\varepsilon_o\,\varepsilon''(\omega)\,\omega\,\Theta(\omega,T)}{\pi}\delta_{lm}\delta(\boldsymbol{r}-\boldsymbol{r'}) \tag{2.50}$$

where $\varepsilon''(\omega)$ is the imaginary part of the dielectric function of the source, and $\Theta(\omega,T)$ is given by $\hbar\omega/[exp(\hbar\omega/k_BT)-1]$. Thus the spectral density of electromagnetic source fluctuations is directly associated with a macroscopic property of the system [in this case $\varepsilon''(\omega)$]. The δ_{lm} factor ensures that there is no coupling between the fluctuations in the orthogonal directions. The presence of $\delta(\boldsymbol{r}-\boldsymbol{r'})$ implies that the currents at any two positions $\boldsymbol{r}$ and $\boldsymbol{r'}$ in the material are taken to be uncorrelated. This assumption is valid only when the length scales involved in the problem is much greater than the mean-free path of the electrons in metals or atomic spacing in dielectrics [68]. In this work we shall assume the validity of Eq. 2.50.

2.6 Near-field radiative heat transfer between two planar bodies

Since the proximity approximation makes use of the near-field radiative heat transfer coefficient from two parallel flat surfaces to approximate the conductance between curved bodies, it is necessary to give a brief explanation about the computation of the radiative heat flux between two flat surfaces. The development of the theory of computing near-field radiative transfer between planar surfaces is similar to the development of that between two spherical bodies except that we use vector spherical waves in the latter case as opposed to vector planar waves in the former case for the modal expansion of the dyadic Green's functions.

The magnitude of heat transfer by radiative transfer is determined by calculating the Poynting vector at the desired location [44]. The ensemble average Poynting vector $\langle\boldsymbol{S}\rangle$ at any position $\boldsymbol{r}$ is given by:

$$\langle\boldsymbol{S}(\boldsymbol{r},\omega)\rangle = \int_0^\infty \mathrm{Re}\langle\boldsymbol{E}(\boldsymbol{r},\omega)\times\boldsymbol{H}^*(\boldsymbol{r},\omega)\rangle\,d\omega \tag{2.51}$$

The cross product of two vector quantities $\boldsymbol{A}$ and $\boldsymbol{B}$ in Einstein notation is given by:

$$(\boldsymbol{A}\times\boldsymbol{B})_i = e_{ijk}A_jB_k$$

where e_{ijk} is the Levi-Civita symbol, and i,j,k refer to the three Cartesian components. Hence the Poynting vector can be written as:

$$\langle S_i(\boldsymbol{r},\omega)\rangle = e_{ijk}\langle E_j(\boldsymbol{r},\omega)H_k^*(\boldsymbol{r},\omega)\rangle \tag{2.52}$$

The electric field and magnetic field can be expressed in terms of the electric DGF $\overline{\overline{\boldsymbol{G}}}_e$ (which needs to be found) as given in Eq. 2.41 and Eq. 2.48. By using the tensor notation we can write:

$$E_j(\boldsymbol{r},\omega) = i\omega\mu_0 \int G_{jp}^e(\boldsymbol{r},\boldsymbol{r'},\omega)J_p(\boldsymbol{r'},\omega)\,dr' \tag{2.53}$$

$$H_k^*(\boldsymbol{r},\omega) = \int G_{kl}^{h*}(\boldsymbol{r},\boldsymbol{r''},\omega)J_l(\boldsymbol{r''},\omega)\,dr'' \tag{2.54}$$

Thus from Eq. 2.52, Eq. 2.53 and Eq. 2.54 we can write:

$$S_i(\boldsymbol{r},\omega) = e_{ijk}i\omega\mu_0 \iint G_{jp}^e(\boldsymbol{r},\boldsymbol{r'},\omega)G_{kl}^{h*}(\boldsymbol{r},\boldsymbol{r''},\omega)\langle J_p(\boldsymbol{r'},\omega)J_l(\boldsymbol{r''},\omega)\rangle\,dr'\,dr'' \tag{2.55}$$

Substituting for $\langle J_p(\boldsymbol{r'},\omega)J_l(\boldsymbol{r''},\omega)\rangle$ from the fluctuation-dissipation theorem given in Eq. 2.50 we have:

$$S_i(\boldsymbol{r},\omega) = e_{ijk}\frac{2i\omega^2}{\pi}\mu_0\varepsilon_0\varepsilon''(\omega)\Theta(\omega,T) \iint G_{jp}^e(\boldsymbol{r},\boldsymbol{r'},\omega)G_{kp}^{h*}(\boldsymbol{r},\boldsymbol{r''},\omega)\delta(\mathbf{r''}-\boldsymbol{r'})\,dr'\,dr'' \tag{2.56}$$

$$\Leftrightarrow S_i(\boldsymbol{r},\omega) = e_{ijk}\frac{2i\omega^2}{\pi}\mu_0\varepsilon_0\varepsilon''(\omega)\Theta(\omega,T) \int G_{jp}^e(\boldsymbol{r},\boldsymbol{r'},\omega)G_{kp}^{h*}(\boldsymbol{r},\boldsymbol{r'},\omega)\,dr' \tag{2.57}$$

Since we need the heat transfer in the z-direction, we get:

$$S_z(\boldsymbol{r},\omega) = \frac{2i\omega^2}{\pi}\mu_0\varepsilon_0\varepsilon''(\omega)\Theta(\omega,T) \int \left[G_{xp}^e(\boldsymbol{r},\boldsymbol{r'},\omega)G_{yp}^{h*}(\boldsymbol{r},\boldsymbol{r'},\omega) - G_{yp}^e(\boldsymbol{r},\boldsymbol{r'},\omega)G_{xp}^{h*}(\boldsymbol{r},\boldsymbol{r'},\omega)\right]\,dr' \tag{2.58}$$

$$\Leftrightarrow S_z(\boldsymbol{r},\omega) = \frac{2i\omega^2}{\pi}\mu_0\varepsilon_0\varepsilon''(\omega)\Theta(\omega,T) \int \left[\overline{\overline{\boldsymbol{G}}}_e(\boldsymbol{r},\boldsymbol{r'},\omega).\overline{\overline{\boldsymbol{G}}}_T^{h*}(\boldsymbol{r},\boldsymbol{r'},\omega)\right]_{xy-yx} dr' \tag{2.59}$$

where,the subscript T denotes transpose of the dyad.

In order to find $\overline{\overline{\boldsymbol{G}}}_e(\boldsymbol{r},\boldsymbol{r'},\omega)$ and $\overline{\overline{\boldsymbol{G}}}_h^*(\boldsymbol{r},\boldsymbol{r'},\omega)$ we use the orthonormal triad $\hat{\boldsymbol{e}}$, $\hat{\boldsymbol{h}}$, $\hat{\boldsymbol{k}}$ defined by the relations:

$$\hat{\boldsymbol{e}} = \frac{\boldsymbol{k}\times\boldsymbol{z}}{|\boldsymbol{k}\times\boldsymbol{z}|} \tag{2.60}$$

$$\hat{\boldsymbol{h}} = \frac{\hat{\boldsymbol{e}}\times\boldsymbol{k}}{|\boldsymbol{k}|} \tag{2.61}$$

$$\hat{\boldsymbol{k}} = \frac{\boldsymbol{k}}{|\boldsymbol{k}|} \tag{2.62}$$

In the orthonormal basis $(\hat{\boldsymbol{e}},\hat{\boldsymbol{h}},\hat{\boldsymbol{k}})$, the expression for $\overline{\overline{\boldsymbol{G}}}_e(\boldsymbol{r},\boldsymbol{r'})$ which relates the source in medium 1 to the field in medium 3 as shown in Fig. 2.8 is given by [71; 72]:

$$\overline{\overline{\boldsymbol{G}}}_e(\boldsymbol{r},\boldsymbol{r'}) = \frac{i}{8\pi^2}\iint dk_x dk_y \frac{1}{k_{1z}}\Big(\left[A_3 e^{i\boldsymbol{k}_3\cdot\boldsymbol{r}}\hat{\boldsymbol{e}}(k_{3z})\right]\hat{\boldsymbol{e}}(k_{1z})e^{-i\boldsymbol{k}_1\cdot\boldsymbol{r'}} \\ \left[C_3 e^{i\boldsymbol{k}_3\cdot\boldsymbol{r}}\hat{\boldsymbol{h}}(k_{3z})\right]\hat{\boldsymbol{h}}(k_{1z})e^{-i\boldsymbol{k}_1\cdot\boldsymbol{r'}}\Big) \tag{2.63}$$

with $\boldsymbol{k}_3 = k_x\hat{\boldsymbol{x}} + k_y\hat{\boldsymbol{y}} + k_{3z}\hat{\boldsymbol{z}}$ and $\boldsymbol{k}_1 = k_x\hat{\boldsymbol{x}} + k_y\hat{\boldsymbol{y}} + k_{1z}\hat{\boldsymbol{z}}$

This can be viewed as an up-going vector planar TE wave $e^{-i\boldsymbol{k}_1\cdot\boldsymbol{r'}}\hat{\boldsymbol{e}}(k_{1z})$ in the source layer (medium 1) giving rise to a transmitted wave $A_3 e^{i\boldsymbol{k}_3\cdot\boldsymbol{r}}\hat{\boldsymbol{e}}(k_{3z})$ in medium 3. Similarly a vector planar TM wave $\hat{\boldsymbol{h}}(k_{1z})e^{-i\boldsymbol{k}_1\cdot\boldsymbol{r'}}$ gives rise to a transmitted wave $C_3 e^{i\boldsymbol{k}_3\cdot\boldsymbol{r}}\hat{\boldsymbol{h}}(k_{3z})$ in medium 3. The coefficients A_3 and C_3 is found out by applying the boundary conditions at the interfaces using the steps described in the next paragraph.

Consider first an interface between two infinite media located at position z_1 as shown in Fig. 2.7. A planar wave of unit amplitude in medium 1 $e^{+ik_{1z}z}$ impinging on the interface gives rise to a reflected wave $B_1 e^{-ik_{1z}z}$ in medium 1 as well as a transmitted wave $A_2 e^{+ik_{2z}z}$ in medium 2. Here k_{1z} and k_{2z} denote the component of wavevector in the z-direction in the first medium and second medium respectively. The coefficients B_1 and A_2 can be found by employing boundary conditions (continuity of electric and magnetic fields) at the interface. For TE waves (assuming nonmagnetic media with $\mu_l = 1$), the boundary conditions at the

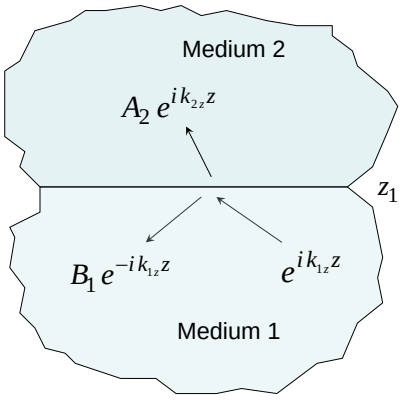

Figure 2.7: Reflection and transmission at an interface between two infinite media

interface located at z_1 give two linear equations in B_1 and A_2 [61; 64]:

$$e^{+ik_{1z}z_1} + B_1 e^{-ik_{1z}z_1} = A_2 e^{ik_{2z}z_1} \tag{2.64}$$

$$k_{1z}(e^{+ik_{1z}z_1} - B_1 e^{-ik_{1z}z_1}) = k_{2z}(A_2 e^{ik_{2z}z_1}) \tag{2.65}$$

For TM waves the corresponding boundary conditions are:

$$\frac{k_{1z}}{\frac{\omega}{c}\sqrt{\varepsilon_1}}(e^{+ik_{1z}z_1} - D_1 e^{-ik_{1z}z_1}) = \frac{k_{2z}}{\frac{\omega}{c}\sqrt{\varepsilon_2}}(C_2 e^{ik_{2z}z_1}) \tag{2.66}$$

$$\frac{\omega}{c}\sqrt{\varepsilon_1}(e^{+ik_{1z}z_1} + D_1 e^{-ik_{1z}z_1}) = \frac{\omega}{c}\sqrt{\varepsilon_2}(C_2 e^{ik_{2z}z_1}) \tag{2.67}$$

where C_2 and D_1 are the transmission and reflection coefficients analogous to A_2 and B_1. Solving Eqs. 2.64 and 2.65 for B_1 we get:

$$B_1 = e^{2ik_{1z}z_1}\frac{k_{1z} - k_{2z}}{k_{1z} + k_{2z}}, \tag{2.68}$$

which can be written in the form $B_1 = e^{2ik_{1z}z_1}R_{12}$ where R_{12} denotes the Fresnel reflection coefficient for a wave traveling from medium 1 to medium 2 and is given by (for TE waves):

$$R_{12}^{TE} = \frac{k_{1z} - k_{2z}}{k_{1z} + k_{2z}}, \tag{2.69}$$

For TM waves the Fresnel reflection coefficient is given by:

$$R_{12}^{TM} = \frac{k_{1z}/\varepsilon_1 - k_{2z}/\varepsilon_2}{k_{1z}/\varepsilon_1 + k_{2z}/\varepsilon_2} \tag{2.70}$$

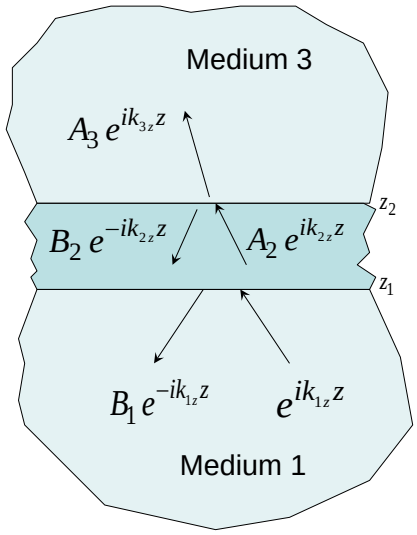

Figure 2.8: Reflection and transmission from a film embedded between two half spaces

The relation between B_1 and R_{12} is got from:

$$R_{12}^{TE} e^{+ik_{1z}z_1} = B_1 e^{-ik_{1z}z_1} \tag{2.71}$$

In the presence of an additional interface at z_2 as shown in Fig. 2.8 the expression for B_1 will change. Applying boundary conditions similar to Eqs. 2.64 and 2.65 to the interfaces at z_1 and z_2 and solving for B_1 we get

$$B_1 = e^{2ik_{1z}z_1} \frac{R_{12} + R_{23} e^{2ik_{2z}(z_2 - z_1)}}{1 + R_{12} R_{23} e^{2ik_{2z}(z_2 - z_1)}}, \tag{2.72}$$

where R_{12} and R_{23} are the Fresnel reflection coefficients at the interfaces z_1 and z_2 defined appropriately as shown in Eq. 2.69 and Eq. 2.70. Depending on whether the analysis is being performed for TE or TM waves, the corresponding form of the Fresnel reflection coefficients have to be used.

Equation 2.67 can be written in the form $B_1 = e^{2ik_{1z}z_1} \tilde{R}_{12}$ where $\tilde{R}_{12}$ denotes the altered reflection coefficient for the interface at z_1 in the presence of an additional interface at z_2 and is given by:

$$\tilde{R}_{12} = \frac{R_{12} + R_{23} e^{2ik_{2z}(z_2 - z_1)}}{1 + R_{12} R_{23} e^{2ik_{2z}(z_2 - z_1)}}, \tag{2.73}$$

Here, the reflection coefficient for the interface at z_1, $\tilde{R}_{12}$, has been written in terms of the reflection coefficient of the interface above it, R_{23}. While only two interfaces needs to be considered for finding the radiative heat transfer between two planar surfaces, this method can be generalized to the case when you have several successive layers. For such a case we can find a generalized reflection coefficient $\tilde{R}_{n,n+1}$ in terms of the reflection coefficient at the $(n+1)^{th}$ interface, $\tilde{R}_{n+1,n+2}$ as:

$$\tilde{R}_{n,n+1} = \frac{R_{n,n+1} + \tilde{R}_{n+1,n+2} e^{2ik_{(n+1)z}(z_{n+1}-z_n)}}{1 + R_{n,n+1}\tilde{R}_{n+1,n+2} e^{2ik_{(n+1)z}(z_{n+1}-z_n)}}, \tag{2.74}$$

This enables us to set up a recursive scheme to find the reflection coefficients in all the layers whereby the reflection coefficient in the top most interface is given by the Fresnel coefficient and for each of the successive layers, the reflection coefficient is computed in terms of the reflection coefficient of the interface immediately above it by employing the form shown in Eq. 2.74. Knowing the reflection coefficients at an interface, the boundary condition equation at the interface (Eq. 2.64 or 2.65) can be used to find the corresponding transmission coefficient.

By solving the boundary conditions we arrive at the transmission coefficients A_3 (for TE waves) and C_3 (for TM waves) and thus the electric DGF from Eq. 2.63. The magnetic DGF $\overline{\overline{\boldsymbol{G}}}_h$ is obtained from $\nabla \times \overline{\overline{\boldsymbol{G}}}_e = \overline{\overline{\boldsymbol{G}}}_h$ and using these in Eq. 2.59 we get the net heat transfer per unit area from surface 1 to surface 2 across the vacuum film. The radiative heat transfer coefficient h between two silica planar surfaces has been plotted in Fig. 2.9. A slope of -2 in the log-log plot indicate a $1/d^2$ behavior in the near-field region. To understand why we see a $1/d^2$ at small gaps, consider the expression for the net radiative heat transfer between two planar surfaces via *evanescent waves*. This is given by [44]:

$$q^{evan} = \frac{1}{\pi^2}\int_0^\infty d\omega \left[\Theta(\omega, T_1) - \Theta(\omega, T_2)\right] \int_0^\infty k_\rho \frac{\mathrm{Im}(r_{01}^p)\mathrm{Im}(r_{02}^p)e^{-2k_\rho d}}{|1 - r_{01}^p\, r_{02}^p e^{-2k_\rho d}|^2}\, dk_\rho \tag{2.75}$$

where, $\Theta(\omega, T_1)$ is the mean energy of the Planck's oscillator at temperature T_1, k_ρ is the in-plane component of the wave vector, r_{01}^p and r_{02}^p are the Fresnel reflection coefficients (for TM waves) for the two surfaces respectively (with vacuum as interface) which are independent of k_ρ in the limit $k_\rho \gg \omega/c$ (true for evanescent waves), d is the separation distance and k_ρ

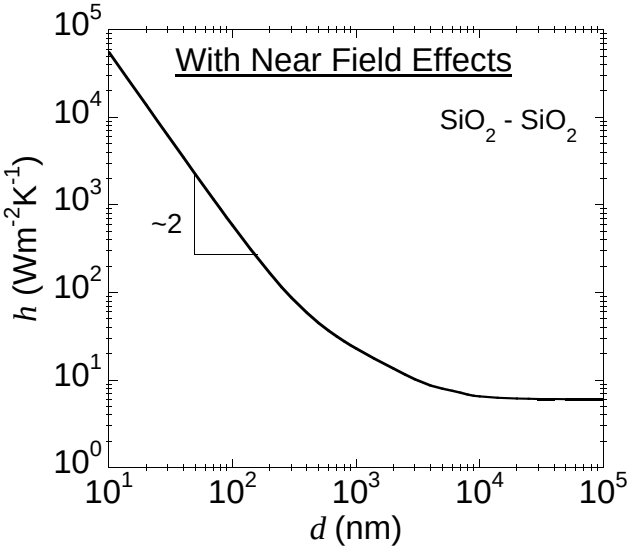

Figure 2.9: Plot of radiative heat transfer coefficient h as a function of gap in nm for two planar surfaces made of silica

is the in-plane wave propagation constant. To facilitate integration taking $k_\rho d = \beta$ where β is an integration parameter, Eq. 2.75 can be simplified to:

$$q^{evan} = \frac{1}{\pi^2}\int_0^\infty d\omega\,[\Theta(\omega,T_1)-\Theta(\omega,T_2)]\frac{1}{d^2}\int_0^\infty d\beta\,\beta\frac{\mathrm{Im}(r_{01}^p)\mathrm{Im}(r_{02}^p)e^{-2\beta}}{|1-r_{01}^p\,r_{02}^p e^{-2\beta}|^2} \tag{2.76}$$

$$\Leftrightarrow q^{evan} = \frac{1}{d^2}\int_0^\infty d\omega\,[\Theta(\omega,T_1)-\Theta(\omega,T_2)]K \tag{2.77}$$

where,

$$K = \frac{1}{\pi^2}\int_0^\infty \beta\frac{\mathrm{Im}(r_{01}^p)\mathrm{Im}(r_{02}^p)e^{-2\beta}}{|1-r_{01}^p\,r_{02}^p e^{-2\beta}|^2}\,d\beta \tag{2.78}$$

Eq. 2.77 shows that for small gaps, when the contribution from evanescent waves is dominant, the radiative heat transfer varies as $1/d^2$.

Part II

Near-field radiative transfer between spherical bodies

Chapter 3

Theoretical formulation for computing radiative transfer between spherical objects

3.1 Introduction

In this chapter the semi-analytical method that has been developed by Narayanaswamy and Chen [36] to arrive at an expression for the the near-field radiative heat flux between two spheres maintained at temperatures T_A and T_B has been outlined briefly and some of the steps for arriving at the analytical expressions listed in Ref. [36] have been shown explicitly. The theoretical procedure is similar to that between planar bodies which has been outlined in Chapter 2.

3.2 Discussion

The configuration of the two spheres between which radiative transfer is to be calculated is shown in Fig. 3.1. Radiative heat transfer between the spheres is calculated using Rytov's theory of fluctuational electrodynamics [2]. The Fourier component of the fluctuating electric field $\boldsymbol{E}(\boldsymbol{r}_a, \omega)$ and magnetic field $\boldsymbol{H}(\boldsymbol{r}_a, \omega)$ at any point $\boldsymbol{r}_a$ are given by Eq. 2.41 and Eq.

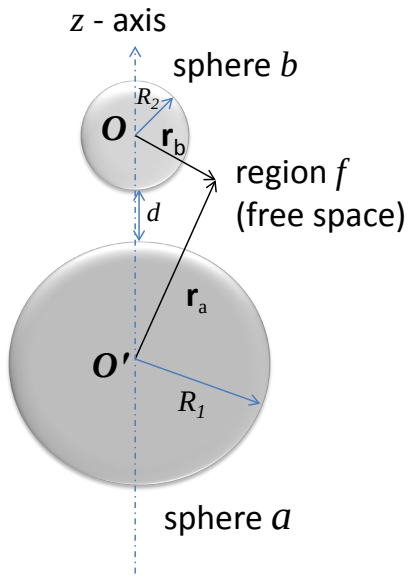

Figure 3.1: Configuration of two spheres whose centers are translated along z-axis

2.48 (repeated here for completeness of discussion). They are given by:

$$\boldsymbol{E}(\boldsymbol{r}_a,\omega) = i\omega\mu_o \int_V d^3 r_{a'}\, \overline{\overline{\boldsymbol{G}}}_e(\boldsymbol{r}_a,\boldsymbol{r}'_a,\omega)\cdot\boldsymbol{J}(\boldsymbol{r}'_a,\omega), \qquad \text{(2.41 revisited)}$$

$$\boldsymbol{H}(\boldsymbol{r}_a,\omega) = \int_V d^3 r_{a'}\overline{\overline{\boldsymbol{G}}}_h(\boldsymbol{r}_a,\boldsymbol{r}'_a,\omega)\cdot\boldsymbol{J}(\boldsymbol{r}'_a,\omega), \qquad \text{(2.48 revisited)}$$

where $\overline{\overline{\boldsymbol{G}}}_e(\boldsymbol{r}_a,\boldsymbol{r}'_a,\omega)$ and $\overline{\overline{\boldsymbol{G}}}_h(\boldsymbol{r}_a,\boldsymbol{r}'_a,\omega)$ are the dyadic Green's functions (DGF) for the electric and magnetic fields due to a point source at $\boldsymbol{r}'_a$ and are related by $\overline{\overline{\boldsymbol{G}}}_h(\boldsymbol{r}_a,\boldsymbol{r}'_a,\omega) = \boldsymbol{\nabla}\times\overline{\overline{\boldsymbol{G}}}_e(\boldsymbol{r}_a,\boldsymbol{r}'_a,\omega)$, $\boldsymbol{J}(\boldsymbol{r}'_a,\omega)$ is the Fourier component of the current density due to thermal fluctuations, and μ_o is the permeability of vacuum. The integration is performed over the entire volume V containing the source.

Finding the DGF is a non-trivial task. In order to employ Eq. 2.41 and 2.48 to find the electric and magnetic fields in the scattered region, the DGF must necessarily satisfy the boundary conditions on the surface of the two spheres. The boundary conditions are:

1. Tangential part of the electric DGF has to continuous i.e.

$$\hat{\boldsymbol{n}}\times\overline{\overline{\boldsymbol{G}}}_e(\boldsymbol{r}_1,\boldsymbol{r}') = \hat{\boldsymbol{n}}\times\overline{\overline{\boldsymbol{G}}}_e(\boldsymbol{r}_2,\boldsymbol{r}') \qquad (3.1)$$

2. Tangential part of the magnetic DGF has to be continuous i.e.

$$\hat{\boldsymbol{n}} \times \overline{\overline{\boldsymbol{G}}}_h(\boldsymbol{r}_1, \boldsymbol{r'}) = \hat{\boldsymbol{n}} \times \overline{\overline{\boldsymbol{G}}}_h(\boldsymbol{r}_2, \boldsymbol{r'}) \tag{3.2}$$

where, $\hat{\boldsymbol{n}}$ is a unit normal to the boundary surface at $\boldsymbol{r_1}$ or $\boldsymbol{r_2}$. The development of $\overline{\overline{\boldsymbol{G}}}_e$ and $\overline{\overline{\boldsymbol{G}}}_h$ parallels that of the layered media case explained in Chapter 2 except that one has to employ vector spherical waves $\boldsymbol{M}$ and $\boldsymbol{N}$ waves in place of the vector planar waves. A brief outline of this is given in the ensuing paragraphs.

Consider first the case when there are no boundaries (i.e homogenous medium). The electric DGF for the field at any observation point $\boldsymbol{r}_a$ due to a source at $\boldsymbol{r'_a}$ is given by the solution of the in-homogenous vector Helmholtz equation given in Eq. 2.42, along with the Sommerfeld radiation boundary condition mentioned in Chapter 2. The electric DGF is given by [65; 64; 59]:

$$\begin{aligned}\overline{\overline{\boldsymbol{G}}}_e(\boldsymbol{r}_a, \boldsymbol{r'_a}) =& \frac{\hat{\boldsymbol{r}}\hat{\boldsymbol{r}}}{k_a^2}\delta(\boldsymbol{r}_a - \boldsymbol{r'_a}) \\ &+ ik_a \sum_{\substack{m=-l \\ l=1}}^{\substack{l=\infty \\ m=l}} \begin{cases} \boldsymbol{M}^{(1)}_{lm}(k_a\boldsymbol{r}_a)\boldsymbol{M}^{(3)}_{l,-m}(k_a\boldsymbol{r'_a}) + \boldsymbol{N}^{(1)}_{lm}(k_a\boldsymbol{r}_a)\boldsymbol{N}^{(3)}_{l,-m}(k_a\boldsymbol{r'_a}) & \text{if } r_a < r'_a \\ \boldsymbol{M}^{(3)}_{lm}(k_a\boldsymbol{r}_a)\boldsymbol{M}^{(1)}_{l,-m}(k_a\boldsymbol{r'_a}) + \boldsymbol{N}^{(3)}_{lm}(k_a\boldsymbol{r}_a)\boldsymbol{N}^{(1)}_{l,-m}(k_a\boldsymbol{r'_a}) & \text{if } r_a > r'_a \end{cases}\end{aligned} \tag{3.3}$$

where $\boldsymbol{r'_a}$ is the source point and $\boldsymbol{r_a}$ is the observation point. In particular, we will be interested in the case where $r_a > r'_a$ (since we later take the source to be inside sphere A whereas the boundary of interest will be the surface of the sphere). In this case the DGF takes the form:

$$\overline{\overline{\boldsymbol{G}}}_e(\boldsymbol{r}_a, \boldsymbol{r'_a}) = ik_a \sum_{\substack{m=-l \\ l=1}}^{\substack{l=\infty \\ m=l}} \left[\boldsymbol{M}^{(3)}_{lm}(k_a\boldsymbol{r}_a)\boldsymbol{M}^{(1)}_{l,-m}(k_a\boldsymbol{r'_a}) + \boldsymbol{N}^{(3)}_{lm}(k_a\boldsymbol{r}_a)\boldsymbol{N}^{(1)}_{l,-m}(k_a\boldsymbol{r'_a})\right] \tag{3.4}$$

This equation can be viewed as $\boldsymbol{M}^{(3)}_{lm}(k_a\boldsymbol{r}_a)$ waves being generated at the observation point $\boldsymbol{r}_a$ by $\boldsymbol{M}^{(1)}_{l,-m}(k_a\boldsymbol{r'_a})$ waves at the source point $\boldsymbol{r'_a}$ (and similarly for $\boldsymbol{N}^{(3)}_{lm}(k_a\boldsymbol{r}_a)$ waves). However, in the presence of a boundary/interface, due to reflection of waves from the interface, there

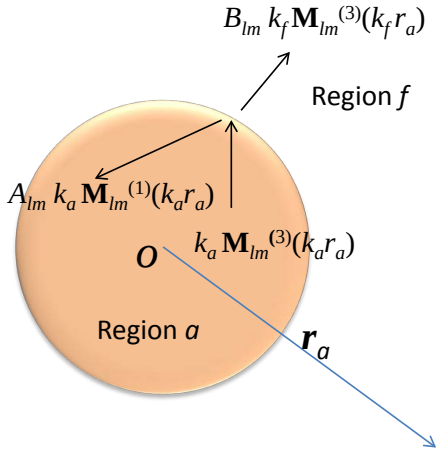

Figure 3.2: Configuration showing reflection and transmission of a $\boldsymbol{M}$ vector spherical wave inside a sphere of radius R_1. The origin of the coordinate system is located at the center of the sphere marked as O and the blue line denotes the position vector $\boldsymbol{r}_a$ with respect to this coordinate system

will be additional fields generated. For demonstrative purposes a simple boundary case (a single sphere surrounded by free space) has been analyzed below.

3.2.1 Analysis for a single sphere

Consider the case of an outgoing $\boldsymbol{M}_{lm}^{(3)}(k_a \boldsymbol{r}_a)$ wave inside a single sphere (region a) of radius R_1 as shown in Fig. 3.2. This will give rise to a reflected wave in region a as well as a transmitted wave in region f, which can be represented by $A_{lm}\boldsymbol{M}_{lm}^{(1)}(k_a \boldsymbol{r}_a)$ and $B_{lm}\boldsymbol{M}_{lm}^{(3)}(k_f \boldsymbol{r}_a)$ respectively, where k_a and k_f are the frequency dependent wave propagation constants in the two regions a and f respectively as shown in Fig. 3.2. A_{lm} and B_{lm} are unknown coefficients which are to be determined. Depending on the region in question we can use only $\boldsymbol{M}^{(1)}(k_a \boldsymbol{r}_a)$ ($\boldsymbol{M}^{(3)}(k_f \boldsymbol{r}_a)$) to avoid encountering singularity as $k_a \boldsymbol{r}_a \to 0$ ($k_f \boldsymbol{r}_a \to \infty$).

For this simple case, the DGF for an observation point in region a is given by:

$$\overline{\overline{\boldsymbol{G}}}_e(\boldsymbol{r}_a, \boldsymbol{r}'_a) = ik_a \sum_{\substack{m=-l \\ l=1}}^{\substack{l=\infty \\ m=l}} \begin{bmatrix} \left[\boldsymbol{M}^{(3)}_{lm}(k_a\boldsymbol{r}_a) + A_{lm}\boldsymbol{M}^{(1)}_{lm}(k_a\boldsymbol{r}_a)\right]\boldsymbol{M}^{(1)}_{l,-m}(k_a\boldsymbol{r}'_a) \\ +\left[\boldsymbol{N}^{(3)}_{lm}(k_a\boldsymbol{r}_a) + A'_{lm}\boldsymbol{N}^{(1)}_{lm}(k_a\boldsymbol{r}_a)\right]\boldsymbol{N}^{(1)}_{l,-m}(k_a\boldsymbol{r}'_a) \end{bmatrix} \tag{3.5}$$

and for an observation point in region f the DGF is given by:

$$\overline{\overline{\boldsymbol{G}}}_e(\boldsymbol{r}_a, \boldsymbol{r}'_a) = ik_f \sum_{\substack{m=-l \\ l=1}}^{\substack{l=\infty \\ m=l}} \begin{bmatrix} \left[B_{lm}\boldsymbol{M}^{(3)}_{lm}(k_f\boldsymbol{r}_a)\right]\boldsymbol{M}^{(1)}_{l,-m}(k_a\boldsymbol{r}'_a) \\ +\left[B'_{lm}\boldsymbol{N}^{(3)}_{lm}(k_f\boldsymbol{r}_a)\right]\boldsymbol{N}^{(1)}_{l,-m}(k_a\boldsymbol{r}'_a) \end{bmatrix} \tag{3.6}$$

where, A'_{lm} and B'_{lm} are analogous to A_{lm} and B_{lm} but for a $\boldsymbol{N}$ wave. The coefficients A_{lm}, B_{lm}, A'_{lm} and B'_{lm} are determined by applying the boundary conditions (Eq. 3.1 and 3.2) on the surface of the sphere. This has been shown below:

First, we note from referring to the expression for DGF in Eq. 3.4 that what we have to analyze is not just propagation of $\boldsymbol{M}^{(3)}_{lm}(k_p r_a)$ wave function but the function $k_p\,\boldsymbol{M}^{(3)}_{lm}(k_p r_a)$ where k_p is the propagation constant in the medium where the $\boldsymbol{M}$ wave is propagating. The tangential component of the $\boldsymbol{M}^{(3)}_{lm}(k_p r_a)$ $\left[\boldsymbol{N}^{(3)}_{lm}(k_p r_a)\right]$ wave is $z^{(3)}_l(k_p r_a)$ $\left[\zeta^{(3)}_l(k_p r_a)\ \right]$ where $\zeta^{(3)}_l(x) = \frac{1}{x}\frac{d}{dx}\left(xz^{(3)}_l(x)\right)$. Using $\nabla \times \boldsymbol{M} = k\boldsymbol{N}$ we get the boundary condition equations to be (noting that at the interface the magnitude of position vector $\boldsymbol{r}_a$ is R_1):

$$k_a z^{(3)}_l(k_a R_1) + B_{lm} k_a z^{(1)}_l(k_a R_1) = A_{lm} k_f z^{(3)}_l(k_f R_1) \tag{3.7}$$

$$k_a^2 \zeta^{(3)}_l(k_a R_1) + B_{lm} k_a^2 \zeta^{(1)}_l(k_a R_1) = A_{lm} k_f^2 \zeta^{(3)}_l(k_f R_1) \tag{3.8}$$

Solving this gives us:

$$B_{lm} = \frac{k_f z^{(3)}_l(k_a R_1)\zeta^{(3)}_l(k_f R_1) - k_a z^{(3)}_l(k_f R_1)\zeta^{(3)}_l(k_a R_1)}{k_a z^{(3)}_l(k_f R_1)\zeta^{(1)}_l(k_a R_1) - k_f z^{(1)}_l(k_a R_1)\zeta^{(3)}_l(k_f R_1)} \tag{3.9}$$

In such problems it also useful to find an expression for the reflection coefficient at the interface of region a and region f, $\tilde{R}_{af}$, given by:

$$\tilde{R}_{af}\, k_a z^{(3)}_l(k_a R_1) = B_{lm}\, k_a z^{(1)}_l(k_a R_1) \tag{3.10}$$

This gives us:

$$\tilde{R}^{(M)}_{af} = \left(\frac{k_f z^{(3)}_l(k_a R_1)\zeta^{(3)}_l(k_f R_1) - k_a z^{(3)}_l(k_f R_1)\zeta^{(3)}_l(k_a R_1)}{k_a z^{(3)}_l(k_f R_1)\zeta^{(1)}_l(k_a R_1) - k_f z^{(1)}_l(k_a R_1)\zeta^{(3)}_l(k_f R_1)}\right)\left(\frac{z^{(1)}_l(k_a R_1)}{z^{(3)}_l(k_a R_1)}\right) \tag{3.11}$$

The superscript (M) denotes that the analysis is for the propagation of $\boldsymbol{M}$ wave. Substituting $\zeta(k_f R_1) = \dfrac{z(k_f R_1) + (k_f\, R_1)\, \frac{\partial z(x)}{\partial x}|_{k_f R_1}}{k_f\, R_1}$ and using

$$\frac{\partial f_n}{\partial x} = \frac{n}{x} f_n - f_{n+1} \tag{3.12}$$

with f denoting the Bessel function we can show that this is equivalent to:

$$\tilde{R}_{af}^{(M)} = \left(\frac{k_a \, \frac{z_{n+1}^{(3)}(k_a R_1)}{z_n^{(3)}(k_a R_1)} - k_f \, \frac{z_{n+1}^{(3)}(k_f R_1)}{z_n^{(3)}(k_f R_1)}}{k_f \, \frac{z_{n+1}^{(3)}(k_f R_1)}{z_n^{(3)}(k_f R_1)} - k_a \, \frac{z_{n+1}^{(1)}(k_a R_1)}{z_n^{(1)}(k_a R_1)}} \right) \tag{3.13}$$

Similarly, solving for A_{lm} in Eq. 3.7 and 3.8 we get,

$$A_{lm} = \frac{k_a}{k_f} \left(\frac{k_a z_l^{(3)}(k_a R_1) \zeta_l^{(1)}(k_a R_1) - k_a z_l^{(1)}(k_a R_1) \zeta_l^{(3)}(k_a R_1)}{k_a z_l^{(3)}(k_f R_1) \zeta_l^{(1)}(k_a R_1) - k_f z_l^{(1)}(k_a R_1) \zeta_l^{(3)}(k_f R_1)} \right) \tag{3.14}$$

The expression for the transmission coefficient at the interface of region a and region f, $\tilde{T}_{af}^{(M)}$, is got from the equation:

$$\tilde{T}_{af}^{(M)}\, k_a z_l^{(3)}(k_a R_1) = A_{lm}\, k_f z_l^{(3)}(k_f R_1) \tag{3.15}$$

For an outgoing $\boldsymbol{N}_{lm}^{(3)}(k_a \boldsymbol{r}_a)$ wave in Fig. 3.2 the coefficients A'_{lm} and B'_{lm} can be similarly solved to give:

$$A'_{lm} = \frac{k_a z_l^{(3)}(k_a R_1) \zeta_l^{(3)}(k_f R_1) - k_f z_l^{(3)}(k_f R_1) \zeta_l^{(3)}(k_a R_1)}{k_f z_l^{(3)}(k_f R_1) \zeta_l^{(1)}(k_a R_1) - k_a z_l^{(1)}(k_a R_1) \zeta_l^{(3)}(k_f R_1)} \tag{3.16}$$

$$B'_{lm} = \left(\frac{k_a}{k_f} \right) \left(\frac{k_a z_l^{(3)}(k_a R_1) \zeta_l^{(1)}(k_a R_1) - k_a z_l^{(1)}(k_a R_1) \zeta_l^{(3)}(k_a R_1)}{k_f z_l^{(3)}(k_f R_1) \zeta_l^{(1)}(k_a R_1) - k_a z_l^{(1)}(k_a R_1) \zeta_l^{(3)}(k_f R_1)} \right) \tag{3.17}$$

The expressions for the reflection and transmission coefficients $\tilde{R}_{af}^{(N)}$ and $\tilde{T}_{af}^{(N)}$ are got from using Eq. 3.16 and 3.17 in Eq. 3.10 and 3.15 respectively.

3.2.2 Analysis for two spheres translated along z-axis

It must be noted that for the case of symmetric boundaries (e.g. such as surface of a single sphere considered in Sec. 3.2.1 or even concentric spherical layers) a $\boldsymbol{M}$ wave will give rise

to only $\boldsymbol{M}$ waves after reflection and transmission at the interface. However when there are asymmetric boundaries (e.g. the configuration which we are analyzing of two spheres with centers translated along z-axis), then each $\boldsymbol{M}$ wave arising from one sphere will give rise to both $\boldsymbol{M}$ and $\boldsymbol{N}$ waves on reflection from the other sphere. The DGF for the configuration shown in Fig. 3.1 for an observation point in the scattered region (vacuum space between the two spheres) can therefore be written as:

$$\overline{\overline{\boldsymbol{G}}}_e(\boldsymbol{r}_a,\boldsymbol{r}'_a) = ik_f \sum_{\substack{l,\nu=(1,m)\\ m=-N_m}}^{\substack{m=N_m\\ l,\nu=N_m}} (-1)^m \left[\begin{array}{l} \left[\begin{array}{l} \left(C^{lM}_{\nu m}\boldsymbol{M}^{(3)}_{\nu m}(k_f\boldsymbol{r}_a) + C^{lN}_{\nu m}\boldsymbol{N}^{(3)}_{\nu m}(k_f\boldsymbol{r}_a)\right)+ \\ \left(D^{lM}_{\nu m}\boldsymbol{M}^{(3)}_{\nu m}(k_f\boldsymbol{r}_b) + D^{lN}_{\nu m}\boldsymbol{N}^{(3)}_{\nu m}(k_f\boldsymbol{r}_b)\right) \end{array} \right] \boldsymbol{M}^{(1)}_{l,-m}(k_a\boldsymbol{r}'_a)+ \\ \left[\begin{array}{l} \left(C'^{lM}_{\nu m}\boldsymbol{M}^{(3)}_{\nu m}(k_f\boldsymbol{r}_a) + C'^{lN}_{\nu m}\boldsymbol{N}^{(3)}_{\nu m}(k_f\boldsymbol{r}_a)\right)+ \\ \left(D'^{lM}_{\nu m}\boldsymbol{M}^{(3)}_{\nu m}(k_f\boldsymbol{r}_b) + D'^{lN}_{\nu m}\boldsymbol{N}^{(3)}_{\nu m}(k_f\boldsymbol{r}_b)\right) \end{array} \right] \boldsymbol{N}^{(1)}_{l,-m}(k_a\boldsymbol{r}'_a) \end{array} \right] \tag{3.18}$$

The position vectors $\boldsymbol{r}_a$ and $\boldsymbol{r}_b$ refer to the same location in space in coordinate systems located at the center of spheres a and b respectively. The coefficients $C^{lM}_{\nu m}$, $D^{lM}_{\nu m}$ etc are found from applying the boundary conditions on the surface of the two spheres similar to that explained for a single sphere above. The magnetic DGF is got from:

$$\begin{aligned} \overline{\overline{\boldsymbol{G}}}_h(\boldsymbol{r}_a,\boldsymbol{r}'_a) &= \boldsymbol{\nabla}\times\overline{\overline{\boldsymbol{G}}}_e(\boldsymbol{r}_a,\boldsymbol{r}'_a) \\ &= ik_f^2 \sum_{\substack{l,\nu=(1,m)\\ m=-N_m}}^{\substack{m=N_m\\ l,\nu=N_m}} (-1)^m \left[\begin{array}{l} \left[\begin{array}{l} \left(C^{lM}_{\nu m}\boldsymbol{N}^{(3)}_{\nu m}(k_f\boldsymbol{r}_a) + C^{lN}_{\nu m}\boldsymbol{M}^{(3)}_{\nu m}(k_f\boldsymbol{r}_a)\right)+ \\ \left(D^{lM}_{\nu m}\boldsymbol{N}^{(3)}_{\nu m}(k_f\boldsymbol{r}_b) + D^{lN}_{\nu m}\boldsymbol{M}^{(3)}_{\nu m}(k_f\boldsymbol{r}_b)\right) \end{array} \right] \boldsymbol{M}^{(1)}_{l,-m}(k_a\boldsymbol{r}'_a)+ \\ \left[\begin{array}{l} \left(C'^{lM}_{\nu m}\boldsymbol{N}^{(3)}_{\nu m}(k_f\boldsymbol{r}_a) + C'^{lN}_{\nu m}\boldsymbol{M}^{(3)}_{\nu m}(k_f\boldsymbol{r}_a)\right)+ \\ \left(D'^{lM}_{\nu m}\boldsymbol{N}^{(3)}_{\nu m}(k_f\boldsymbol{r}_b) + D'^{lN}_{\nu m}\boldsymbol{M}^{(3)}_{\nu m}(k_f\boldsymbol{r}_b)\right) \end{array} \right] \boldsymbol{N}^{(1)}_{l,-m}(k_a\boldsymbol{r}'_a) \end{array} \right] \end{aligned} \tag{3.19}$$

Using Eq. 3.18 and 3.19, an expression for the Poynting vector can be obtained in the following steps. First we use the translation addition theorem (explained in greater detail in Chapter 4) which enables us to express $\boldsymbol{M}^{(3)}_{\nu m}(k_f\boldsymbol{r}_a)$ and $\boldsymbol{N}^{(3)}_{\nu m}(k_f\boldsymbol{r}_a)$ as an expansion series in terms of $\boldsymbol{M}$ and $\boldsymbol{N}$ waves with respect to the coordinate system at the center of the sphere b. This can be written as:

$$\boldsymbol{M}^{(3)}_{\nu m}(k_f\boldsymbol{r}_a) = \sum_n \left[A_{\nu m,nm}\boldsymbol{M}^{(1)}_{nm}(k_f\boldsymbol{r}_b) + B_{\nu m,nm}\boldsymbol{N}^{(1)}_{nm}(k_f\boldsymbol{r}_b)\right] \tag{3.20}$$

$$\boldsymbol{N}^{(3)}_{\nu m}(k_f \boldsymbol{r}_a) = \sum_n \left[B_{\nu m,nm} \boldsymbol{M}^{(1)}_{nm}(k_f \boldsymbol{r}_b) + A_{\nu m,nm} \boldsymbol{N}^{(1)}_{nm}(k_f \boldsymbol{r}_b) \right] \tag{3.21}$$

It must be noted that:

1. In the translation theorem, the outgoing wave from sphere a is expressed in terms of incoming waves from sphere b (and vice-versa)

2. The m subscript in $\boldsymbol{M}^{(3)}_{\nu m}(k_f \boldsymbol{r}_a)$ does not change while applying the translation theorem only because we are dealing with translation only along z-axis. A more general form of the translation theorem would have been

$$\boldsymbol{M}^{(3)}_{\nu m}(k_f \boldsymbol{r}_a) = \sum_{n,m'} \left[A_{\nu m,nm'} \boldsymbol{M}^{(1)}_{nm'}(k_f \boldsymbol{r}_b) + B_{\nu m,nm'} \boldsymbol{N}^{(1)}_{nm'}(k_f \boldsymbol{r}_b) \right] \tag{3.22}$$

Using Eq. 3.20 and 3.21 (and interchanging summations over n and ν) we get:

$$\begin{aligned}
\frac{\overline{\overline{\boldsymbol{G}}}_e(\boldsymbol{r}_a, \boldsymbol{r}'_a)}{ik_f} =& \sum_{l,m,n} (-1)^m \Bigg[\sum_\nu \left(C^{lM}_{\nu m} A_{\nu m,nm} + C^{lN}_{\nu m} B_{\nu m,nm} \right) \boldsymbol{M}^{(1)}_{nm}(k_f \boldsymbol{r}_b) + \\
& \sum_\nu \left(C^{lM}_{\nu m} B_{\nu m,nm} + C^{lN}_{\nu m} A_{\nu m,nm} \right) \boldsymbol{N}^{(1)}_{nm}(k_f \boldsymbol{r}_b) + \\
& \sum_\nu \left[D^{lM}_{\nu m} \boldsymbol{M}^{(3)}_{\nu m}(k_f \boldsymbol{r}_b) + D^{lN}_{\nu m} \boldsymbol{N}^{(3)}_{\nu m}(k_f \boldsymbol{r}_b) \right] \Bigg] \boldsymbol{M}^{(\mathbf{1})}_{l,-m}(k_a \boldsymbol{r}'_a) + \\
\sum_{l,m,n} (-1)^m & \Bigg[\sum_\nu \left(C'^{lM}_{\nu m} A_{\nu m,nm} + C'^{lN}_{\nu m} B_{\nu m,nm} \right) \boldsymbol{M}^{(1)}_{nm}(k_f \boldsymbol{r}_b) + \qquad (3.23) \\
& \sum_\nu \left(C'^{lM}_{\nu m} B_{\nu m,nm} + C'^{lN}_{\nu m} A_{\nu m,nm} \right) \boldsymbol{N}^{(1)}_{nm}(k_f \boldsymbol{r}_b) + \\
& \sum_\nu \left(D'^{lM}_{\nu m} \boldsymbol{M}^{(3)}_{\nu m}(k_f \boldsymbol{r}_b) + D'^{lN}_{\nu m} \boldsymbol{N}^{(3)}_{\nu m}(k_f \boldsymbol{r}_b) \right) \Bigg] \boldsymbol{N}^{(\mathbf{1})}_{l,-m}(k_a \boldsymbol{r}'_a) \qquad (3.24)
\end{aligned}$$

Now use the boundary conditions (Eq. 20c and Eq. 20d in Ref. [36]) to replace the

summations and take the summation over n inside, to get:

$$\frac{\overline{\overline{\boldsymbol{G}}}_e(\boldsymbol{r}_a,\boldsymbol{r}'_a)}{ik_f} = \sum_{l,m}(-1)^m \Bigg[\sum_n \left(\frac{-D^{lM}_{nm}}{u_n(R_2)} \boldsymbol{M}^{(1)}_{nm}(k_f\boldsymbol{r}_b) + \frac{-D^{lN}_{nm}}{v_n(R_2)} \boldsymbol{N}^{(1)}_{nm}(k_f\boldsymbol{r}_b) \right) + \sum_\nu \left[D^{lM}_{\nu m}\boldsymbol{M}^{(3)}_{\nu m}(k_f\boldsymbol{r}_b) + D^{lN}_{\nu m}\boldsymbol{N}^{(3)}_{\nu m}(k_f\boldsymbol{r}_b) \right] \Bigg] \boldsymbol{M}^{(\mathbf{1})}_{l,-m}(k_a\boldsymbol{r}'_a) + \sum_{l,m}(-1)^m \Bigg[\sum_n \left(\frac{-D'^{lM}_{nm}}{u_n(R_2)} \boldsymbol{M}^{(1)}_{nm}(k_f\boldsymbol{r}_b) + \frac{-D'^{lN}_{nm}}{v_n(R_2)} \boldsymbol{N}^{(1)}_{nm}(k_f\boldsymbol{r}_b) \right) + \sum_\nu \left(D'^{lM}_{\nu m}\boldsymbol{M}^{(3)}_{\nu m}(k_f\boldsymbol{r}_b) + D'^{lN}_{\nu m}\boldsymbol{N}^{(3)}_{\nu m}(k_f\boldsymbol{r}_b) \right) \Bigg] \boldsymbol{N}^{(\mathbf{1})}_{l,-m}(k_a\boldsymbol{r}'_a) \quad (3.25)$$

where $u_n(R_2)$ and $v_n(R_2)$ are the Mie scattering coefficients of a sphere of radius R_2. These are equivalent to the the coefficients B_{lm} and A_{lm} given in Eq. 3.14 and 3.9 respectively. Since n is just a dummy variable, we can replace it by ν to give:

$$\frac{\overline{\overline{\boldsymbol{G}}}_e(\boldsymbol{r}_a,\boldsymbol{r}'_a)}{ik_f} = \sum_{l,m}(-1)^m \Bigg[\sum_\nu \left(\frac{-D^{lM}_{\nu m}}{u_\nu(R_2)} \boldsymbol{M}^{(1)}_{\nu m}(k_f\boldsymbol{r}_b) + \frac{-D^{lN}_{\nu m}}{v_\nu(R_2)} \boldsymbol{N}^{(1)}_{\nu m}(k_f\boldsymbol{r}_b) \right) + \sum_\nu \left[D^{lM}_{\nu m}\boldsymbol{M}^{(3)}_{\nu m}(k_f\boldsymbol{r}_b) + D^{lN}_{\nu m}\boldsymbol{N}^{(3)}_{\nu m}(k_f\boldsymbol{r}_b) \right] \Bigg] \boldsymbol{M}^{(\mathbf{1})}_{l,-m}(k_a\boldsymbol{r}'_a) + \sum_{l,m}(-1)^m \Bigg[\sum_\nu \left(\frac{-D'^{lM}_{\nu m}}{u_\nu(R_2)} \boldsymbol{M}^{(1)}_{\nu m}(k_f\boldsymbol{r}_b) + \frac{-D'^{lN}_{\nu m}}{v_\nu(R_2)} \boldsymbol{N}^{(1)}_{\nu m}(k_f\boldsymbol{r}_b) \right) + \sum_\nu \left(D'^{lM}_{\nu m}\boldsymbol{M}^{(3)}_{\nu m}(k_f\boldsymbol{r}_b) + D'^{lN}_{\nu m}\boldsymbol{N}^{(3)}_{\nu m}(k_f\boldsymbol{r}_b) \right) \Bigg] \boldsymbol{N}^{(\mathbf{1})}_{l,-m}(k_a\boldsymbol{r}'_a) \quad (3.26)$$

Splitting the $\boldsymbol{M}$ and $\boldsymbol{N}$ waves in terms of vector spherical harmonics $\boldsymbol{V}^{(1)}_{\nu m}(\theta,\phi)$, $\boldsymbol{V}^{(2)}_{\nu m}(\theta,\phi)$,$\boldsymbol{V}^{(3)}_{\nu m}(\theta,\phi)$

using Eq. 2.16 and Eq. 2.17:

$$\begin{aligned}\frac{\overline{\overline{\boldsymbol{G}}}_e(\boldsymbol{r}_a,\boldsymbol{r}'_a)}{ik_f} = &\sum_{l,m,\nu}(-1)^m\Bigg[D^{lM}_{\nu m}\left(z^{(3)}_\nu(x)-\frac{z^{(1)}_\nu(x)}{u_\nu(R_2)}\right)\boldsymbol{V}^{(2)}_{\nu m}+D^{lN}_{\nu m}\left(\zeta^{(3)}_\nu(x)-\frac{\zeta^{(1)}_\nu(x)}{v_\nu(R_2)}\right)\boldsymbol{V}^{(3)}_{\nu m}\\ &+D^{lN}_{\nu m}\left(\frac{z^{(3)}_\nu}{x}-\frac{z^{(1)}_\nu(x)/x}{v_\nu(R_2)}\right)\sqrt{\nu(\nu+1)}\boldsymbol{V}^{(1)}_{\nu m}\Bigg]\boldsymbol{M}^{(\mathbf{1})}_{l,-m}(k_a\boldsymbol{r}'_a)\\ &+\sum_{l,m,\nu}(-1)^m\Bigg[D'^{lM}_{\nu m}\left(z^{(3)}_\nu(x)-\frac{z^{(1)}_\nu(x)}{u_\nu(R_2)}\right)\boldsymbol{V}^{(2)}_{\nu m}+D'^{lN}_{\nu m}\left(\zeta^{(3)}_\nu(x)-\frac{\zeta^{(1)}_\nu(x)}{v_\nu(R_2)}\right)\boldsymbol{V}^{(3)}_{\nu m}\\ &+D'^{lN}_{\nu m}\left(\frac{z^{(3)}_\nu}{x}-\frac{z^{(1)}_\nu(x)/x}{v_\nu(R_2)}\right)\sqrt{\nu(\nu+1)}\boldsymbol{V}^{(1)}_{\nu m}\Bigg]\boldsymbol{N}^{(\mathbf{1})}_{l,-m}(k_a\boldsymbol{r}'_a)\end{aligned}\tag{3.27}$$

where $x = k_f R_2$. Similarly for $\overline{\overline{\boldsymbol{G}}}_h$ we have from Eq. 3.19:

$$\begin{aligned}\frac{\overline{\overline{\boldsymbol{G}}}_h(\boldsymbol{r}_a,\boldsymbol{r}'_a)}{ik_f^2}=&\sum_{l,m}(-1)^m\Bigg[\sum_\nu\left(\frac{-D^{lM}_{\nu m}}{u_\nu(R_2)}\boldsymbol{N}^{(1)}_{\nu m}(k_f\boldsymbol{r}_b)+\frac{-D^{lN}_{\nu m}}{v_\nu(R_2)}\boldsymbol{M}^{(1)}_{\nu m}(k_f\boldsymbol{r}_b)\right)+\\ &\sum_\nu\left(D^{lM}_{\nu m}\boldsymbol{N}^{(3)}_{\nu m}(k_f\boldsymbol{r}_b)+D^{lN}_{\nu m}\boldsymbol{N}^{(3)}_{\nu m}(k_f\boldsymbol{r}_b)\right)\Bigg]\boldsymbol{M}^{(\mathbf{1})}_{l,-m}(k_a\boldsymbol{r}'_a)+\\ &\sum_{l,m}(-1)^m\Bigg[\sum_\nu\left(\frac{-D'^{lM}_{\nu m}}{u_\nu(R_2)}\boldsymbol{N}^{(1)}_{\nu m}(k_f\boldsymbol{r}_b)+\frac{-D'^{lN}_{\nu m}}{v_\nu(R_2)}\boldsymbol{M}^{(1)}_{\nu m}(k_f\boldsymbol{r}_b)\right)+\\ &\sum_\nu\left(D'^{lM}_{\nu m}\boldsymbol{N}^{(3)}_{\nu m}(k_f\boldsymbol{r}_b)+D'^{lN}_{\nu m}\boldsymbol{N}^{(3)}_{\nu m}(k_f\boldsymbol{r}_b)\right)\Bigg]\boldsymbol{N}^{(\mathbf{1})}_{l,-m}(k_a\boldsymbol{r}'_a)\end{aligned}\tag{3.28}$$

which simplifies to:

$$\begin{aligned}\frac{\overline{\overline{\boldsymbol{G}}}_h(\boldsymbol{r}_a,\boldsymbol{r}'_a)}{ik_f^2} = &\sum_{l,m,\nu}(-1)^m\Bigg[D^{lN}_{\nu m}\left(z^{(3)}_\nu(x)-\frac{z^{(1)}_\nu(x)}{v_\nu(R_2)}\right)\boldsymbol{V}^{(2)}_{\nu m}+D^{lM}_{\nu m}\left(\zeta^{(3)}_\nu(x)-\frac{\zeta^{(1)}_\nu(x)}{u_\nu(R_2)}\right)\boldsymbol{V}^{(3)}_{\nu m}\\ &+D^{lM}_{\nu m}\left(\frac{z^{(3)}_\nu}{x}-\frac{z^{(1)}_\nu(x)/x}{u_\nu(R_2)}\right)\sqrt{\nu(\nu+1)}\boldsymbol{V}^{(1)}_{\nu m}\Bigg]\boldsymbol{M}^{(\mathbf{1})}_{l,-m}(k_a\boldsymbol{r}'_a)\\ &+\sum_{l,m,\nu}(-1)^m\Bigg[D'^{lN}_{\nu m}\left(z^{(3)}_\nu(x)-\frac{z^{(1)}_\nu(x)}{v_\nu(R_2)}\right)\boldsymbol{V}^{(2)}_{\nu m}+D'^{lM}_{\nu m}\left(\zeta^{(3)}_\nu(x)-\frac{\zeta^{(1)}_\nu(x)}{u_\nu(R_2)}\right)\boldsymbol{V}^{(3)}_{\nu m}\\ &+D'^{lM}_{\nu m}\left(\frac{z^{(3)}_\nu}{x}-\frac{z^{(1)}_\nu(x)/x}{u_\nu(R_2)}\right)\sqrt{\nu(\nu+1)}\boldsymbol{V}^{(1)}_{\nu m}\Bigg]\boldsymbol{N}^{(\mathbf{1})}_{l,-m}(k_a\boldsymbol{r}'_a)\end{aligned}\tag{3.29}$$

As shown in Sec. 2.6 the ensemble average Poynting vector $\langle\boldsymbol{S}\rangle$ at any position $\boldsymbol{r}$ can be expressed in terms of the factor $\langle E_i(\boldsymbol{r}_1,\omega)H*_j(\boldsymbol{r}_1,\omega)\rangle$, where,

$$\langle E_i(\boldsymbol{r}_1,\omega)H*_j(\boldsymbol{r}_1,\omega)\rangle=\frac{i\epsilon_0\epsilon''(\omega)\mu_0\omega^2\Theta(\omega,T)}{\pi}\int_V d^3r'[\boldsymbol{G}_e(\boldsymbol{r}_1,\boldsymbol{r}',\omega).\boldsymbol{G}^{*T}_h(\boldsymbol{r}_1,\boldsymbol{r}',\omega)]_{ij}\tag{3.30}$$

For this we need the dot product of $\boldsymbol{G}_e$, given by the quantity in Eq. 3.27 and $\boldsymbol{G}_h^*$, given by the transpose conjugate of the quantity given in Eq. 3.29. For this we make use of the fact that $\boldsymbol{M}$ and $\boldsymbol{N}$ waves are mutually orthogonal and use the relations Ref. [36] (since we have an integral over $\boldsymbol{r'}$ we will require integral over $\boldsymbol{M}_{l,-m}^{(1)}(k_s\boldsymbol{r'}).\boldsymbol{M}_{l,-m}^{*(1)}(k_s\boldsymbol{r'})$) :

$$k_f^2\varepsilon_a^{''}\int_{V_a}\boldsymbol{M}_{lm}^{(1)}(k_a\boldsymbol{r'})\boldsymbol{M}_{pq}^{(1)*}(k_a\boldsymbol{r'})d\boldsymbol{r'}=\delta_{lp}\delta_{mq}R_1\ \mathrm{Im}[k_a^*R_1z_l^{(1)}(k_aR_1)\zeta^{(1)*}(k_aR_1)] \tag{3.31}$$

and

$$k_f^2\varepsilon_a^{''}\int_{V_a}\boldsymbol{N}_{lm}^{(1)}(k_a\boldsymbol{r'})\boldsymbol{N}_{pq}^{(1)*}(k_a\boldsymbol{r'})d\boldsymbol{r'}=\delta_{lp}\delta_{mq}R_1\ \mathrm{Im}[k_a^*R_1z_l^{(1)*}(k_aR_1)\zeta^{(1)}(k_aR_1)] \tag{3.32}$$

Once the ensemble average Poynting vector $\langle\boldsymbol{S}\rangle$ at any position $\boldsymbol{r}$ is calculated, since we want the net energy seeping into the sphere, we actually would need to take the following integral over the surface area of the sphere b, S_b:

$$Q_{a\to b}(\omega,T)=\oint_{S_b}\boldsymbol{S}.\hat{\boldsymbol{r}}\ dA$$

i.e.

$$Q_{a\to b}(\omega,T)=\int_0^{2\pi}\int_0^{\pi}\boldsymbol{S}.\hat{\boldsymbol{r}}\ R_2^2\sin\theta\ d\theta\,d\phi \tag{3.33}$$

where T is the temperature of the sphere a. It is possible to define a linearized thermal conductance G (units WK^{-1}) between the two spheres as:

$$G=\lim_{T_1\to T_2}\frac{Q(T_1,T_2)}{T_1-T_2}, \tag{3.34}$$

where $Q\left(T_1,T_2\right)$ is the rate of heat transfer between the two spheres at temperatures T_1 and T_2. In terms of the quantity $Q_{a\to b}(\omega,T)$ given in Eq. 3.33, we get an expression for the conductance G as:

$$G(\omega,T)=\frac{d}{dT}Q_{a\to b}(\omega,T), \tag{3.35}$$

For calculating the integral in Eq. 3.33, the following relations from Ref. [36] would have to

be made use of:

$$\oint_{\Omega} \left(\boldsymbol{V}_{lm}^{(s)}(\theta,\phi) \times \boldsymbol{V}_{pq}^{(s)*}(\theta,\phi) \right) \boldsymbol{.}\, \hat{\boldsymbol{r}} d\Omega = 0 \tag{3.36}$$

$$\oint_{\Omega} \left(\boldsymbol{V}_{lm}^{(2)}(\theta,\phi) \times \boldsymbol{V}_{pq}^{(3)*}(\theta,\phi) \right) \boldsymbol{.}\, \hat{\boldsymbol{r}} d\Omega = \delta_{lp}\delta_{mq} \tag{3.37}$$

$$\oint_{\Omega} \left(\boldsymbol{V}_{lm}^{(3)}(\theta,\phi) \times \boldsymbol{V}_{pq}^{(2)*}(\theta,\phi) \right) \boldsymbol{.}\, \hat{\boldsymbol{r}} d\Omega = -\delta_{lp}\delta_{mq} \tag{3.38}$$

Using these integrals in Eq. 3.33 the expression for the radiative conductance $G(\omega, T)$ in Eq. 3.35 can be obtained as (Eq. 28 in Ref. [36]):

$$\begin{aligned} G(\omega,T) =& \frac{R_2}{R_1}\frac{d\Theta}{dT}(\omega,T)\times \\ & \sum_{l,m,\nu} \begin{bmatrix} \left[\mathrm{Im}\left(\frac{1}{x_\nu(R_2)}\right) \left|\tilde{D}_{\nu m}^{lM}\right|^2 - \mathrm{Im}\left(\frac{1}{y_\nu(R_2)}\right) \left|\tilde{D}_{\nu m}^{lN}\right|^2 \right] \mathrm{Im}\left(\frac{1}{x_l(R_2)}\right) |x_l(R_2)|^2 + \\ \left[\mathrm{Im}\left(\frac{1}{x_\nu(R_2)}\right) \left|\tilde{D'}_{\nu m}^{lM}\right|^2 - \mathrm{Im}\left(\frac{1}{y_\nu(R_2)}\right) \left|\tilde{D'}_{\nu m}^{lN}\right|^2 \right] \mathrm{Im}\left(\frac{1}{y_l(R_2)}\right) |y_l(R_2)|^2 \end{bmatrix} \end{aligned} \tag{3.39}$$

where,

$$x_\nu(R_2) = k_b R_2 \zeta_\nu^{(1)}(k_b R_2) z_\nu^{(1)}(k_f R_2) - k_f R_2 \zeta_\nu^{(1)}(k_f R_2) z_\nu^{(1)}(k_b R_2) \tag{3.40}$$

$$y_\nu(R_2) = k_b R_2 \zeta_\nu^{(1)}(k_f R_2) z_\nu^{(1)}(k_b R_2) - k_f R_2 \zeta_\nu^{(1)}(k_b R_2) z_\nu^{(1)}(k_f R_2) \tag{3.41}$$

and the normalized coefficients

$$\begin{aligned} \tilde{D}_{\nu m}^{lM} &= \frac{z_l^{(1)}(k_a R_1)}{z_\nu^{(1)}(k_f R_2)} D_{\nu m}^{lM} \\ \tilde{D}_{\nu m}^{lN} &= \frac{z_l^{(1)}(k_a R_1)}{\zeta_\nu^{(1)}(k_f R_2)} D_{\nu m}^{lN} \\ \tilde{D'}_{\nu m}^{lM} &= \frac{\zeta_l^{(1)}(k_a R_1)}{z_\nu^{(1)}(k_f R_2)} D_{\nu m}^{\prime lM} \\ \tilde{D'}_{\nu m}^{lN} &= \frac{\zeta_l^{(1)}(k_a R_1)}{\zeta_\nu^{(1)}(k_f R_2)} D_{\nu m}^{\prime lN} \end{aligned} \tag{3.42}$$

The process of normalization is explained in greater detail in Chapter 4.

To conclude, it must be mentioned that this chapter does not present any new findings. The intention of the chapter is to explain the theoretical foundations for computing the

radiative transfer between two spheres that has been developed earlier in literature. I have shown explicitly the derivations to arrive at some of the analytical expressions listed in Ref. [36].

Chapter 4

Translation addition theorem

4.1 Introduction

An important component of the analysis of multi-body electromagnetic scattering problems is the usage of translation addition theorem to facilitate the application of boundary conditions on the surface of the adjacent objects. In particular, for the two-sphere problem, the vector addition theorem allows us to expand the electromagnetic field in terms of vector spherical waves from each of the spheres and then re-expand the vector spherical waves from one sphere in terms of the vector spherical waves from the second sphere. The efficient computation of the translation coefficients for the scalar and vector addition theorems is thus of significance, especially when the number of terms required for convergence in the vector spherical wave expansion is large - which is the case in near-field electromagnetic scattering problems.

In this chapter an introduction to the translation addition theorem has been given in Sec. 4.2 and the recurrence relations that have been developed in literature to compute the translation coefficients are described in Sec. 4.3. A method to normalize the translation coefficients which helps avoid the possibility of encountering divergent numbers (numbers too large for a given floating point format on a computer) during the calculation of coefficients of the translation addition theorem is discussed in Sec. 4.4.

4.2 Definitions for vector spherical waves and vector translation coefficients

The simplest case of a multi-particle system is that of two spheres whose centers are translated along the z-axis as shown in Fig. 3.1. For convenience, the configuration has been re-drawn in Fig. 4.1 with the parameters relevant for this chapter highlighted. Emission and scattering of electromagnetic waves from such a system involves solving the vector wave equation given in Eq. 2.15 (repeated here for convenience):

$$\boldsymbol{\nabla} \times \boldsymbol{\nabla} \times \boldsymbol{X}(\boldsymbol{r}, \omega) - k^2 \boldsymbol{X}(\boldsymbol{r}, \omega) = 0; \qquad \text{(2.15 revisited)}$$

where, $\boldsymbol{X}(\boldsymbol{r}, \omega)$ is the electric or magnetic field at position vector $\boldsymbol{r}$ and k is the frequency dependent wave propagation constant. Following the notation in Fig. 4.1, $k = k_f = \omega/c$ in the free-space region; $k = k_a = n_a(\omega)\,\omega/c$ inside sphere a; and $k = k_b = n_b(\omega)\,\omega/c$ inside sphere b with $n_a(\omega)$ and $n_b(\omega)$ being the complex refractive indices of sphere a and sphere b respectively. The independent divergence-free solutions of the vector wave equation in spherical coordinates are given in Eqs. 2.16 and 2.17 (and repeated here for completeness):

$$\boldsymbol{M}_{nm}^{(p)}(k\boldsymbol{r}) = z_n^{(p)}(kr)\boldsymbol{V}_{nm}^{(2)}(\theta, \phi); \qquad \text{(2.16 revisited)}$$

$$\boldsymbol{N}_{nm}^{(p)}(k\boldsymbol{r}) = \zeta_n^{(p)}(kr)\boldsymbol{V}_{nm}^{(3)}(\theta, \phi) + \frac{z_n^{(p)}(kr)}{kr}\sqrt{n(n+1)}\boldsymbol{V}_{nm}^{(1)}(\theta, \phi); \qquad \text{(2.17 revisited)}$$

The symbols and notations are explained in Sec. 2.1.

Following Ref. [73] these vector spherical waves can also be expressed in terms of the solutions to the scalar Helmholtz equation. The solutions of the scalar Helmholtz equation $\boldsymbol{\nabla}^2\psi + k^2\psi = 0$ are given by:

$$\psi_{nm}^{(p)}(k, \boldsymbol{r}) = z_n^{(p)}(kr)Y_{nm}(\theta, \phi) \qquad (4.1)$$

where, ψ_{nm} are scalar spherical waves of the same order (n, m) and $Y_{nm}(\theta, \phi)$ represent the spherical harmonics. Using these the vector spherical waves can be expressed as:

$$\boldsymbol{M}_{nm}^{(p)}(k, \boldsymbol{r}) = \frac{1}{\sqrt{n(n+1)}}\boldsymbol{\nabla} \times \left[\boldsymbol{r}\psi_{nm}^{(p)}(k, \boldsymbol{r})\right] \qquad (4.2)$$

$$\boldsymbol{N}_{nm}^{(p)}(k,\boldsymbol{r}) = \frac{1}{\sqrt{n(n+1)}}\frac{1}{k}\boldsymbol{\nabla}\times\boldsymbol{\nabla}\times\left[\boldsymbol{r}\psi_{nm}^{(p)}(k,\boldsymbol{r})\right] \tag{4.3}$$

The representations for $\boldsymbol{M}$ and $\boldsymbol{N}$ waves in Eq. 2.16, 2.17 and Eq. 4.2, 4.3 are equivalent, and differ from the corresponding representations in Ref. [73] in only a factor $(1/\sqrt{n(n+1)})$ which has been introduced to ensure that the vector spherical waves are orthonormal to each other for integration over θ and ϕ.

The scalar addition theorem for the scalar spherical waves ψ_{nm} is given by:

$$\psi_{nm}(k,\boldsymbol{r}_a) = \sum_{\nu m'}\psi_{\nu m'}(k,\boldsymbol{r}_b)\beta_{\nu m',nm} \tag{4.4}$$

and the vector addition theorem for the vector spherical waves $\boldsymbol{M}_{nm}$ and $\boldsymbol{N}_{nm}$ waves are given by Eqs. 3.20 and 3.21 (and repeated here for completeness):

$$\boldsymbol{M}_{nm}(k,\boldsymbol{r}_a) = \sum_{\nu,m}\left[\boldsymbol{M}_{\nu m}(k,\boldsymbol{r}_b)A_{\nu m,nm} + \boldsymbol{N}_{\nu m}(k,\boldsymbol{r}_b)B_{\nu m,nm}\right] \tag{3.20 revisited}$$

$$\boldsymbol{N}_{nm}(k,\boldsymbol{r}_a) = \sum_{\nu,m}\left[\boldsymbol{N}_{\nu m}(k,\boldsymbol{r}_b)A_{\nu m,nm} + \boldsymbol{M}_{\nu m}(k,\boldsymbol{r}_b)B_{\nu m,nm}\right] \tag{3.21 revisited}$$

where $\boldsymbol{r}_a$ and $\boldsymbol{r}_b$ are coordinates of the same point with respect to the coordinate systems centered at O and O' respectively as shown in Fig. 4.1. Here $\boldsymbol{r}_a = \boldsymbol{r}_b + \boldsymbol{D}$. Since the definition of the vector spherical waves $\boldsymbol{M}_{nm}(k,\boldsymbol{r}_a)$ and $\boldsymbol{N}_{nm}(k,\boldsymbol{r}_a)$ differs in literature (see Ref. [73], Ref. [36]), the formulae for the vector translation coefficients will differ accordingly. The superscripts *'Chew'* and *'AN'* has been used to refer to the definitions according to Ref. [73] and Ref. [36] respectively. The following steps indicate how we can change from one representation to another. Consider first the vector addition theorem with the definitions of $\boldsymbol{M}_{nm}(k,\boldsymbol{r}_a)$, $\boldsymbol{N}_{nm}(k,\boldsymbol{r}_a)$, $A_{\nu m,nm}$, and $B_{\nu m,nm}$ according to Ref. [73]:

$$\boldsymbol{M}_{nm}^{Chew}(k,\boldsymbol{r}_a) = \sum_{\nu m}\left[\boldsymbol{M}_{\nu m}^{Chew}(k,\boldsymbol{r}_b)A_{\nu m,nm}^{Chew} + \boldsymbol{N}_{\nu m}^{Chew}(k,\boldsymbol{r}_b)B_{\nu m,nm}^{Chew}\right] \tag{4.5}$$

This equation can be converted to reflect the definitions given in Ref. [36] by using the factor $1/\sqrt{n(n+1)}$.

$$\frac{\boldsymbol{M}_{nm}^{Chew}(k,\boldsymbol{r}_a)}{\sqrt{n(n+1)}} = \sum_{\nu m}\left[\frac{\boldsymbol{M}_{\nu m}^{Chew}(k,\boldsymbol{r}_b)}{\sqrt{n(n+1)}}A_{\nu m,nm}^{Chew} + \frac{\boldsymbol{N}_{\nu m}^{Chew}(k,\boldsymbol{r}_b)}{\sqrt{n(n+1)}}B_{\nu m,nm}^{Chew}\right] \tag{4.6}$$

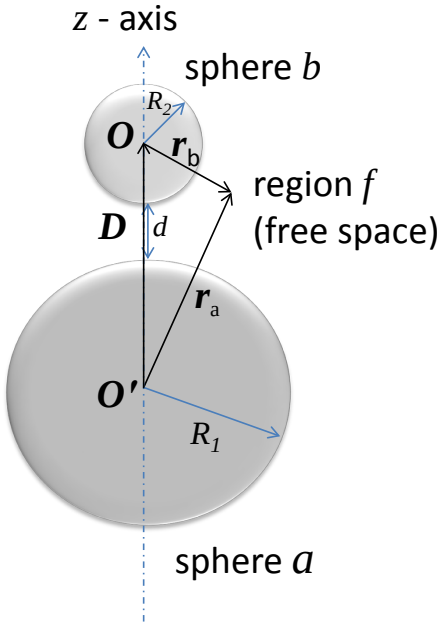

Figure 4.1: The configuration for this study consisting of two spheres of unequal radii R_1 and R_2 (labeled sphere a and sphere b respectively) and the position vectors $\boldsymbol{r}_a$, $\boldsymbol{r}_b$ and $\boldsymbol{D}$. The minimum surface to surface gap between the two spheres d is given by $d = D - R_1 - R_2$

$$\Leftrightarrow \boldsymbol{M}_{nm}^{AN}(k,\boldsymbol{r}_a) = \sum_{\nu m}\left[\frac{\boldsymbol{M}_{\nu m}(k,\boldsymbol{r}_b)}{\sqrt{n(n+1)}}\sqrt{\frac{\nu(\nu+1)}{\nu(\nu+1)}}A_{\nu m,nm}^{Chew} + \frac{\boldsymbol{N}_{\nu m}(k,\boldsymbol{r}_b)}{\sqrt{n(n+1)}}\sqrt{\frac{\nu(\nu+1)}{\nu(\nu+1)}}B_{\nu m,nm}^{Chew}\right] \tag{4.7}$$

$$\Leftrightarrow \boldsymbol{M}_{nm}^{AN}(k,\boldsymbol{r}_a) = \sum_{\nu m}\left[\boldsymbol{M}_{\nu m}^{AN}(k,\boldsymbol{r}_b)\sqrt{\frac{\nu(\nu+1)}{n(n+1)}}A_{\nu m,nm}^{Chew} + \boldsymbol{N}_{\nu m}^{AN}(k,\boldsymbol{r}_b)\sqrt{\frac{\nu(\nu+1)}{n(n+1)}}B_{\nu m,nm}^{Chew}\right] \tag{4.8}$$

Therefore we have:

$$A_{\nu m,nm}^{AN} = \sqrt{\frac{\nu(\nu+1)}{n(n+1)}}A_{\nu m,nm}^{Chew} \tag{4.9}$$

and

$$B_{\nu m,nm}^{AN} = \sqrt{\frac{\nu(\nu+1)}{n(n+1)}}B_{\nu m,nm}^{Chew} \tag{4.10}$$

The superscripts *Chew* and *AN* have been dropped for the formulae later on in this work, noting that by default the definitions from Ref. [36] has been used for deriving all

other relations.

4.3 Computing the vector translation coefficients

The coefficients of the vector addition theorem $A_{\nu m',nm}$ and $B_{\nu m',nm}$ can be expressed in terms of summation over Wigner 3j symbols [74] calculating which involve computations of a large number of factorials. For the configuration shown in Fig. 4.1 (with $m = m'$ due to axisymmetry condition) the vector translation coefficients are given by (using $k = k_f$ for the coordinate systems O and O' positioned in free-space):

$$A_{\nu m,nm} = \sqrt{\frac{\nu(\nu+1)}{n(n+1)}}\frac{2\pi}{\nu(\nu+1)}\sum_p [n(n+1)+\nu(\nu+1)-p(p+1)]\times \\ i^{\nu+p-n}\,\psi_{p,0}(k_f D)\;A(m,n,-m,\nu,p) \tag{4.11}$$

$$B_{\nu m,n,m} = \frac{imk_f D}{\sqrt{\nu(\nu+1)n(n+1)}}\sum_p i^{\nu+p-n}\,\psi_{p,0}(k_f D)\,A(m,n,-m,\nu,p) \tag{4.12}$$

where,

$$A(m,n,-m,\nu,p) = (-1)^m\sqrt{\frac{(2n+1)(2\nu+1)(2p+1)}{4\pi}}\times \\ \begin{pmatrix} n & \nu & p \\ 0 & 0 & 0 \end{pmatrix}\begin{pmatrix} n & \nu & p \\ -m & m & 0 \end{pmatrix} \tag{4.13}$$

with the symbol $\begin{pmatrix} n & \nu & p \\ m & \mu & q \end{pmatrix}$ representing the Wigner 3j coefficient [74]. The above relations differ from those that are given in Ref. [75] due to the different definitions of $\boldsymbol{M}_{nm}^{(p)}(k\boldsymbol{r})$ and $\boldsymbol{N}_{nm}^{(p)}(k\boldsymbol{r})$ waves that we are using (given in Eq. 4.2 and 4.3). The corresponding scalar coefficient $\beta_{\nu m,nm}$ is given by (Eq. 25 in Ref. [75] modified to reflect axisymmetry condition for our configuration):

$$\beta_{\nu m,nm}(k_f D) = \sum_p 4\pi\, i^{\nu+p-n} z_p^{(3)}(k_f D)\sqrt{\frac{2p+1}{4\pi}}A(m,n,-m,\nu,p) \tag{4.14}$$

When large number of coefficients are required computation of these Wigner 3j symbols becomes computationally tedious. To overcome this complexity, recursion relations derived for the scalar addition theorem [76] and the vector addition theorem [73] can be used, which result in reduced computational times. The recursion relation for the scalar translation coefficient β is given by (Eq. 23 and Eq. 27 in Ref. [76]):

$$\beta_{\nu m,n+1,m} = \frac{-a^-_{nm}\,\beta_{\nu m,n-1,m} + a^+_{\nu-1,m}\beta_{\nu-1\,m,nm} + a^-_{\nu+1,m}\beta_{\nu+1\,m,nm}}{a^+_{nm}} \tag{4.15}$$

and

$$\beta_{\nu\,n+1,n+1\,n+1} = \frac{b^+_{\nu-1,n}\,\beta_{\nu-1\,n,nn} + b^-_{\nu+1,n}\,\beta_{\nu+1\,n,nn}}{b^+_{nn}} \tag{4.16}$$

The form of the constants a^+_{nm}, a^-_{nm} and b^+_{nm}, b^-_{nm} have been retained from Ref. [76]. Since the vector translation coefficients $A_{\nu m,nm}$ and $B_{\nu m,nm}$ can be related to β, they are computed directly from β as (Eq. 12a and Eq. 12b in Ref. [73] changed according to the axisymmetry of our configuration and definition of $\boldsymbol{M}$ and $\boldsymbol{N}$ waves)

$$\begin{aligned} A_{\nu m,nm} = \sqrt{\frac{\nu(\nu+1)}{n(n+1)}}\beta_{\nu m,nm} &+ \sqrt{\frac{\nu(\nu+1)}{n(n+1)}}\frac{k_f D}{\nu+1}\sqrt{\frac{(\nu+m+1)(\nu-m+1)}{(2\nu+1)(2\nu+3)}}\beta_{\nu+1,m,nm} \\ &+ \sqrt{\frac{\nu(\nu+1)}{n(n+1)}}\frac{k_f D}{\nu}\sqrt{\frac{(\nu+m)(\nu-m)}{(2\nu-1)(2\nu+1)}}\beta_{\nu-1,m,nm} \end{aligned} \tag{4.17}$$

$$B_{\nu m,n,m} = \frac{imk_f D}{\sqrt{\nu(\nu+1)n(n+1)}}\beta_{\nu m,n,m} \tag{4.18}$$

4.4 Normalizing the translation coefficients

To initialize the recursion for the scalar translation coefficient the following expression is used:

$$\beta_{\nu 0,00} = (-1)^\nu\sqrt{2\nu+1}\; z^{(3)}_\nu(k_f D) \tag{4.19}$$

where, $z_\nu^{(3)}(k_f D)$ represents the spherical Hankel function. When $\nu \gg k_f D$, spherical Hankel and Bessel functions can be approximated by the following asymptotic forms:

$$z_\nu^{(3)}(k_f D) \approx i\sqrt{\frac{4}{(2\nu+1)k_f D}}\left(\frac{2\nu+1}{e k_f D}\right)^{(\nu+1/2)} \tag{4.20}$$

$$z_\nu^{(1)}(k_f D) \approx \sqrt{\frac{4}{(2\nu+1)k_f D}}\left(\frac{e k_f D}{2\nu+1}\right)^{(\nu+1/2)} \tag{4.21}$$

It follows from Eq. 4.20 and Eq. 4.21 that evaluating spherical Hankel and Bessel functions in the limit $\nu \gg k_f D$ can lead to numbers too large or too small for a given floating point format on a computer. For instance, the maximum and minimum positive floating point numbers for double precision floating point format are $1.7976\times10^{+308}$ and 2.225×10^{-308} respectively (both approximate). However, since products of such large and small terms are important for subsequent calculations, we need to modify the algorithm so that evaluations such large or small numbers can be minimized. This can be achieved through the "normalization" of the translation coefficients with appropriate factors, which has been explained below. A careful look at the form of the spectral radiative conductance (Eq.28 in Ref. [36]) gives us a hint on the appropriate factors. It is observed that coefficients $D_{\nu m}^{lM}$ and $D_{\nu m}^{lN}$ which represent the coefficients of $\boldsymbol{M}$ and $\boldsymbol{N}$ waves in the scattered field in vacuum (Eq. 19 in Ref. [36]) are accompanied by factors of the form $\left(z_l^{(1)}(k_a R_1)/z_\beta^{(1)}(k_f R_2)\right)$ and $\left(z_l^{(1)}(k_a R_1)/\zeta_\beta^{(1)}(k_f R_2)\right)$ respectively. Hence, what is important for the computation of the radiative energy transfer is not the terms $D_{\nu m}^{lM}$ and $D_{\nu m}^{lN}$ themselves but $\left(D_{\nu m}^{lM} z_l^{(1)}(k_a R_1)/z_\beta^{(1)}(k_f R_2)\right)$ and $\left(D_{\nu m}^{lN} z_l^{(1)}(k_a R_1)/\zeta_\beta^{(1)}(k_f R_2)\right)$.

These factors can be used in the coupled linear equations for the coefficients of vector spherical waves in vacuum (Eq. 20 in Ref. [36]) to arrive at different forms of the normalizing factors for the translation coefficients $A_{\nu m,nm}$ and $B_{\nu m,nm}$ as has been shown below. The coupled linear equations are given by:

$$C_{nm}^{lM} + \overline{u}_n(a)\frac{z_n^{(1)}(k_f R_1)}{z_n^{(3)}(k_f R_1)}\sum_{\nu=(m,1)}^{N_{max}}\begin{bmatrix} D_{\nu m}^{lM} A_{\nu m,nm}(-k_f D) \\ +D_{\nu m}^{lN} B_{\nu m,nm}(-k_f D)\end{bmatrix} = p_N^M \delta_{Nl} \tag{4.22a}$$

$$D_{nm}^{lM} + \overline{u}_n(R_2)\frac{z_n^{(1)}(k_f R_2)}{z_n^{(3)}(k_f R_2)} \sum_{\nu=(m,1)}^{N_{max}} \begin{bmatrix} C_{\nu m}^{lM} A_{\nu m,nm}(+k_f D) \\ +C_{\nu m}^{lN} B_{\nu m,nm}(+k_f D) \end{bmatrix} = 0 \tag{4.22b}$$

$$C_{nm}^{lN} + \overline{v}_n(a)\frac{z_n^{(1)}(k_f R_1)}{z_n^{(3)}(k_f R_1)} \sum_{\nu=(m,1)}^{N_{max}} \begin{bmatrix} D_{\nu m}^{lM} B_{\nu m,nm}(-k_f D) \\ +D_{\nu m}^{lN} A_{\nu m,nm}(-k_f D) \end{bmatrix} = 0 \tag{4.22c}$$

$$D_{nm}^{lN} + \overline{v}_n(R_2)\frac{z_n^{(1)}(k_f R_2)}{z_n^{(3)}(k_f R_2)} \sum_{\nu=(m,1)}^{N_{max}} \begin{bmatrix} C_{\nu m}^{lM} B_{\nu m,nm}(+k_f D) \\ +C_{\nu m}^{lN} A_{\nu m,nm}(+k_f D) \end{bmatrix} = 0 \tag{4.22d}$$

where:

$$\overline{u}_n(R_1) = \left(\frac{k_b \dfrac{z_{n+1}^{(1)}(k_b R_1)}{z_n^{(1)}(k_b R_1)} - k_f \dfrac{z_{n+1}^{(1)}(k_f R_1)}{z_n^{(1)}(k_f R_1)}}{k_b \dfrac{z_{n+1}^{(1)}(k_b R_1)}{z_n^{(1)}(k_b R_1)} - k_f \dfrac{z_{n+1}^{(3)}(k_f R_1)}{z_n^{(3)}(k_f R_1)}} \right) \tag{4.23}$$

and

$$\overline{v}_n(R_1) = \left(\frac{k_b R_1 \dfrac{z_{n+1}^{(1)}(k_f R_1)}{z_n^{(1)}(k_f R_1)} - k_f R_1 \dfrac{z_{n+1}^{(1)}(k_b R_1)}{z_n^{(1)}(k_b R_1)} + (n+1)\left(\dfrac{k_f}{k_b} - \dfrac{k_b}{k_f}\right)}{k_b R_1 \dfrac{z_{n+1}^{(1)}(k_f R_1)}{z_n^{(1)}(k_f R_1)} - k_f R_1 \dfrac{z_{n+1}^{(3)}(k_b R_1)}{z_n^{(3)}(k_b R_1)} + (n+1)\left(\dfrac{k_f}{k_b} - \dfrac{k_b}{k_f}\right)} \right) \tag{4.24}$$

And similarly $\overline{u}_n(R_2)$ and $\overline{v}_n(R_2)$. For convenience of illustration the steps involved are shown for one of the equations (Eq. 4.22b). Using the normalizing factors for D_{nm}^{lM} Eq. 4.22b can be written as:

$$\frac{z_l^{(1)}(k_a R_1)}{z_n^{(1)}(k_f R_2)} D_{nm}^{lM} + \overline{u}_n(R_2)\frac{z_l^{(1)}(k_a R_1)}{\cancel{z_n^{(1)}(k_f R_2)}}\frac{\cancel{z_n^{(1)}(k_f R_2)}}{z_n^{(3)}(k_f R_2)} \sum_{\nu=(m,1)}^{N_{max}} \begin{bmatrix} C_{\nu m}^{lM} A_{\nu m,nm}(+k_f D)+ \\ C_{\nu m}^{lN} B_{\nu m,nm}(+k_f D) \end{bmatrix} = 0 \tag{4.25}$$

The equivalent normalizing factors for C_{nm}^{lM} and C_{nm}^{lN} are $\frac{z_l^{(1)}(k_b R_2)}{z_\nu^{(1)}(k_f R_1)}$ and $\frac{z_l^{(1)}(k_b R_2)}{\zeta_\nu^{(1)}(k_f R_1)}$ respectively. Using these, Eq. 4.25 can be written as:

$$\Leftrightarrow \frac{z_l^{(1)}(k_a R_1)}{z_n^{(1)}(k_f R_2)} D_{nm}^{lM} + \overline{u}_n(R_2)\frac{z_l^{(1)}(k_a R_1)}{z_n^{(3)}(k_f R_2)} \sum_{\nu=(m,1)}^{N_{max}} \begin{bmatrix} \left(\frac{z_l^{(1)}(k_b R_2)}{z_\nu^{(1)}(k_f R_1)} C_{\nu m}^{lM}\right) \frac{z_\nu^{(1)}(k_f R_1)}{z_l^{(1)}(k_b R_2)} A_{\nu m,nm}(+k_f D)+ \\ \frac{z_l^{(1)}(k_b R_2)}{\zeta_\nu^{(1)}(k_f R_1)} C_{\nu m}^{lN} \frac{\zeta_\nu^{(1)}(k_f R_1)}{z_l^{(1)}(k_b R_2)} B_{\nu m,nm}(+k_f D) \end{bmatrix} = 0 \tag{4.26}$$

$$\Leftrightarrow \frac{z_l^{(1)}(k_a\,R_1)}{z_n^{(1)}(k_f R_2)}\,D_{nm}^{lM} + \overline{u}_n(R_2)\sum_{\nu=(m,1)}^{N_{max}}\left[\begin{array}{l}\frac{z_l^{(1)}(k_a\,R_1)}{z_n^{(3)}(k_f R_2)}\left(\frac{z_l^{(1)}(k_b\,R_2)}{z_\nu^{(1)}(k_f R_1)}C_{\nu m}^{lM}\right)\frac{z_\nu^{(1)}(k_f R_1)}{z_l^{(1)}(k_b\,R_2)}A_{\nu m,nm}(+k_f D)+\\ \frac{z_n^{(1)}(k_a\,R_1)}{z_l^{(3)}(k_f R_2)}\frac{z_l^{(1)}(k_b\,R_2)}{\zeta_\nu^{(1)}(k_f R_1)}C_{\nu m}^{lN}\frac{\zeta_\nu^{(1)}(k_f R_1)}{z_l^{(1)}(k_b\,R_2)}B_{\nu m,nm}(+k_f D)\end{array}\right] = 0 \tag{4.27}$$

$$\begin{aligned}\Leftrightarrow \frac{z_l^{(1)}(k_a\,R_1)}{z_n^{(1)}(k_f R_2)}\,D_{nm}^{lM} + \overline{u}_n(R_2)\frac{z_l^{(1)}(k_a\,R_1)}{z_l^{(1)}(k_b\,R_2)}\times\\ \sum_{\nu=(m,1)}^{N_{max}}\left[\begin{array}{l}\left(\frac{z_l^{(1)}(k_b\,R_2)}{z_\nu^{(1)}(k_f R_1)}C_{\nu m}^{lM}\right)\left(\frac{z_\nu^{(1)}(k_f R_1)}{z_n^{(3)}(k_f R_2)}A_{\nu m,nm}(+k_f D)\right)+\\ \left(\frac{z_l^{(1)}(k_b\,R_2)}{\zeta_\nu^{(1)}(k_f R_1)}C_{\nu m}^{lN}\right)\left(\frac{\zeta_\nu^{(1)}(k_f R_1)}{z_n^{(3)}(k_f R_2)}B_{\nu m,nm}(+k_f D)\right)\end{array}\right] = 0\end{aligned} \tag{4.28}$$

From Eq. 4.28 it is apparent that the appropriate normalizing factors for $A_{\nu m,nm}$ are $\left(z_\nu^{(1)}(k_f R_1)/z_n^{(3)}(k_f R_2)\right)$. Using similar steps the other coupled linear equations (Eq. 4.22a, 4.22b, 4.22c and 4.22d) can be modified to:

$$\begin{aligned}\left(\frac{z_l^{(1)}(k_b\,R_2)}{z_n^{(1)}(k_f R_1)}C_{nm}^{lM}\right) + \overline{u}_n(a)\frac{z_l^{(1)}(k_b\,R_2)}{z_l^{(1)}(k_a\,R_1)}\times\\ \sum_{\nu=(m,1)}^{N_{max}}\left[\begin{array}{l}\left(\frac{z_l^{(1)}(k_a\,R_1)}{z_\nu^{(1)}(k_f R_2)}D_{\nu m}^{lM}\right)\left(\frac{z_\nu^{(1)}(k_f R_2)}{z_n^{(3)}(k_f R_1)}A_{\nu m,nm}(-k_f D)\right)+\\ \left(\frac{z_l^{(1)}(k_a\,R_1)}{\zeta_\nu^{(1)}(k_f R_2)}D_{\nu m}^{lN}\right)\left(\frac{\zeta_\nu^{(1)}(k_f R_2)}{z_n^{(3)}(k_f R_1)}B_{\nu m,nm}(-k_f D)\right)\end{array}\right] = \frac{z_l^{(1)}(k_b\,R_2)}{z_n^{(1)}(k_f R_1)}p_N^M\delta_{Nl}\end{aligned} \tag{4.29a}$$

$$\begin{aligned}\left(\frac{z_l^{(1)}(k_a\,R_1)}{z_n^{(1)}(k_f R_2)}\,D_{nm}^{lM}\right) + \overline{u}_n(R_2)\frac{z_l^{(1)}(k_a\,R_1)}{z_l^{(1)}(k_b\,R_2)}\times\\ \sum_{\nu=(m,1)}^{N_{max}}\left[\begin{array}{l}\left(\frac{z_l^{(1)}(k_b\,R_2)}{z_\nu^{(1)}(k_f R_1)}C_{\nu m}^{lM}\right)\left(\frac{z_\nu^{(1)}(k_f R_1)}{z_n^{(3)}(k_f R_2)}A_{\nu m,nm}(+k_f D)\right)+\\ \left(\frac{z_l^{(1)}(k_b\,R_2)}{\zeta_\nu^{(1)}(k_f R_1)}C_{\nu m}^{lN}\right)\left(\frac{\zeta_\nu^{(1)}(k_f R_1)}{z_n^{(3)}(k_f R_2)}B_{\nu m,nm}(+k_f D)\right)\end{array}\right] = 0\end{aligned} \tag{4.29b}$$

$$\left(\frac{z_l^{(1)}(k_b R_2)}{\zeta_n^{(1)}(k_f R_1)} C_{nm}^{lN}\right) + \overline{v}_n(R_1) \frac{z_n^{(1)}(k_f R_1)}{\zeta_n^{(1)}(k_f R_1)} \frac{z_l^{(1)}(k_b R_2)}{z_l^{(1)}(k_a R_1)} \times \sum_{\nu=(m,1)}^{N_{max}} \left[\begin{array}{l} \left(\frac{z_l^{(1)}(k_a R_1)}{z_\nu^{(1)}(k_f R_2)} D_{\nu m}^{lM}\right) \left(\frac{z_\nu^{(1)}(k_f R_2)}{z_n^{(3)}(k_f R_1)} B_{\nu m,nm}(-k_f D)\right) \\ + \left(\frac{z_l^{(1)}(k_a R_1)}{\zeta_\nu^{(1)}(k_f R_2)} D_{\nu m}^{lN}\right) \left(\frac{\zeta_\nu^{(1)}(k_f R_2)}{z_n^{(3)}(k_f R_1)} A_{\nu m,nm}(-k_f D)\right) \end{array} \right] = 0 \tag{4.29c}$$

$$\left(\frac{z_l^{(1)}(k_a R_1)}{\zeta_n^{(1)}(k_f R_2)} D_{nm}^{lN}\right) + \overline{v}_n(R_2) \frac{z_n^{(1)}(k_f R_2)}{\zeta_n^{(1)}(k_f R_2)} \frac{z_l^{(1)}(k_a R_1)}{z_l^{(1)}(k_b R_2)} \times \sum_{\nu=(m,1)}^{N_{max}} \left[\begin{array}{l} \left(\frac{z_l^{(1)}(k_b R_2)}{z_\nu^{(1)}(k_f R_1)} C_{\nu m}^{lM}\right) \left(\frac{z_\nu^{(1)}(k_f R_1)}{z_n^{(3)}(k_f R_2)} B_{\nu m,nm}(+k_f D)\right) \\ + \left(\frac{z_l^{(1)}(k_b R_2)}{\zeta_\nu^{(1)}(k_f R_1)} C_{\nu m}^{lN}\right) \left(\frac{\zeta_\nu^{(1)}(k_f R_1)}{z_n^{(3)}(k_f R_2)} A_{\nu m,nm}(+k_f D)\right) \end{array} \right] = 0 \tag{4.29d}$$

Since $A_{\nu m,nm}$ and $B_{\nu m,nm}$ are related to $\beta_{\nu m,nm}$ as given in Eq. 4.17 and 4.18 it is sufficient if we build recursion relations for the normalized scalar translation coefficient $\beta_{\nu m,nm}^N$ given by

$$\beta_{\nu m,nm}^N = \frac{z_\nu^{(1)}(k_f R_1)}{z_n^{(3)}(k_f R_2)} \beta_{\nu m,nm} \tag{4.30}$$

The recursion relations for the normalized translation coefficients $\beta_{\nu m,nm}^N$ can be developed as:

$$\frac{z_\nu^{(1)}(k_f R_1)}{z_{n+1}^{(3)}(k_f R_2)} \beta_{\nu m,n+1,m} = \frac{1}{a_{nm}^+} \left(-a_{nm}^- \frac{z_\nu^{(1)}(k_f R_1)}{z_{n+1}^{(3)}(k_f R_2)} (\beta_{\nu m,n-1,m}) + a_{\nu-1,m}^+ \frac{z_\nu^{(1)}(k_f R_1)}{z_{n+1}^{(3)}(k_f R_2)} (\beta_{\nu-1m,nm}) + a_{\nu+1,m}^- \frac{z_\nu^{(1)}(k_f R_1)}{z_{n+1}^{(3)}(k_f R_2)} (\beta_{\nu+1m,nm}) \right) \tag{4.31}$$

$$\begin{aligned} \Leftrightarrow \beta_{\nu m,n+1,m}^N = & \frac{1}{a_{nm}^+} \left(-a_{nm}^- \frac{\cancel{z_\nu^{(1)}(k_f R_1)}}{z_{n+1}^{(3)}(k_f R_2)} \frac{z_{n-1}^{(3)}(k_f R_2)}{\cancel{z_{n-1}^{(3)}(k_f R_2)}} (\beta_{\nu m,n-1,m}^N) \right. \\ & + a_{\nu-1,m}^+ \frac{z_\nu^{(1)}(k_f R_1)}{z_{n+1}^{(3)}(k_f R_2)} \frac{\cancel{z_{\nu-1}^{(1)}(k_f R_1)}}{z_{\nu-1}^{(1)}(k_f R_1)} \frac{z_n^{(3)}(k_f R_2)}{\cancel{z_n^{(3)}(k_f R_2)}} (\beta_{\nu-1m,nm}^N) \\ & \left. + \frac{z_\nu^{(1)}(k_f R_1)}{z_{n+1}^{(3)}(k_f R_2)} \frac{\cancel{z_{\nu+1}^{(1)}(k_f R_1)}}{z_{\nu+1}^{(1)}(k_f R_1)} \frac{z_n^{(3)}(k_f R_2)}{\cancel{z_n^{(3)}(k_f R_2)}} a_{\nu+1,m}^- (\beta_{\nu+1m,nm}^N) \right) \end{aligned} \tag{4.32}$$

$$\Leftrightarrow \beta^N_{\nu m,n+1,m} = \frac{1}{a^+_{nm}} \left(-a^-_{nm} \frac{z^{(3)}_{n-1}(k_f R_2)}{z^{(3)}_{n+1}(k_f R_2)} \beta^N_{\nu m,n-1,m} + a^+_{\nu-1,m} \frac{z^{(1)}_{\nu}(k_f R_1)}{z^{(1)}_{\nu-1}(k_f R_1)} \frac{z^{(3)}_{n}(k_f R_2)}{z^{(3)}_{n+1}(k_f R_2)} \beta^N_{\nu-1 m,nm} + \frac{z^{(1)}_{\nu}(k_f R_1)}{z^{(1)}_{\nu+1}(k_f R_1)} \frac{z^{(3)}_{n}(k_f R_2)}{z^{(3)}_{n+1}(k_f R_2)} a^-_{\nu+1,m} \beta^N_{\nu+1 m,nm} \right) \tag{4.33}$$

An important property to be noticed is the fact that a^-_{mm} is zero so that to start off you will only need (0,0) harmonic to find the coefficients for the (1,0) harmonic. As can be noticed, the recursion relations depend on ratios of successive orders of Bessel and Hankel functions. This aids computation of these translation coefficients tremendously since you do not have to compute individual Bessel and Hankel functions of a particular order and hence we do not encounter divergent numbers at any point during the recursion.

To traverse from one 'm' to the next, the following recursion relations for the translation coefficients needs to be used (Eq. 27 in Ref. [76]:

$$\beta_{\nu\, m+1,n+1\, m+1} = \frac{-b^-_{nm}(\beta_{\nu\, m+1,n-1\, m+1}) + b^+_{\nu-1,m}(\beta_{\nu-1\, m,nm}) + b^-_{\nu+1,m}(\beta_{\nu+1\, m,nm})}{b^+_{nm}} \tag{4.34}$$

We only need the values for $n = m$ since we can initialize the values for higher values of n using Eq. 4.15. Also note that when $n = m$, $b_{nn} = 0$. Hence Eq. 4.34 reduces to Eq. 4.16. The normalization process for Eq. 4.16 is given below:

$$\frac{z^{(1)}_{\nu}(k_f R_1)}{z^{(3)}_{n+1}(k_f R_2)} \beta_{\nu\, n+1,n+1\, n+1} = \frac{1}{b^+_{nn}} \left(b^+_{\nu-1,n} \frac{z^{(1)}_{\nu}(k_f R_1)}{z^{(3)}_{n+1}(k_f R_2)} \frac{\cancel{z^{(1)}_{\nu-1}(k_f R_1)}}{z^{(1)}_{\nu-1}(k_f R_1)} \frac{z^{(3)}_{n}(k_f R_2)}{\cancel{z^{(3)}_{n}(k_f R_2)}} (\beta_{\nu-1\, n,nn}) + b^-_{\nu+1,n} \frac{z^{(1)}_{\nu}(k_f R_1)}{z^{(3)}_{n+1}(k_f R_2)} \frac{\cancel{z^{(1)}_{\nu+1}(k_f R_1)}}{z^{(1)}_{\nu+1}(k_f R_1)} \frac{z^{(3)}_{n}(k_f R_2)}{\cancel{z^{(3)}_{n}(k_f R_2)}} (\beta_{\nu+1\, n,nn}) \right) \tag{4.35}$$

i.e.

$$\beta^N_{\nu\, n+1,n+1\, n+1} = \frac{1}{b^+_{nn}} \left(b^+_{\nu-1,n} \frac{z^{(3)}_{n}(k_f R_2)}{z^{(3)}_{n+1}(k_f R_2)} \frac{z^{(1)}_{\nu}(k_f R_1)}{z^{(1)}_{\nu-1}(k_f R_1)} \beta_{\nu-1\, n,nn} + b^-_{\nu+1,n} \frac{z^{(3)}_{n}(k_f R_2)}{z^{(3)}_{n+1}(k_f R_2)} \frac{z^{(1)}_{\nu}(k_f R_1)}{z^{(1)}_{\nu+1}(k_f R_1)} \beta_{\nu+1\, n,nn} \right) \tag{4.36}$$

These recursion relations are only dependent on ratio of successive orders of spherical Bessel functions and hence we do not encounter very small numbers when $\nu \gg k_f D$. The ratios have been computed by method of continued fractions as shown in Section 4.5. The initialization for the recursion is provided by:

$$\boxed{\beta^N_{\nu 0,00} = (-1)^\nu \sqrt{2\nu+1} \frac{z^{(1)}_\nu(k_f R_1)}{z^{(3)}_0(k_f R_2)} z^{(3)}_\nu(k_f D)} \tag{4.37}$$

The spherical Hankel functions in Eq. 4.37, if computed individually, will lead to diverging numbers when $\nu \gg k_f D$ as explained previously. To circumvent this, the factor $\frac{z^{(1)}_0(k_f R_1)}{z^{(3)}_\nu(k_f R_2)} z^{(3)}_\nu(k_f D)$ is determined by computing the exponential of $\log\left[z^{(1)}_0(k_f R_1)\right] - \log\left[z^{(3)}_\nu(k_f R_2)\right] + \log\left[z^{(3)}_\nu(k_f D)\right]$. The procedure to compute logarithm of Bessel functions and Hankel functions is detailed in Section 4.5.

The steps for initializing the $(n,\nu)^{th}$ element of the translation coefficient $\beta_{\nu m,nm}$ are:

- $m = 0$

  Find (0,0), (0,1), (0,2), (0,3)... successively using Eq. 4.37. Use these values and employ Eq. 4.33 to find (1,1), (1,1), (1,2), (1,3) and similarly for other rows of n

- $m = 1$

  Use (0,0), (0,1), (0,2) ... from $m = 0$ to find (1,1) , (1,2), (1,3)... for $m = 1$ employing Eq. 4.36 and then use Eq. 4.33 to find the coefficients of (2,1), (2,2), (2,3)...and other rows in n successively.

- $m = 2$

  Use (1,1), (1,2) ... from $m = 1$ to find (2,2), (2,3)... for $m = 2$ employing Eq. 4.36 and then use Eq. 4.33 to find the coefficients of (3,2), (3,3), (3,4)... and other rows in n successively

  and similarly for other values of m

4.5 Computing logarithm and ratios of Bessel functions

The method of continued fraction to compute ratios of successive orders of Bessel and Hankel functions has been adopted from Ref. [77] and the method to compute logarithm of Bessel and Hankel functions has been adopted from Ref. [78]. While the steps below detail that for cylindrical Bessel and Hankel functions, it can be extended to spherical Bessel functions by noting that:

$$z_n^{(1)}(x) = \sqrt{\frac{\pi}{2x}} J_{n+1/2}(x) \tag{4.38}$$

The logarithm of Bessels function is of the form:

$$\log\left[J_n(z)\right] = \log\left[J_0(z)\right] - \sum_{k=1}^{n} \log\left(R_k\right) \tag{4.39}$$

where

$$R_k = \frac{J_{k-1}(z)}{J_k(z)} \tag{4.40}$$

Note that to find $\log\left[J_{(n)}\right]$ we must know what R_k is. This is got from using continued fraction expansion.

$$R_k = a_1(z,k) + \cfrac{1}{a_2(z,k) + \cfrac{1}{a_3(z,k) + \cfrac{1}{a_4(z,k) + ...}}} \tag{4.41}$$

with $a_m(z,k) = \dfrac{2\left(-1\right)^{(m+1)}\left(k+m-1\right)}{z}$ We also need the value of $\log\left[J_0(z)\right]$ which is computed using the form:

$$\log\left[J_0(z)\right] = \log\left[\cos(z)\right] - \log\left(1 + 2\sum_{k=0}^{\infty}\left(-1\right)^k \frac{J_{2k}(z)}{J_0(z)}\right) \tag{4.42}$$

The ratio $\dfrac{J_{2k}(z)}{J_0(z)}$ is got from the following consideration: If N is the largest order of the bessel function required, then R_N can be computed using the continued fraction method

shown earlier. Using this $\frac{J_{2k}}{J_0}$ can be found out (for small k of course, or else there will be a overflow again) from:

$$\frac{J_n(z)}{J_0(z)} = R_n \cdot R_{n-1} \cdot R_{n-2} \cdot ...R_1 \tag{4.43}$$

4.6 Conclusion

In this chapter a brief introduction to the translation addition theorem was provided. The method of computation of the translation coefficients present in literature was listed and difficulties of computing the translation coefficients in the present form for near-field scattering problems was explained. A method of normalizing the translation coefficients was shown and recursion relations were derived for the normalized translation coefficients. The ability to express these recursion relations of the normalized translation coefficients in terms of ratios of successive order of spherical Bessel and Hankel functions was mentioned as the primary reason for overcoming the computational difficulties in the original form. Apart from overcoming diverging numbers normalizing translation coefficients has another important consequence which is explained in Chapter 6

Chapter 5

One term approximation

5.1 Motivation

In most cases arrays of the translation coefficients $A_{\nu m,nm}$ and $B_{\nu m,nm}$ are needed for $n = 1, ..., n_{max}$ and $\nu = 1, ..., \nu_{max}$ at fixed values of m. It is mentioned in Ref. [73] that when $n_{max} = \nu_{max} = 10$, the speed when using the recurrence relations listed in Chapter 4 (Eq. 4.15 and Eq. 4.16) is about 400 times faster than using the form which includes computing the Weigner 3j coefficients (Eq. 4.14 in Chapter 4). However, when computing the near-field radiative transfer between two spheres separated by a small gap, n_{max} and ν_{max} can easily reach values up to 1000 and even these recurrence relations become computationally expensive. In this chapter it is shown that in such a case when the number of spherical waves needed for convergence $n_{max}, \nu_{max} \gg k_f D$, the recurrence relations can be simplified further to make it more computationally viable. Recursion relations have also been derived for these simplified form of translation coefficients.

5.2 Analysis

Consider the form for the scalar translation coefficient, $\beta_{\nu m,nm}$ for two spheres separated by a gap D given in [51]. The exact form for the translation coefficient is given by:

$$\beta_{\nu m,nm}(k_f D) = \sum_p 4\pi i^{\nu+p-n} \psi_{p,0}(k_f D) A(m,n,-m,\nu,p) \tag{5.1}$$

where,

$$\psi_{p,0}(k_f D) = z_p^{(3)}(k_f D) Y_{p,0}(\theta'', \phi'') \tag{5.2}$$

For our configuration $\theta'' = 0$, $\phi'' = 0$ so that:

$$\psi_{p,0}(k_f D) = z_p^{(3)}(k_f D) Y_{p,0}(0,0) \tag{5.3}$$

The spherical harmonic $Y_{p,0}(\theta'', \phi'')$ is given by:

$$Y_{p,0}(0,0) = \sqrt{\frac{2p+1}{4\pi}}\, P_p^0(1) \tag{5.4}$$

where, $P_p^0(1)$ represents the Associated Legendre polynomials. The function $P_p^n(1)$ has the property that

$$P_p^n(1) = \begin{cases} 1 & \text{when } n = 0 \\ 0 & \text{when } n \neq 0 \end{cases} \tag{5.5}$$

Therefore we have,

$$\psi_{p,0}(k_f D) = z_p^{(3)}(k_f D) \sqrt{\frac{2p+1}{4\pi}} \tag{5.6}$$

Hence, the form for $\beta_{\nu m,nm}(k_f D)$ from Eq. 5.1 for our configuration of two spheres translated along z-axis reduces to Eq. 4.14 (repeated here for the convenience of the reader):

$$\beta_{\nu m,nm}(k_f D) = \sum_p 4\pi i^{\nu+p-n} z_p^{(3)}(k_f D) \sqrt{\frac{2p+1}{4\pi}} A(m,n,-m,\nu,p) \qquad \text{(4.14 revisited)}$$

We note that the form for $\beta_{\nu m,nm}$ depends on a summation over different orders p of the spherical Hankel function $z_p^{(3)}(k_f D)$. The magnitude of $z_p^{(3)}(k_f D)$ increases exponentially for $p > k_f D$, as seen in Fig. 5.1. From this behavior, we observe that for $p \gg k_f D$ the

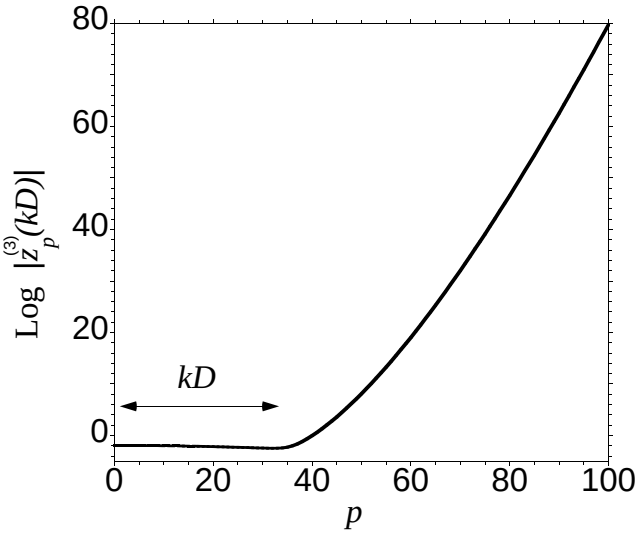

Figure 5.1: Plot of $\log|z_p^{(3)}(k_fD)|$ as a function of the order p. Here k_fD is arbitrarily chosen to be of value 33

contribution from the last term in the summation over p in Eq. 4.14 i.e the term with $p = n + \nu$ dominates over the rest of the contributions and hence only this term can be retained in the summation over p. Using this in Eq. 4.14, we get the one-term approximation form for the scalar translation coefficient $\beta_{\nu m,nm}$ as:

$$\beta_{\nu m,nm} = 4\pi i^{2\nu}\, z_{n+\nu}^{(3)}(k_fD)\sqrt{\frac{2(n+\nu)+1}{4\pi}}A(m,n,-m,\nu,(n+\nu)) \tag{5.7}$$

In order to decide the cutoff criterion for employing this simplification, it is sufficient if we analyze the exponential behavior of $z_p^{(3)}(k_fD)$ as a function of its order p since the rest of the terms in Eq. 4.14 do not vary significantly. What we are primarily interested in is the ratio $(z_{p+2}^{(3)}/z_p^{(3)})$ since p increments by a step of two due to the special property of $A(m,n,-m,\nu,n+\nu)$ [51]. The asymptotic form for the ratio $z_{p+2}^{(3)}(k_fD)/z_p^{(3)}(k_fD)$ for $p \gg 1$ is equivalent to the asymptotic form for the ratio $y_{p+2}(k_fD)/y_p(k_fD)$ where $y_p(k_fD)$ represents the spherical Neumann functions. From Ref. [74], the asymptotic form for cylindrical Neumann functions $Y_\nu(z)$ can be written as:

$$Y_\nu(z) = \sqrt{\frac{2}{\pi\nu}} \left(\frac{ez}{2\nu}\right)^{-\nu} \tag{5.8}$$

Since we require spherical Neumann functions $y_\nu(z)$ which are related to $Y_\nu(z)$ by:

$$y_\nu(z) = \sqrt{\frac{\pi}{2z}} Y_{\nu+\frac{1}{2}}(z) \tag{5.9}$$

we get:

$$\begin{aligned} Y_{\nu+\frac{1}{2}}(z) &= \sqrt{\frac{2}{\pi(\nu+\frac{1}{2})}} \left(\frac{ez}{2(\nu+\frac{1}{2})}\right)^{-(\nu+\frac{1}{2})} &(5.10)\\ &= \sqrt{\frac{4}{\pi(2\nu+1)}} \left(\frac{ez}{(2\nu+1)}\right)^{-(\nu+\frac{1}{2})} &(5.11)\end{aligned}$$

Hence we have:

$$\begin{aligned} \frac{y_{\nu+2}(k_f D)}{y_\nu(k_f D)} &= \sqrt{\frac{(2\nu+1)}{(2\nu+5)}} \left(\frac{1}{ek_f D}\right)^2 \left(\frac{(2\nu+5)^{\nu+\frac{5}{2}}}{(2\nu+1)^{\nu+\frac{1}{2}}}\right) &(5.12)\\ &= \left(\frac{2\nu+5}{ek_f D}\right)^2 \left(\frac{2\nu+5}{2\nu+1}\right)^\nu &(5.13)\end{aligned}$$

Therefore we get:

$$\frac{z^{(3)}_{p+2}(k_f D)}{z^{(3)}_p(k_f D)} = \left(\frac{2p+5}{ek_f D}\right)^2 \left(\frac{2p+5}{2p+1}\right)^p \tag{5.14}$$

Using Eq. 5.14 it is possible to get an estimate of the error resulting from not retaining the rest of the terms in the summation over p in Eq. 4.14 while using the one-term approximation. To see this we simplify Eq. 5.14 with the following steps:

$$\begin{aligned} \frac{z^{(3)}_p(k_f D)}{z^{(3)}_{p-2}(k_f D)} &= \left(\frac{2p-3}{ek_f D}\right)^2 \left(\frac{2p+1}{2p-3}\right)^p &(5.15)\\ &= \left(\frac{2p-3}{ek_f D}\right)^2 \left(\frac{2p-3+4}{2p-3}\right)^p &(5.16)\\ &= \left(\frac{2p-3}{ek_f D}\right)^2 \left(1+\frac{2}{p-\frac{3}{2}}\right)^p &(5.17)\end{aligned}$$

For large p, this $\left(1+\frac{2}{p-\frac{3}{2}}\right)^p$ reduces to e^2 so that we can write:

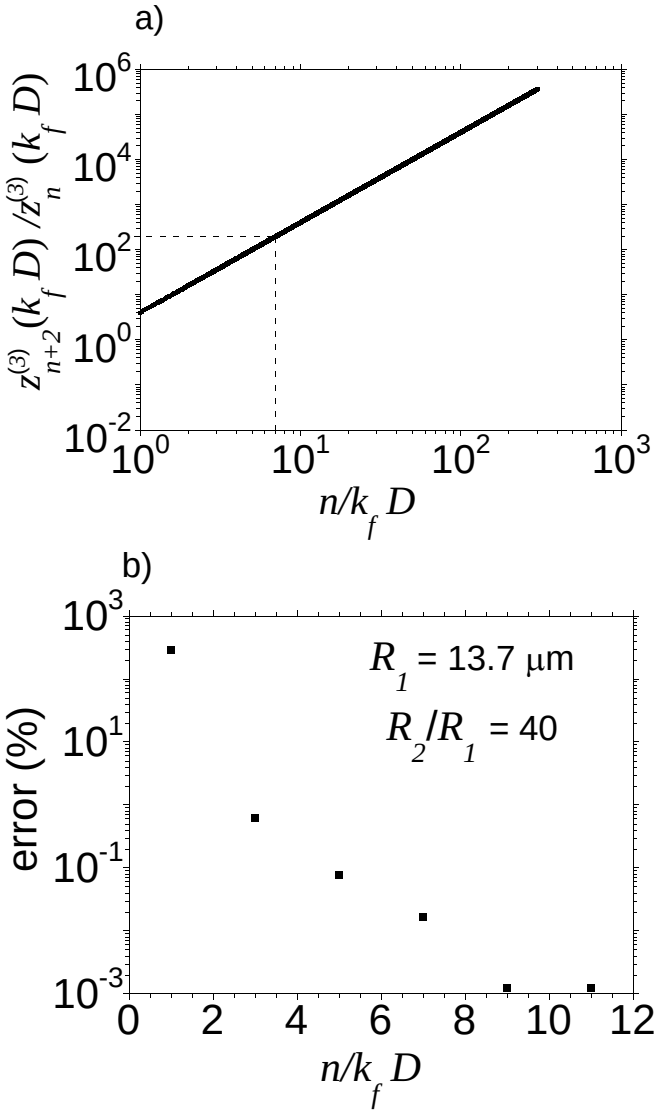

Figure 5.2: a) Plot of $(z^{(3)}_{n+2}(k_f D)/z^{(3)}_n(k_f D))$ as a function of n for a $k_f D$ value of 33 (arbitrarily chosen). The point $n = 7\,k_f D$ beyond which the one-term approximation has been adopted in our computations for calculating the translation coefficients has been indicated in the figure b) The error in spectral conductance at the resonant frequency of 0.061 eV when different factors of the argument $k_f D$ is chosen as the criterion for employing the one-term approximation. From the plot, a criterion $n = 7k_f D$ is observed to give an error of $\approx 0.02\%$ in the spectral conductance. The spectral conductance has been computed for two spheres of size $R_1 = 13.7\,\mu$m and $R_2 = 40R_1$ with minimum gap $d/R_1 = 0.01$

$$\frac{z_p^{(3)}(k_f D)}{z_{p-2}^{(3)}(k_f D)} = \left(\frac{2p-3}{e k_f D}\right)^2 e^2 \tag{5.18}$$

$$\Rightarrow \frac{z_{p-2}^{(3)}(k_f D)}{z_p^{(3)}(k_f D)} = \left(\frac{k_f D}{2p-3}\right)^2 \tag{5.19}$$

To get an expression for the error [= (exact − estimated)/exact = 0.01 (for 1% error)] we make a reasonable approximation that for large p the contribution from $p = n + \nu - 2$ is representative of the error from retaining only the last term $p = n + \nu$ in the summation in Eq. 4.14. Hence the expression for the error can be written as:

$$\text{error} = \frac{\left[z_{p-2}^{(3)}(k_f D) + z_p^{(3)}(k_f D)\right] - z_p^{(3)}(k_f D)}{\left[z_{p-2}^{(3)}(k_f D) + z_p^{(3)}(k_f D)\right]} \tag{5.20}$$

$$\Rightarrow \text{error} = \frac{\left(\frac{z_{p-2}^{(3)}(k_f D)}{z_p^{(3)}(k_f D)}\right)}{\left(\frac{z_{p-2}^{(3)}(k_f D)}{z_p^{(3)}(k_f D)}\right) + 1} \tag{5.21}$$

Substituting from Eq. 5.19 we get:

$$\text{error} = \frac{\left(\frac{k_f D}{2p-3}\right)^2}{\left(\frac{k_f D}{2p-3}\right)^2 + 1} \tag{5.22}$$

Since $p = n + \nu$ in the one-term approximation, the expression for the error in Eq. 5.22 turns out to be:

$$\text{error} \approx \frac{\left(\frac{k_f D}{2(n+\nu)-3}\right)^2}{\left(\frac{k_f D}{2(n+\nu)-3}\right)^2 + 1} \tag{5.23}$$

For 1% error we get $n + \nu \approx 5\, k_f D$. For our computations we have used $n + \nu = 7\, k_f D$ as the criterion for employing the one-term approximation. The ratio from Eq. 5.14 has been plotted in Fig. 5.2(a). It is observed that when $p = 7\, k_f D$, $z_p^{(3)}(k_f D) \approx 100\, z_{p-2}^{(3)}(k_f D)$. A

plot of error (in %) in the spectral conductance at a resonant frequency (0.061 eV) when the one-term approximation is used at different values of the order p is shown in Fig. 5.2(b). The errors are computed with respect to the spectral conductance value when the approximated form for translation coefficients is not employed. It can be observed that adopting $p = 7k_fD$ as the criterion for employing the one-term approximation gives us an error of about 0.05% in the spectral conductance.

The expression for the scalar translation coefficient $\beta_{\nu m,nm}$ given in Eq. 5.7 cannot be used as is for computational purposes since the computation of Weigner 3j coefficient is tedious. Hence recursion relations can be derived for the approximated form for $\beta_{\nu m,nm}$. Employing

$$\begin{pmatrix} n & \nu & n+\nu \\ -m & m & 0 \end{pmatrix} = (-1)^{n-\nu}\sqrt{\frac{(2n)!(2\nu)!(n+\nu)!(n+\nu)!}{(2n+2\nu+1)!(n-m)!(n+m)!(\nu-m)!(\nu+m)!}} \tag{5.24}$$

in Eq. 5.7 it can be shown that the recursion relations turn out to be of the form:

$$\begin{aligned}\beta_{\nu m,n+1\,m} = \beta_{\nu m,nm}\left(\frac{n+1}{n}\right)\sqrt{\frac{(2n+3)(2n+1)}{(n+1)^2-m^2}}\times \\ \left(\frac{n+\nu+1}{2n+2\nu+1}\right)\left(\frac{z^{(3)}_{n+\nu+1}(k_fD)}{z^{(3)}_{n+\nu}(k_fD)}\right)\end{aligned} \tag{5.25}$$

This form of recursion is computationally simpler than the corresponding recursion relations for the exact form of $\beta_{\nu m,nm}$ given in Eq. 4.15. Once the scalar translation coefficient $\beta_{\nu m,nm}$ has been computed, the vector translation coefficients $A_{\nu m,nm}$ and $B_{\nu m,nm}$ can be obtained from Eq. 4.17 and Eq. 4.18.

5.3 Conclusions

In this chapter, a simplified form of translation addition theorem (referred to in this chapter as the 'one-term approximation') valid for general near-field electromagnetic scattering problems has been proposed and the limit at which this form is valid is discussed. The accuracy of this approximation has also been detailed from an error analysis. This simplified

form is about 10 times faster than the corresponding exact form for computing the vector translation coefficients

Chapter 6

Dependence of normalized translation coefficients on the radius ratio of the spheres

6.1 Introduction

For near-field scattering problems when the closest gap between the two spheres $d \ll R_1, R_2$ (here, $d = D - R_1 - R_2$) the elements in the matrix representing the normalized translation coefficient $\beta^N_{nm,\nu m}$ shows a marked dependence on the radius ratio R_2/R_1. In this chapter a description of this behavior is provided by expressing the elements of $\beta^N_{nm,\nu m}$ in a matrix form for different values of (n, ν) (for a particular m) and plotting this matrix for different radius ratios of the spheres. An attempt is made to explain this characteristic behavior analytically and its utilization in simplifying the computational procedure to calculate the near-field radiative transfer between spherical bodies.

6.2 Description via matrix plots

As described in Chapter 4 a form of the normalized scalar translation coefficient can be written as:

$$\beta^N_{\nu m,nm} = \beta_{\nu m,nm} \frac{z^{(1)}_\nu(k_f R_1)}{z^{(3)}_n(k_f R_2)} \tag{6.1}$$

This is equivalent to computing an expression of the form:

$$\beta_{\nu m,nm} \frac{z^{(1)}_n(k_f R_1)}{z^{(3)}_\nu(k_f R_2)} \tag{6.2}$$

and then taking the transpose of Expr. 6.2 keeping in mind the symmetry relations for $\beta_{\nu m,nm}$ [79]. The advantage of using Expr. 6.2 becomes apparent when we analyze the behavior of this expression for $(n, \nu) > k_f D$. From the one-term approximation that has been detailed in Chapter 5 for $n, \nu \gg k_f D$, we can write

$$\beta_{\nu m,nm} \sim z^{(3)}_{n+\nu}(k_f D) \tag{6.3}$$

[since the spherical Hankel function is the dominant term for large (n, ν)]. Expr. 6.2 is thus similar to

$$\left(z^{(3)}_{n+\nu}(k_f D) \frac{z^{(1)}_n(k_f R_1)}{z^{(3)}_\nu(k_f R_2)} \right) \tag{6.4}$$

This expression has been analyzed as a function of n and ν for different radius ratios R_2/R_1. Figures 6.1(a), 6.1(b), 6.1(c) and 6.1(d) show the contour plots of the expression $\mathrm{Log}_{10}|z^{(3)}_{n+\nu}(k_f D)\, z^{(1)}_n(k_f R_1)/z^{(3)}_\nu(k_f R_2)|$ for two spheres with radius ratios $R_2/R_1 = 1, 3, 10, \text{and } 20$ respectively. The radius of the smaller sphere $R_1 = 10\,\mu$m and the gap between the spheres is taken to be 50 nm for all the cases. When $R_2/R_1 = 1$ it can be observed from Fig. 6.1(a) that the dominant terms in the matrix are present in a band along the diagonal with terms on either side of the band tapering off exponentially. This behavior can be utilized to simplify the computation of translation coefficients and also the linear-coupled equations that result from applying the boundary conditions, since, terms in the matrix with absolute values less than 10^{-6} can be approximated to be zero and sparse routines can then be employed to solve the linear equations. This approximation affords an

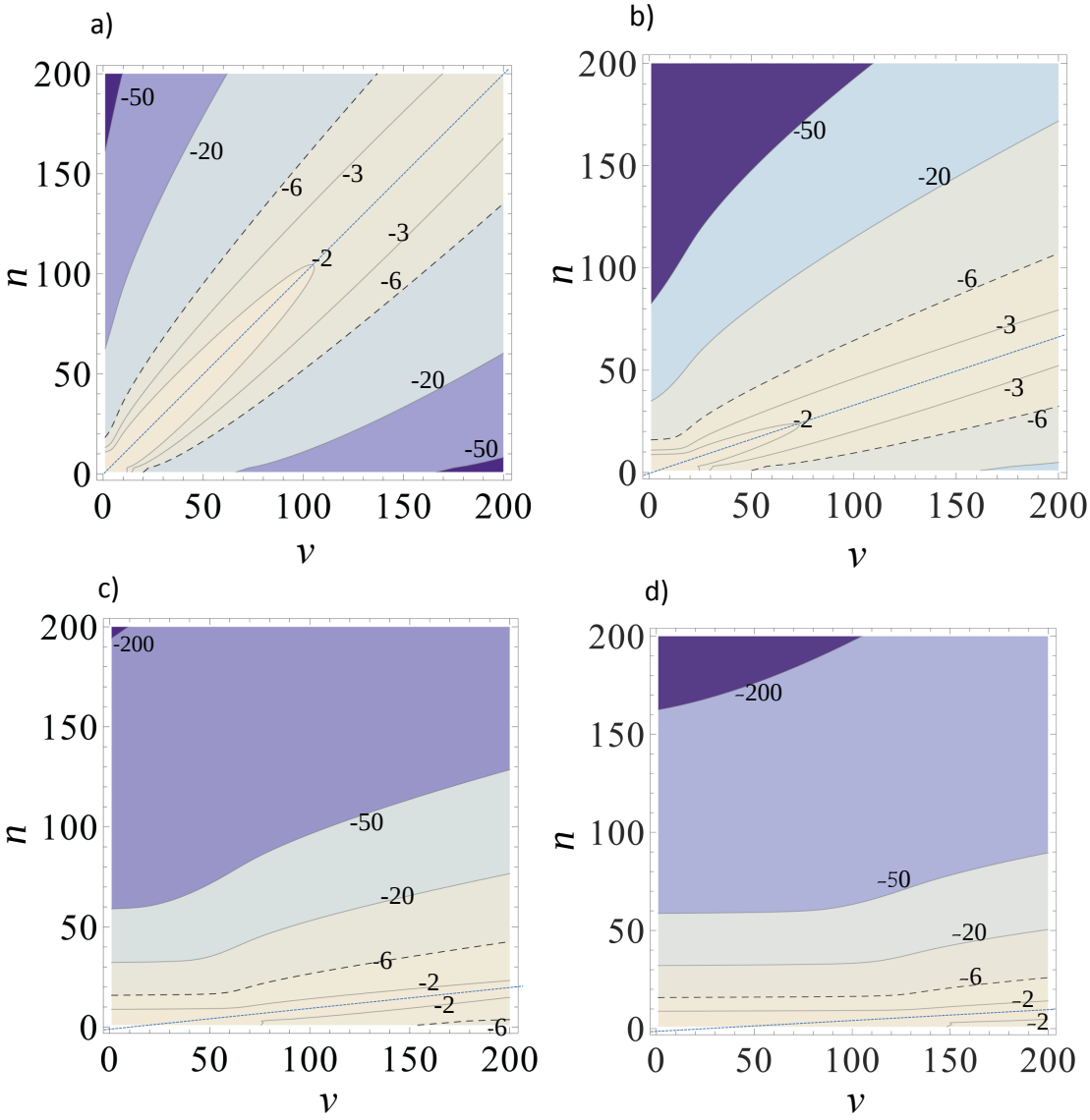

Figure 6.1: Contour plots of the expression $\mathrm{Log}_{10}|z_n^{(1)}(k_f R_1)\, z_{n+\nu}^{(3)}(k_f r'')/z_\nu^{(3)}(k_f R_2)|$ as a function of n and ν for two spheres with successive radius ratios R_2/R_1 = (a) 1, (b) 3, (c) 10, and (d) 20 with $R_1 = 10\,\mu$m, and the minimum gap maintained at 50 nm for all the cases. The dashed-lines denotes the contour line for a value of -6 which is taken as the cutoff point below which values for the normalized vector translation coefficients are approximated to zero. The line of maximum (shown as dotted lines) given by Eq. 6.35 has been superimposed on these contour plots

error of less than 0.05 % in the final computed value of the conductance. For $R_2/R_1 > 1$ the distribution of the dominant terms in the matrix changes markedly. From Fig. 6.1(c) and 6.1(d) where $R_2/R_1 \gg 1$ it can be observed that only the elements in the first few rows of the matrix needs to be initialized with the absolute values of the terms in the higher rows falling off exponentially. This simplifies the computation procedure since only these rows need to be stored and utilized thereof.

6.3 Asymptotic analysis

The characteristic dependence of $\beta^N_{nm,\nu m}$ on the radius ratio R_2/R_1 as shown in Section 6.2 can be explained analytically by using the asymptotic forms for the spherical Bessel and Hankel functions when $n, \nu \gg 1$. When $n \to \infty$ and $x \approx O(n)$ (from Ref. [74]) the asymptotic form for the cylindrical Bessel function as:

$$J_n(n \text{ sech } \alpha) = \frac{e^{n(\tanh\alpha - \alpha)}}{\sqrt{2\pi n \tanh\alpha}} \tag{6.5}$$

where, $0 < \text{sech } \alpha \leq 1$ Using ν sech $\alpha = x_1$ i.e sech $\alpha = x_1/\nu$, and $\tanh^2(x) = 1 - \text{sech}^2(x)$, Eq. 6.5 reduces to:

$$J_n(x_1) = \frac{e^{\sqrt{n^2 - x_1^2} - n \cosh^{-1}(n/x_1)}}{\sqrt{2\pi\sqrt{(n^2 - x_1^2)}}} \tag{6.6}$$

From this, and making use of the relation between cylindrical and spherical Bessel functions, we can write the asymptotic form for the spherical Bessel function $z_n^{(1)}(k_f R_1)$ for $n \gg k_f R_1$ as:

$$z_n^{(1)}(k_f R_1) \approx \frac{e^{\sqrt{(n+1/2)^2 - (k_f R_1)^2} - (n+1/2)\cosh^{-1}[(n+1/2)/(k_f R_1)]}}{2\sqrt{(k_f R_1)\sqrt{(n+1/2)^2 - (k_f R_1)^2}}} \tag{6.7}$$

For the asymptotic form of the spherical Hankel's function $z_\nu^{(3)}(x)$, we use the asymptotic function of the spherical Neumann functions $y_\nu^{(3)}(x)$, since for large ν $z_\nu^{(3)}(x) \approx i y_\nu^{(3)}(x)$. From Ref. [74]) the asymptotic form for the cylindrical Neumann function can be written as:

$$Y_\nu(\nu \text{ sech } \alpha) \approx -\frac{e^{\nu(\alpha - \tanh\alpha)}}{\sqrt{\frac{1}{2}\pi\nu \tanh\alpha}} \tag{6.8}$$

Taking ν sech $\alpha = x_2$ this reduces to:

$$Y_\nu(x_2) = \frac{e^{\nu \cosh^{-1}(\nu/x_2) - \sqrt{\nu^2 - x_2^2}}}{\sqrt{\frac{1}{2}\pi\sqrt{(\nu^2 - x_2^2)}}} \tag{6.9}$$

So we can write the asymptotic forms for $z_\nu^{(3)}(k_f\, R_2)$ and $z_{n+\nu}^{(3)}(k_f\, D)$ as:

$$z_\nu^{(3)}(k_f R_2) \approx \frac{e^{(\nu+1/2)\, \cosh^{-1}[(\nu+1/2)/k_f R_2] - \sqrt{(\nu+1/2)^2 - (k_f R_2)^2}}}{\sqrt{(k_f R_2)\sqrt{(\nu+1/2)^2 - (k_f R_2)^2}}} \tag{6.10}$$

and

$$z_{n+\nu}^{(3)}(k_f D) \approx \frac{e^{(n+\nu+1/2)\, \cosh^{-1}[(\nu+1/2)/k_f D] - \sqrt{(\nu+1/2)^2 - (k_f D)^2}}}{\sqrt{(k_f D)\sqrt{(\nu+1/2)^2 - (k_f D)^2}}} \tag{6.11}$$

The ratio we are interested in is given by Expr. 6.4.

6.3.1 Analysis for equal sized spheres

For the case of equal sized spheres we have $x_1 = x_2 = x(= k_f R_1)$ and $x_3 = kD = 2x + \delta$ where δ denotes the kd term. For small gaps, we have $\delta = kd \to 0$. Expr. 6.4 can thus be reduced to:

$$z_n^{(1)}(x)\frac{z_{n+\nu}^{(3)}(2x+\delta)}{z_\nu^{(3)}(x)} \tag{6.12}$$

To get an order of magnitude estimate we will be considering only the dominant exponential terms in the asymptotic forms for the terms in Expr. 6.12. For simplified representation we replace $(n+1/2)$ by n (and similarly for $(\nu+1/2)$ and $(n+\nu+1/2)$). The arguments below for n and ν can be shown to hold true without this simplification. Expr. 6.12 will then be of the order:

$$\begin{gathered} e^{\left[\sqrt{n^2-x^2}+\sqrt{\nu^2-x^2}-\sqrt{(n+\nu)^2-(2x+\delta)^2}\right]} \times \\ e^{\left[(n+\nu)\, \cosh^{-1}\left(\frac{n+\nu}{2x+\delta}\right) - n\, \cosh^{-1}\left(\frac{n}{x}\right) - \nu\, \cosh^{-1}\left(\frac{\nu}{x}\right)\right]} \end{gathered} \tag{6.13}$$

For ease of analysis we split Expr. 6.13 into two terms and analyze them separately. The two terms are:

$$e^{\left[(n+\nu)\, \cosh^{-1}\left(\frac{n+\nu}{2x+\delta}\right) - n\, \cosh^{-1}\left(\frac{n}{x}\right) - \nu\, \cosh^{-1}\left(\frac{\nu}{x}\right)\right]} \tag{6.14}$$

and

$$e^{\left[\sqrt{n^2-x^2}+\sqrt{\nu^2-x^2}-\sqrt{(n+\nu)^2-(2x+\delta)^2}\right]} \tag{6.15}$$

Consider first Expr. 6.14. Using $\cosh^{-1} z = \log(z + \sqrt{z^2-1})$ we have:

$$e^{\left[(n+\nu)\,\log\left(\frac{n+\nu}{2x+\delta}+\sqrt{(\frac{n+\nu}{2x+\delta})^2-1}\right)-n\,\log\left(\frac{n}{x}+\sqrt{(\frac{n}{x})^2-1}\right)-\nu\,\log\left(\frac{\nu}{x}+\sqrt{(\frac{\nu}{x})^2-1}\right)\right]} \tag{6.16}$$

This simplifies to:

$$\left(\frac{n+\nu}{2x+\delta}+\sqrt{\left(\frac{n+\nu}{2x+\delta}\right)^2-1}\right)^{(n+\nu)}\left(\frac{n}{x}+\sqrt{\left(\frac{n}{x}\right)^2-1}\right)^{-n}\left(\frac{\nu}{x}+\sqrt{\left(\frac{\nu}{x}\right)^2-1}\right)^{-\nu} \tag{6.17}$$

For $n/x \gg 1$ and $\nu/x \gg 1$ (which is what we encounter for small gaps) this can be written as:

$$\begin{aligned}
&\left(\frac{2(n+\nu)}{2x+\delta}\right)^{(n+\nu)}\left(\frac{2n}{x}\right)^{-n}\left(\frac{2\nu}{x}\right)^{-\nu}\\
&=\left(\frac{n+\nu}{2x+\delta}\right)^{(n+\nu)}\left(\frac{n}{x}\right)^{-n}\left(\frac{\nu}{x}\right)^{-\nu}\\
&=\left(\frac{(n+\nu)^{(n+\nu)}}{n^n\nu^\nu}\right)\left(\frac{x^n x^\nu}{(2x+\delta)^{n+\nu}}\right)\\
&=\left(\frac{(n+\nu)^n\,(n+\nu)^\nu}{n^n\nu^\nu}\right)\left(\frac{x^n x^\nu}{(2x+\delta)^{n+\nu}}\right)\\
&=\left(1+\frac{\nu}{n}\right)^n\left(1+\frac{n}{\nu}\right)^\nu\left(2+\frac{\delta}{x}\right)^{-(n+\nu)}\\
&=\left(1+\frac{\nu}{n}\right)^n\left(1+\frac{n}{\nu}\right)^\nu 2^{-(n+\nu)}\left(1+\frac{\delta}{2x}\right)^{-(n+\nu)}\\
&=\frac{\left(1+\frac{\nu}{n}\right)^n\left(1+\frac{n}{\nu}\right)^\nu}{2^{(n+\nu)}}\left(1+\frac{\delta}{2x}\right)^{-(n+\nu)}
\end{aligned} \tag{6.18}$$

For $\delta = 0$, the expression reduces to:

$$\frac{\left(1+\frac{\nu}{n}\right)^n\left(1+\frac{n}{\nu}\right)^\nu}{2^{(n+\nu)}} \tag{6.19}$$

The maximum value of this expression can be shown to occur at $n = \nu$ (Taking partial derivatives with respect to n and ν and solving the two equations simultaneously). And the

maximum value is 1. Now consider the other part in Expr. 6.13 i.e.

$$e^{\left[\sqrt{n^2-x^2}+\sqrt{\nu^2-x^2}-\sqrt{(n+\nu)^2-(2x+\delta)^2}\right]} \qquad \text{(6.15 revisited)}$$

At $\delta = 0$ the power term in Expr. 6.15 reduces to:

$$\sqrt{n^2-x^2}+\sqrt{\nu^2-x^2}-\sqrt{(n+\nu)^2-(2x)^2} \tag{6.20}$$

It is possible to show that $\sqrt{n^2-x^2}+\sqrt{\nu^2-x^2} < \sqrt{(n+\nu)^2-(2x)^2}$ for all $n \neq \nu$ and that the maximum value of the expression (equal to 0) happens when $n = \nu$. To go about this, consider the following steps. We need to show:

$$\sqrt{n^2-x^2}+\sqrt{\nu^2-x^2} < \sqrt{(n+\nu)^2-(2x)^2} \tag{6.21}$$

Squaring both sides of Eq. 6.21:

$$n^2-x^2+\nu^2-x^2+2\sqrt{n^2-x^2}\sqrt{\nu^2-x^2} < (n+\nu)^2-(2x)^2 \tag{6.22}$$

Canceling common terms

$$\sqrt{n^2-x^2}\sqrt{\nu^2-x^2} < n\nu - x^2 \tag{6.23}$$

Squaring both sides and simplifying:

$$-\nu^2-n^2 < -2n\nu \tag{6.24}$$

or

$$\nu^2+n^2 > 2n\nu \tag{6.25}$$

which is true (since $(n-\nu)^2 > 0$). Thus Expr. 6.15 attains a maximum value (=1) when $n = \nu$. Since we have shown that both the factors in Expr. 6.13 attain maximum value when $n = \nu$, thus we can conclude that the maximum value of Expr. 6.12, which is representative of the value of the normalized scalar translation coefficient for equal sized spheres, occurs at $n = \nu$.

6.3.2 Analysis for unequal sized spheres

For analyzing the case of unequal sized spheres we go back to Expr. 6.4. Employing the asymptotic forms for the spherical Bessel and Hankel functions given in Eqs. 6.7, 6.10, and 6.11, we get the order of magnitude estimate of Expr. 6.4 to be:

$$e^{\left[\sqrt{n^2-(k_f\,R_1)^2}+\sqrt{\nu^2-(k_f\,R_2)^2}-\sqrt{(n+\nu)^2-(k_f\,R_1+k_f\,R_2+\delta)^2}\right]}\times e^{\left[(n+\nu)\,\cosh^{-1}(\frac{n+\nu}{k_f\,R_1+k_f\,R_2+\delta})-n\,\cosh^{-1}(\frac{n}{k_f\,R_1})-\nu\,\cosh^{-1}(\frac{\nu}{k_f\,R_2})\right]} \tag{6.26}$$

On similar lines as was shown for the equal-spheres case, we split the above expression into two terms and analyze each of them separately. Consider first:

$$e^{\left[(n+\nu)\,\cosh^{-1}(\frac{n+\nu}{k_f\,R_1+k_f\,R_2+\delta})-n\,\cosh^{-1}(\frac{n}{k_f\,R_1})-\nu\,\cosh^{-1}(\frac{\nu}{k_f\,R_2})\right]} \tag{6.27}$$

Using: $\cosh^{-1}[z] = \log[z + \sqrt{z^2-1}]$ we get:

$$(n+\nu)\cosh^{-1}\left(\frac{n+\nu}{k_f\,R_1+k_f\,R_2+\delta}\right) = (n+\nu)\log\left(\frac{n+\nu}{k_f\,R_1+k_f\,R_2+\delta}+\sqrt{\left(\frac{n+\nu}{k_f\,R_1+k_f\,R_2+\delta}\right)^2-1}\right) \tag{6.28}$$

But since we are dealing with $n \gg k_f\,R_1$ and $\nu \gg k_f\,R_2$, the above term in Expr. 6.27 reduces to:

$$\left(2\frac{n+\nu}{k_f\,R_1+k_f\,R_2+\delta}\right)^{n+\nu} \tag{6.29}$$

Applying the same modifications to the other $\cosh^{-1}$ terms in Expr. 6.27 we get:

$$\left(\frac{n+\nu}{k_f\,R_1+k_f\,R_2+\delta}\right)^{n+\nu}\left(\frac{n}{k_f\,R_1}\right)^{-n}\left(\frac{\nu}{k_f\,R_2}\right)^{-\nu} \tag{6.30}$$

When δ decreases to zero, the remaining terms can be simplified as follows:

$$\left(1+\frac{n}{\nu}\right)^{n}\left(1+\frac{\nu}{n}\right)^{\nu}\left(\frac{k_f\,R_1}{k_f\,R_1+k_f\,R_2}\right)^{n}\left(\frac{k_f\,R_2}{k_f\,R_1+k_f\,R_2}\right)^{\nu} \tag{6.31}$$

which can be written as:

$$\left(1+\frac{n}{\nu}\right)^{n}\left(1+\frac{\nu}{n}\right)^{\nu}\left(1+\frac{R_2}{R_1}\right)^{-n}\left(1+\frac{R_1}{R_2}\right)^{-\nu} \tag{6.32}$$

This can be shown to attain a maximum value (=1) when we have:

$$\nu = n\frac{R_2}{R_1} \tag{6.33}$$

Now consider the other part of Expr. 6.26 i.e.

$$e^{\left[\sqrt{n^2-(k_f\,R_1)^2}+\sqrt{\nu^2-(k_f\,R_2)^2}-\sqrt{(n+\nu)^2-(k_f\,R_1+k_f\,R_2+\delta)^2}\right]} \tag{6.34}$$

When δ reduces to zero the expression becomes maximum (= 1) when

$$\frac{\nu}{n} = \frac{R_2}{R_1} \tag{6.35}$$

Since both the expressions 6.27 and 6.34 attain maximum when Eq. 6.35 holds true, thus we can conclude that the condition for Expr. 6.4 (which is representative of the value of the normalized scalar translation coefficient) to attain maximum is given by Eq. 6.35. This condition conforms well with what is observed in the contour plots of Fig. 6.1 where the line representing Eq. 6.35 has been superimposed on the contour plots.

6.4 Conclusions

In this chapter the behavior of the normalized translation coefficients with varying radius ratio was demonstrated pictorially using contour plots and an attempt was made to explain this behavior analytically. The importance of this behavior stems from the fact that this behavior can be taken advantage of to extend the computational model for two spheres to unequal sized spheres with large radius ratios which was computationally improbable earlier.

Chapter 7

Convergence analysis

7.1 Introduction

As explained in Chapter 3 the completeness of the functions $\boldsymbol{M}_{lm}^{(p)}(k\boldsymbol{r})$ and $\boldsymbol{N}_{lm}^{(p)}(k\boldsymbol{r})$ allows the scattered electromagnetic field to be expanded in an infinite series as:

$$\boldsymbol{E}(\boldsymbol{r}) = \sum_{\substack{m=-l \\ l=1}}^{\substack{l=\infty \\ m=l}} \left[A_{lm}^{(p)} \boldsymbol{M}_{lm}^{(p)}(k\boldsymbol{r}) + B_{lm}^{(p)} \boldsymbol{N}_{lm}^{(p)}(k\boldsymbol{r})\right]; \qquad \text{(2.19 revisited)}$$

$$\boldsymbol{H}(\boldsymbol{r}) = \frac{ik}{\omega\mu} \sum_{\substack{m=-l \\ l=1}}^{\substack{l=\infty \\ m=l}} \left[A_{lm}^{(p)} \boldsymbol{N}_{lm}^{(p)}(k\boldsymbol{r}) + B_{lm}^{(p)} \boldsymbol{M}_{lm}^{(p)}(k\boldsymbol{r})\right]; \qquad \text{(2.20 revisited)}$$

where, $k^2(\boldsymbol{r}) = \omega^2 \varepsilon(\boldsymbol{r}) \mu(\boldsymbol{r})$. Here the dielectric permittivity, $\varepsilon(\boldsymbol{r})$, and magnetic permeability, $\mu(\boldsymbol{r})$, are frequency dependent piecewise constant functions with a discontinuity at the surface of the sphere. Since we are dealing with nonmagnetic materials $\mu(\boldsymbol{r}) = 1$. For the interior of the sphere, we use $p = 1$ (regular vector spherical waves). For the exterior of the sphere, we use $p = 3$ (outgoing vector spherical waves). The coefficients $A_{lm}^{(p)}$ and $B_{lm}^{(p)}$ are obtained by satisfying the boundary conditions on the surface of the sphere.

Irrespective of single sphere or multiple sphere scattering, as a practical matter, the infinite series in Eq. 2.19 and Eq. 2.20 need to be truncated (in indices l and m), retaining only enough terms necessary to ensure a sufficiently accurate approximation. The number

of terms to retain depends on different length scales pertinent to the problem. For far–field scattering by a single sphere, the relevant length scales are the radius of the sphere, R, and the wavelength of incident radiation, λ. The number of terms for convergence N_{conv} is given by [80; 52; 81]

$$N_{conv} = a + x + bx^{1/3} \tag{7.1}$$

where $x = 2\pi R/\lambda$, and a is 1 or 2 and b is 4 or 4.05, depending on x. These values of a and b are obtained empirically and the resulting expansion gives an error less than 0.01 %. For far–field scattering by two spheres shown in Fig. 3.1, the relevant length scales are the radii of spheres R_1 and R_2, the wavelength λ, and the center–to–center distance between the spheres, D. In this case, a different criterion has been proposed [82]

$$N_{conv} = e\pi\frac{D}{\lambda}, \tag{7.2}$$

where e is the base of natural logarithm. While the convergence criteria in Eq. 7.1 and 7.2 are relevant for far–field scattering, near–field effects lead to several peculiarities and hence we can expect different criteria for the number of terms of convergence. This is especially true when surface plasmon and/or phonon polaritons lead to enormous enhancement of the field amplitude near the interfaces. Hence for problems involving near–field effects the role of the gap d between the bodies can be expected to be prominent in deciding the number of terms for convergence.

The fact that scattering and absorption of evanescent waves lead to increased contributions from higher order terms has been recognized previously. Quinten et al [83] while analyzing scattering and extinction by small particles noted the increase in the contributions from higher order modes for scattering and absorption by evanescent waves as compared to propagating waves. Yannopapas and Vitanov [84] noticed difficulty in attaining convergence while calculating local density of states (LDOS) near the surface of a metallic sphere. However an explicit form for the number of terms for convergence along the lines of Eq. 7.1 or 7.2 has not been proposed for near–field scattering. A brief mention of a convergence criteria was made by Narayanaswamy and Chen in their analysis of surface phonon polariton mediated

near–field radiative transfer between two closely spaced spheres [36]. While a scaling form for the number of terms of convergence was proposed, a more detailed error analysis was not pursued. In this chapter a comprehensive error analysis has been made for computation of near–field radiative transfer between two silica spheres of equal radii. Based on the error analysis a criterion for the number of terms required to attain an error of less than 1% has been proposed, and this formulation has also been extended for the case of two spheres of unequal radii.

7.2 Analysis for the two sphere problem

The configuration of two spheres which lie on the common z-axis and whose centers are separated by a distance D is shown in Fig. 3.1. The symmetry in this configuration of the two spheres ensures that Eq. 2.19 and Eq. 2.20 can be simplified to be written as:

$$\boldsymbol{E}(\boldsymbol{r}) = \sum_{\substack{l=(m,1)\\m=0}}^{\substack{m=\infty\\l=\infty}} \left[A_{lm}^{(p)} \boldsymbol{M}_{lm}^{(p)}(k\boldsymbol{r}) + B_{lm}^{(p)} \boldsymbol{N}_{lm}^{(p)}(k\boldsymbol{r}) \right] \tag{7.3}$$

$$\boldsymbol{H}(\boldsymbol{r}) = \frac{ik}{\omega\mu} \sum_{\substack{l=(m,1)\\m=0}}^{\substack{m=\infty\\l=\infty}} \left[A_{lm}^{(p)} \boldsymbol{N}_{lm}^{(p)}(k\boldsymbol{r}) + B_{lm}^{(p)} \boldsymbol{M}_{lm}^{(p)}(k\boldsymbol{r}) \right], \tag{7.4}$$

where the symbol $(m,1)$ refers to the greater of m and 1. This step is more useful than the trivial simplification it appears to be. In Eq. 7.3 and 7.4, the computation for a given value of m is decoupled almost entirely from other values of m. The only link between computations for different values of m is that the recursive scheme for calculating vector translation coefficients at m requires the coefficients for $m-1$ and $m-2$ [51].

Just as scattering or absorption coefficients can be used as metrics to gauge convergence for far–field radiation, we can similarly use radiative conductance G (Eq. 3.39 in Chapter 3) to gauge the convergence of scattering response in the near–field region. The heat transfer parameter G is related to the electromagnetic problem by expressing it in terms of the vector spherical expansion of the dyadic Green's function of the vector Helmholtz equation [36]. The expansion is similar to Eq. 2.19 and 2.20 [61; 85]. Further details of the elctromagnetic

formulation are available in Narayanaswamy and Chen [36]. The spheres are made of silica, the dielectric function of which has been shown as a function of frequency in Fig. 2.3. By observing the variation of the refractive index with frequency it can be deduced that silica supports surface phonon–polaritons between 0.05-0.065 eV and 0.13-0.1405 eV. Hence computations are carried out in the frequency range 0.04-0.16 eV. In addition to conductance G, we also define a spectral conductance $G_\omega(\omega)$ that is related to G by the relation $G = \int G_\omega(\omega)\, d\omega$. The behavior of $G_\omega(\omega)$ is useful in showing the difference in convergence depending on whether or not surface phonon polaritons are active at that frequency. The numerical scheme itself proceeds along the following lines: (1) Choose a value of $l = N_{conv}$ to truncate the summation over l in Eq. 7.3 and Eq. 7.4. (2) Compute the electric and magnetic fields for each value of m, and from that the contribution to $G_\omega(\omega)$. This step is continued until the contribution from $m = M_{conv}$ has reached a sufficiently low value. (3) Repeat steps (1) and (2) for all frequencies to obtain G. Even though all values of m satisfying $|m| \leq N_{conv}$ can contribute to the overall conductance, we will show that $M_{conv} \ll N_{conv}$ in practice.

7.3 Convergence of summation over l: derivation of a convergence criterion based on comparison with planar surfaces

To find the number of l terms required in Eq. 7.3 and Eq. 7.4 for convergence of near–field quantities for the two sphere problem, comparison is drawn with the well understood case of near–field transfer between two half–spaces [24; 26; 86]. In the latter case, the summations in Eq. 7.3 and Eq. 7.4 are replaced by an integral of the form $\int_0^\infty dk_{in} f(k_{in}) \exp(-2k_{in}z)$, where k_{in} is the in–plane wavevector, z is the spacing between the two half–spaces, and $f(k_{in})$ is an appropriately defined function. It is seen that only wavevectors satisfying the condition $k_{in} \lesssim 1/z$ contribute to the integral. The equivalent of the in–plane wavevector for a sphere is the wavelength of spatial variation of the field on the surface of the sphere. For $l = N_{conv}$, the periodicity of the spatial variation is determined by the behavior of $Y_{N_{conv},m}$, $|m| \leq N_{conv}$. The smallest wavelength on the surface is given by $2\pi R/N_{conv}$, resulting in a maximum in–plane wavevector–equivalent of N_{conv}/R. By analogy with the convergence

requirement for two half–spaces, we obtain $N_{conv}/R \sim 1/d$ or

$$N_{conv} = C\frac{R}{d}, \tag{7.5}$$

where C is a constant (or a weak function of R) that is dependent on the desired accuracy of the conductance. This criterion is sufficient for the analysis of radiative transfer between spheres of submicron radii where the radiative transfer is dominated by near–field effects. However, for spheres of larger radii where the contribution from propagating waves is not negligible, we have observed that the above criterion is not sufficient to attain convergence and the equation needs to be modified to:

$$N_{conv} = C\frac{R}{d} + e\pi\frac{D}{\lambda}, \tag{7.6}$$

with the additional term being taken from Eq. 7.2.

In order to quantify the error due to retaining contributions only from wave functions with $l \leq N$ in Eq. 7.3 and Eq. 7.4, the conductance G and spectral conductance G_ω are plotted as a function of N in Fig. 7.1 and Fig. 7.2 respectively. It is seen that an exponentially decaying function of the form $G(N) = G_\infty + ae^{-bN}$ matches the variation of G (and G_ω) adequately, where G_∞ denotes the value of G as $N \to \infty$, and a and b are constants. The relative error $E(N)$ (in %) for total conductance, defined as $E(N) = (G(N) - G_\infty)/G_\infty$, is also plotted in Fig. 7.1. The conductance $G(N)$ and error $E(N)$ for $R = 10$ μm and $R = 25$ μm, with $d/R = 0.01$, are shown in Fig. 7.1(a) and 7.1(b) respectively. The difference between the convergence of the numerical method at nonresonant (0.1005 eV) and resonant (0.061 eV) frequencies is illustrated by plotting the spectral conductance for $R = 10$ μm and $d/R = 0.01$ as a function of N in Fig. 7.2(a) and Fig. 7.2(b). Also plotted are the relative errors in spectral conductance at these frequencies. The exponential decay in the error values is observed for both these frequencies. As expected, convergence to a given relative error requires a larger value of N at a resonant frequency than at a non–resonant frequency. For instance, at $N = 2R/d$ the relative error for the resonant frequency is ≈ 3 % while it is ≈ 0.2 % at the non–resonant frequency.

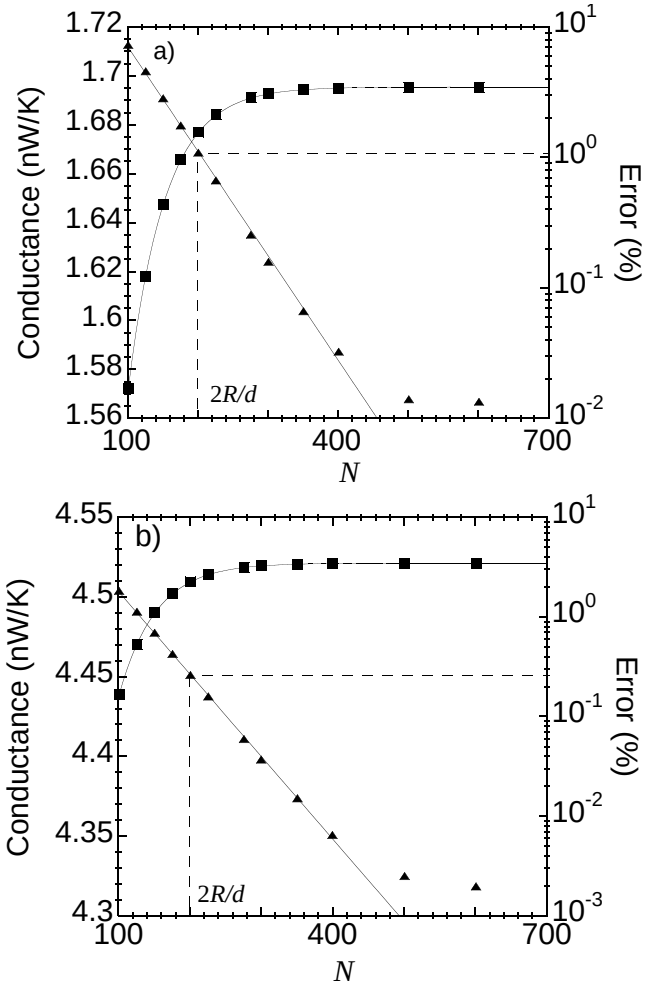

Figure 7.1: Convergence of conductance (on the left axis) and error (on the right axis) shown for **(a)** $R = 10\,\mu$m spheres at $d = 100$ nm and **(b)** $R = 25\,\mu$m spheres at $d = 250$ nm. The solid line through the relative error data points in included to illustrate the exponentially decaying trend.

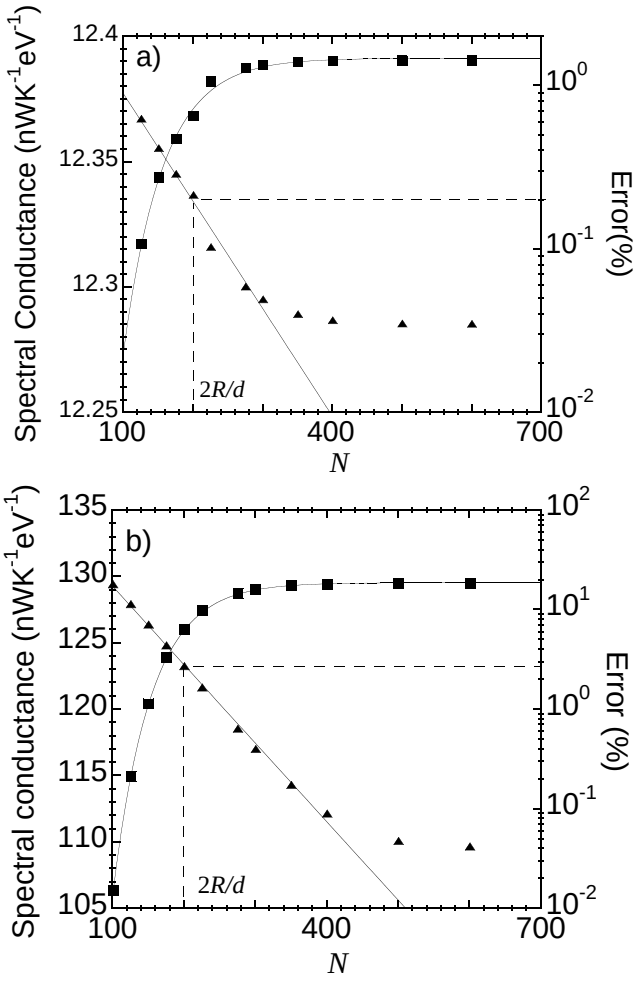

Figure 7.2: Convergence of spectral conductance (on the left axis) and error (on the right axis) shown for $R = 10\,\mu$m spheres for $d = 100$ nm at **(a)** a nonresonant frequency (0.1005 eV) and **(b)** a resonant frequency (0.061 eV).

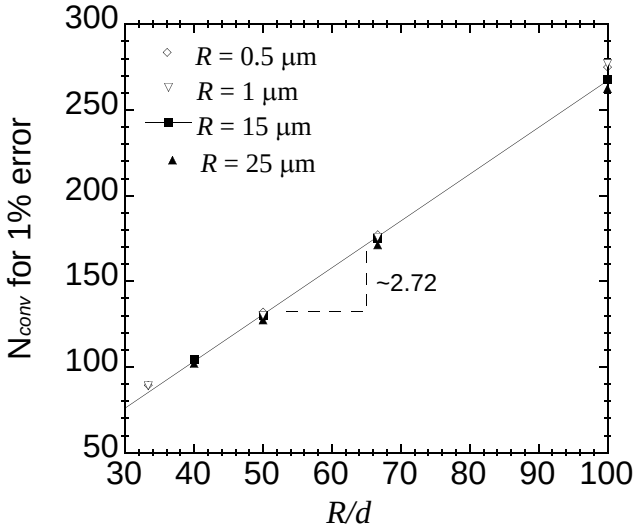

Figure 7.3: Variation of N_{conv} with R/d for two equal–sized spheres with R = 500 nm, 1 μm, 15 μm and 25 μm

While Eq. 7.6 proposes a scaling form for N_{conv}, the constant C needs to be quantified for attaining a given relative error. This can be obtained by analyzing the variation of N_{conv} with R/d for spheres of different radii. Figure 7.3 shows the dependence of N_{conv} on R/d for spheres of both submicron radii and larger radii at the resonant frequency (0.061 eV). It is apparent that C assumes a constant value (≈ 2.72) at the resonant frequency. For total conductance, $C = 2$ is sufficient to attain 1% error as seen in Fig. 7.1. It should be noted that these values of C are particular to the case of radiative transfer between silica spheres. This constant is expected to vary weakly with the dielectric properties of the material(s) of the spheres. However the scaling form shown in Eq. 7.5 was proposed without taking into consideration the material of the spheres and hence can be used for any material that supports surface phonon or plasmon polaritons.

For the sake of completion we have also analyzed the convergence of conductance between spheres of unequal radii. For two spheres of radii R_1 and R_2 with $R_1 < R_2$, N_{conv} can be expected to scale with R_2 as:

$$N_{conv} = C\frac{R_2}{d} + e\pi\frac{D}{\lambda}, \tag{7.7}$$

The variation of spectral conductance G_ω as a function of N for two spheres with $R_1 = 2\,\mu$m, $R_2 = 40\,\mu$m and $d = 200$ nm at a nonresonant frequency (0.1005 eV) and a resonant frequency (0.061 eV) are shown in Fig. 7.4(a) and Fig. 7.4(b) respectively. Due to computational constraints the maximum number of terms considered for this study has been limited to $N = 3R_2/d$. From Fig. 7.4(b) we note that at the resonant frequency the value of constant C in Eq. 7.7, for 1% error, turns out approximately to be the same as the value obtained for equal radii [see Fig. 7.2(b)]. Hence we conclude that Eq. 7.7 is expected to hold true even in the limiting case of $R_1 \to 0$, which implies that to determine the scattered field due to excitation by a dipole current source at a distance $z(\ll \lambda)$ from the surface of a sphere of radius R, N_{conv} scales as R/z. This can be used as a criterion for the convergence of the number of terms to be retained in the summation over l while calculating quantities such as LDOS near the surface of a sphere, like in [84].

7.3.1 Convergence of summation over m

In addition to truncating the infinite series in Eq. 7.3 and 7.4 with respect to l, it is also necessary to truncate the series in m. Since each value of m contributes independent of other values of m to the spectral conductance (and conductance), we can write $G_\omega = \sum_{m=0}^{\max(l)} G_\omega^{(m)}$, where $\max(l)$ is the maximum value of l used in the computation. The variation of $G_\omega^{(m)}$ with m between two spheres of radii $R = 25\,\mu$m and gap $d = 250$ nm at a resonant frequency ($\omega = 0.061$ eV) and a nonresonant frequency ($\omega = 0.1005$ eV) are shown in Fig. 7.5(a) and Fig. 7.5(b) respectively. We notice that there is an approximately exponential decay [$G_\omega^{(m)} \approx A\exp(-Bm)$] in the contributions from higher values of m. The values of B for the resonant and nonresonant frequency are shown in Fig. 7.5(a) and Fig. 7.5(b) respectively. This observation enables us to propose an empirical criterion for the number of terms M_{conv} to be retained in summation over m as:

$$G_\omega^{(M_{conv})} = 0.005 G_\omega^{(0)} \tag{7.8}$$

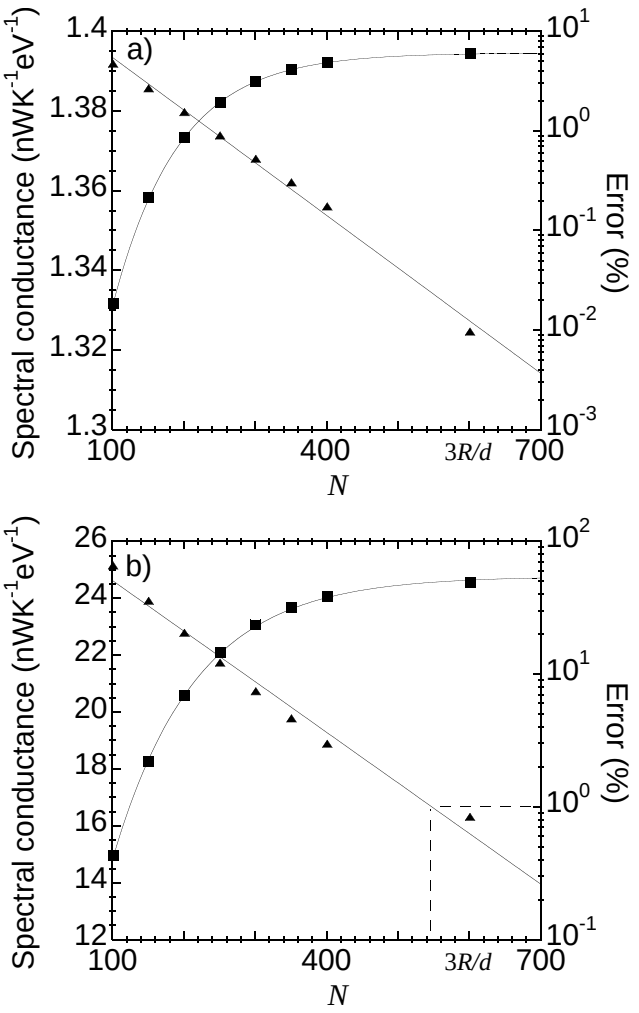

Figure 7.4: Convergence of spectral conductance shown for $R_1 = 2\,\mu$m and $R_2 = 40\,\mu$m spheres for $d = 200$ nm at **(a)** a nonresonant frequency (0.1005 eV) **(b)** a resonant frequency (0.061 eV).

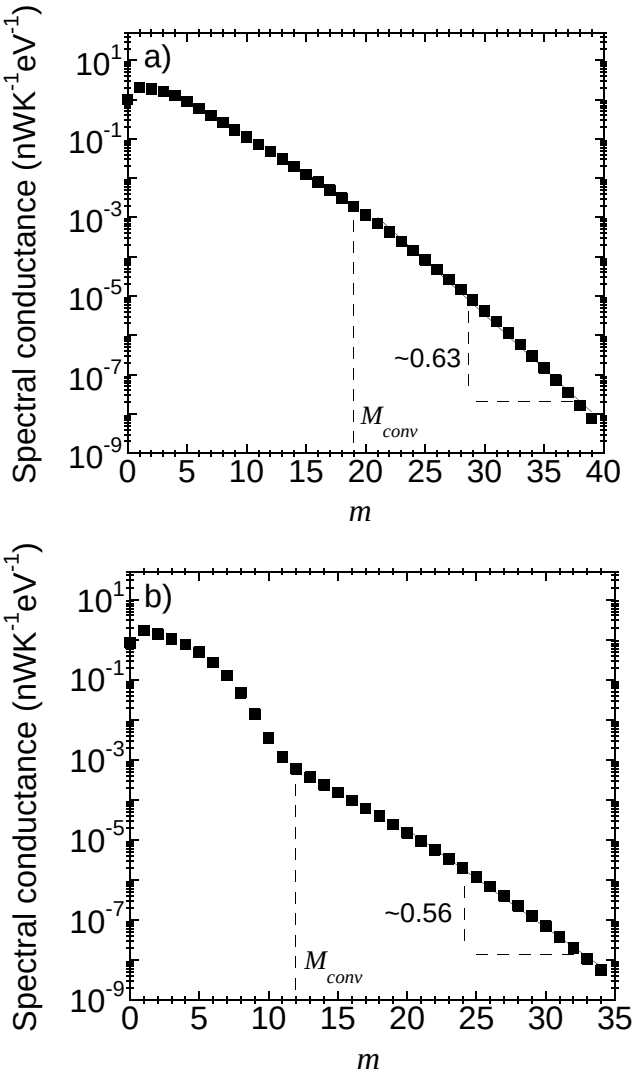

Figure 7.5: Contribution to spectral conductance from each value of m for $R = 25\,\mu$m and $d = 250$ nm at **(a)** a resonant frequency (0.061 eV) **(b)** nonresonant frequency (0.1005 eV). The rate of exponential decay (B) for higher values of m at the resonant frequency is also shown.

i.e only wavefunctions with contribution to spectral conductance higher than 0.5% of the contribution from $m = 0$ are used for the series summation in m in Eq. 7.3 and Eq. 7.4. For the case considered in Fig. 7.5, the error due to retaining contributions only from the wavefunctions satisfying Eq. 7.8 is $\approx 0.028\%$ at the resonant frequency and $\approx 0.024\%$ at the nonresonant frequency.

7.4 Derivation based on the one-term approximation of normalized translation coefficients

7.4.1 Motivation

The convergence criterion for the number of vector spherical waves required for computing the near-field radiative transfer between two spherical bodies in Eq. 7.7 was derived heuristically based on comparison with the convergence criterion for the near-field radiative transfer between planar bodies. In particular, the observation that only the in-plane wavevectors with magnitude less than $1/z$ (z is the gap between the planar surfaces) contribute significantly to the radiative heat transfer between planar surfaces has been used to arrive at the corresponding criterion for the radiative transfer between spherical bodies. However, as has been shown in this chapter, a similar form of convergence criterion can be derived without having to refer to the corresponding relation for planar bodies, by analyzing the asymptotic forms for the normalized translation coefficients. From this, the role of translation coefficients in obtaining convergence in the vector eigenfunction expansion method of computing near-field radiative transfer becomes explicit.

7.4.2 Discussion

As explained in Chapter 5, using the one-term approximation it is possible to show that:

$$\beta_{\nu m,nm} \sim z^{(3)}_{n+\nu}(k_f D) \tag{7.9}$$

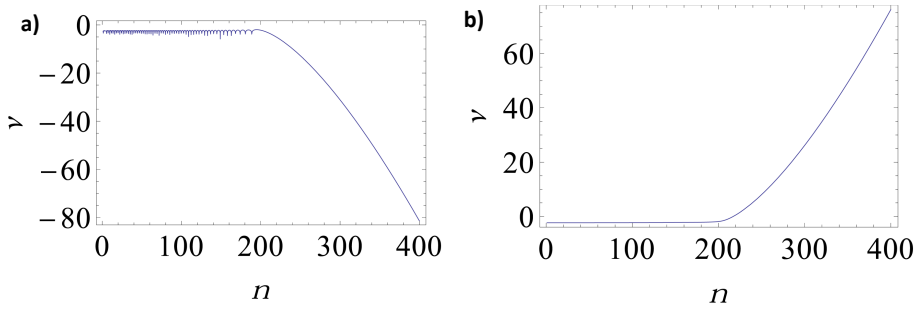

Figure 7.6: **(a)** Plot of $\log|z_n^{(1)}(200)|$ as a function of n; **(b)** Plot of $\log|z_n^{(3)}(200)|$ as a function of n

where, $\beta_{\nu m,nm}$ is the scalar translation coefficient and $z_{n+\nu}^{(3)}(k_f D)$ is the spherical Hankel function with order $n+\nu$ and argument $k_f D$. (Eq. 7.9 takes into account only an order of magnitude estimation; there will be other constants in the expression for the exact form of $\beta_{\nu m,nm}$). The normalized form of the scalar translation coefficient $\beta^N_{\nu m,nm}$ (from Chapter 4) is thus of the order:

$$\beta^N_{\nu m,nm} \sim z_{n+\nu}^{(3)}(k_f D)\frac{z_\nu^{(1)}(k_f R_1)}{z_n^{(3)}(k_f R_2)} \tag{7.10}$$

The behavior of the expression in RHS (right hand side) of Eq. 7.10 has to be understood in order to comprehend how the translation coefficients affects the convergence in the near-field radiative heat transfer calculation. To go about this, consider the log plots of the absolute value of spherical Bessel and Hankel functions $z_n^{(1)}(r)$ and $z_n^{(3)}(r)$ as a function of the order n and for a particular argument r as shown in Fig. 7.6(a) and 7.6(b). The arguments chosen for these plots are random values selected for demonstrative purposes only (the values chosen are specified in the caption). It is observed from these plots that the absolute values for the spherical Bessel (Hankel) function has a oscillatory/sinusoidal behavior when $n \lesssim r$ and decreases (increases) exponentially when $n \gg r$.

Consider the case of two equal spheres separated by a gap d such that $d \ll R_1, R_2$. We then have $k_f D \approx k_f R_1 + k_f R_2$ with $k_f d \to 0$. The values for $k_f R_1$, $k_f R_2$ and $k_f D$ can be chosen to be ≈ 20, ($R_1, R_2 \approx 25\,\mu$ m, $\omega \approx 0.16$ eV). At these values of $k_f R_1$, $k_f R_2$, and $k_f D$ we can expect the absolute values of Bessel (Hankel) function to be nearly constant

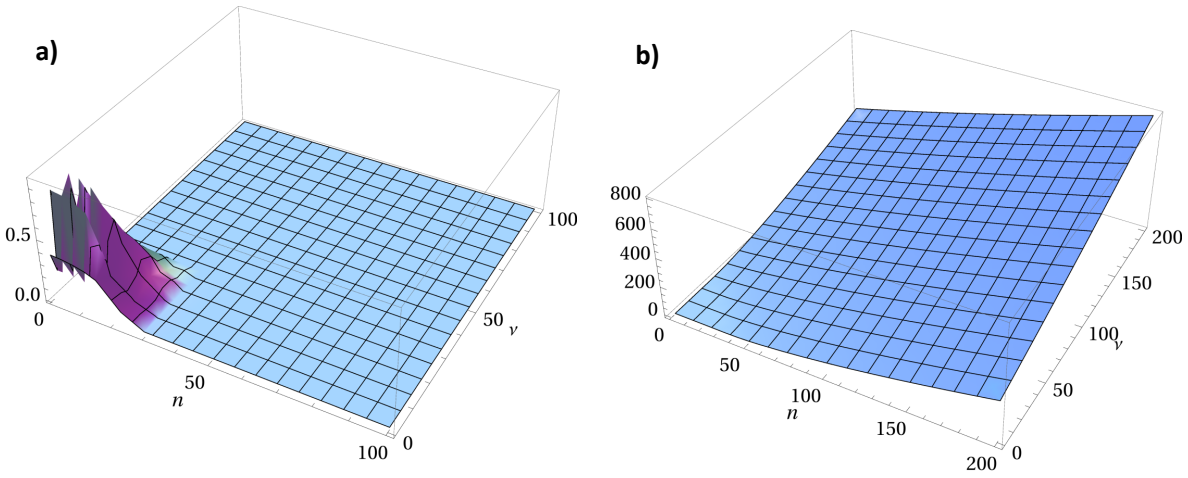

Figure 7.7: **(a)** Plot of $\left|\frac{z_\nu^{(1)}(20)}{z_n^{(3)}(20)}\right|$ as a function of n and ν; **(b)** Plot of $\log|z_{n+\nu}^{(3)}(20)|$ as a function of n and ν

(oscillating) till $z = 20$ before starting to decrease (increase) rapidly when $n \gtrsim 20$. Three-dimensional plots of the ratio $\frac{z_\nu^{(1)}(k_f R_1)}{z_n^{(3)}(k_f R_2)}$ and the function $z_{n+\nu}^{(3)}(k_f D)$ is shown in Fig. 7.7(a) and Fig. 7.7(b) respectively, as a function of n and ν with $k_f R_1 = k_f R_2 = 20$ and $k_f D = 40$:

The steep fall observed in Fig. 7.7(a) for $(n,\, \nu) > 20$ is expected from the behavior of the spherical Bessel and Hankel functions shown in Fig. 7.6 From Fig. 7.7(b) it is observed that the absolute value of $z_{n+\nu}^{(3)}(k_f D)$ is largest along the diagonal line $n = \nu$. As observed from Eq. 7.10 it is the product of the two functions plotted in Fig. 7.7 that is relevant. The product of these two functions is plotted in Fig. 7.8. To understand the behavior of the function when the gap between the two spheres varies, I have plotted the function given in Eq. 7.10 for $k_f R_1 = k_f R_2 = 20$ but different values of $k_f D$ such that $k_f D \approx k_f R_1 + k_f R_2$. In Fig. 7.8(a) $k_f D = k_f R_1 + k_f R_2 = 40$, in Fig. 7.8(b), (c), and (d) $k_f D$ is gradually increased to 40.2, 40.5 and 41 respectively.

The following observations can be made from Fig. 7.8(a) where $k_f D = k_f R_1 + k_f R_2$. The increasing function shown in Fig. 7.7(b) compensates for the rapidly decreasing values of the function shown in Fig. 7.7(a) (when the two functions are multiplied) and the product of these two functions (which gives Eq. 7.10) is nearly constant along the diagonal. While

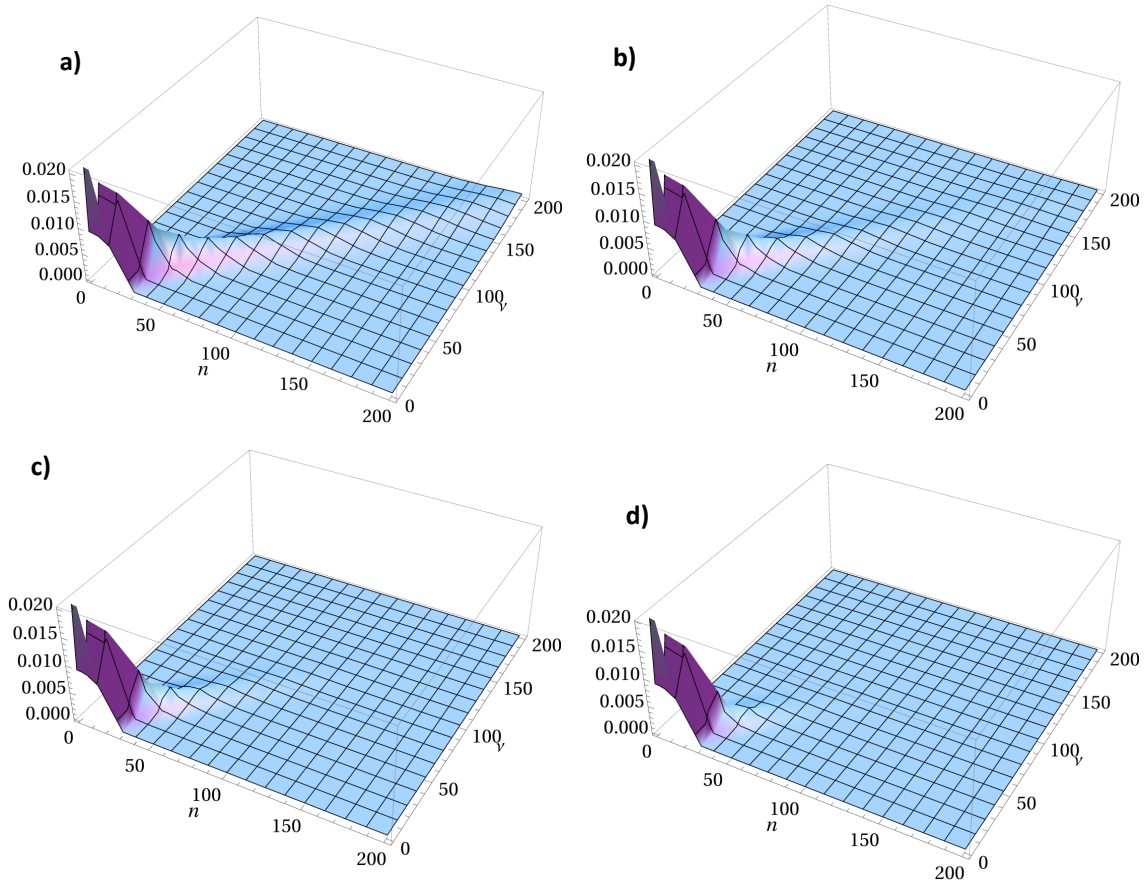

Figure 7.8: Plot of $\left|\frac{z_\nu^{(1)}(k_f R_1)}{z_n^{(3)}(k_f R_2)} z_{n+\nu}^{(3)}(k_f D)\right|$ as a function of n and ν for $k_f R_1 = k_f R_2 = 20$ but for varying $k_f D$ The values of $k_f D$ are chosen to be **(a)** $k_f D = 40$, **(b)** $k_f D = 40.2$, **(c)** $k_f D = 40.5$, and **(d)** $k_f D = 41$

only values up to n, ν of 200 is shown in the plot, the values of the function can be shown to be constant even when extended to larger values of n and ν such that $(n, \nu) \to \infty$. However, when $k_f D > k_f R_1 + k_f R_2$ the increasing function in Fig. 7.7(b) can no longer compensate for the rapidly decreasing values of the function shown in Fig. 7.7(a) and values can be observed to decrease along the diagonal after a few terms. The closer the value of $k_f D$ to $k_f R_1 + k_f R_2$ more will be the number of terms required for value of the function to start decreasing along the diagonal as observed in Fig. 7.8(b), (c), and (d). The number of terms required for the values to decrease along the diagonal thus decides the number of vector spherical waves required for the convergence of the near-field radiative transfer calculation. This is shown analytically in the next section (Section 7.5).

7.5 Asymptotic analysis

Consider Expr. 6.4 which gives the order of magnitude estimate of the normalized scalar translation coefficient $\beta_{\nu m,nm}$. It reads:

$$z^{(3)}_{n+\nu}(k_f D)\frac{z^{(1)}_n(k_f R_1)}{z^{(3)}_\nu(k_f R_2)} \tag{7.11}$$

Employing the asymptotic forms for the spherical Bessel and spherical Hankel functions given by Exprs. 6.7, 6.10 and 6.11, the order of magnitude of Expr. 7.11 has been shown to reduce to Expr. 6.26 which consists of product of two exponential terms namely:

$$e^{\left[\sqrt{n^2-(k_f R_1)^2}+\sqrt{\nu^2-(k_f R_2)^2}-\sqrt{(n+\nu)^2-(k_f R_1+k_f R_2+\delta)^2}\right]} \qquad \text{(6.27 revisited)}$$

and

$$e^{\left[(n+\nu)\,\cosh^{-1}\left(\frac{n+\nu}{k_f R_1+k_f R_2+\delta}\right)-\nu\,\cosh^{-1}\left(\frac{\nu}{k_f R_2}\right)-n\,\cosh^{-1}\left(\frac{n}{k_f R_1}\right)\right]} \qquad \text{(6.34 revisited)}$$

An analysis of Exprs. 6.27 and 6.34 along the line of maximum (given by Eq. 6.35) gives us an estimate of the number of terms that are important along this line, and hence an

estimate of the number of terms for convergence as discussed in Sec. 7.4.2. The Taylor's series expansion of Expr. 6.27 is given by:

$$e^{\left[\sqrt{n^2-(k_f\,R_1)^2}+\sqrt{\nu^2-(k_f\,R_2)^2}-\sqrt{(n+\nu)^2-(k_f\,R_1+k_f\,R_2)^2}\left(1-\frac{(k_f\,R_1+k_f\,R_2)\delta}{(n+\nu)^2-(k_f\,R_1+k_f\,R_2)^2}\right)\right]} \quad (7.12)$$

Since we are analyzing the terms along the line of maximum we can replace ν by $(n)(R_2/R_1)$. Expr. 7.12 then reduces to:

$$e^{\sqrt{n^2-(k_f\,R_1)^2}\left[1+\frac{k_fR_2}{k_fR_1}-\left(1+\frac{k_fR_2}{k_fR_1}\right)\left(1-\frac{(k_f\,R_1)^2\delta}{(n^2-(k_fR_1)^2)(k_fR_1+k_fR_2)}\right)\right]} \quad (7.13)$$

which further simplifies to:

$$e^{\left[\frac{(k_f\,R_1)\delta}{\sqrt{(n^2-(k_fR_1)^2)}}\right]} \quad (7.14)$$

Now consider the other term given in Expr. 6.34. Using the Taylor series expansion

$$(n+\nu)\,\cosh^{-1}\left(\frac{n+\nu}{k_fR_1+k_fR_2+\delta}\right) \approx (n+\nu)\,\cosh^{-1}\left(\frac{n+\nu}{k_fR_1+k_fR_2}\right) - \frac{(n+\nu)^2\delta}{(k_fR_1+k_fR_2)\sqrt{(n+\nu)^2-(k_fR_1+k_fR_2)^2}} \quad (7.15)$$

and a similar analysis along the line of maximum by replacing ν with $n(R_2/R_1)$ reduces Expr. 6.34 to:

$$e^{\left[-\frac{\delta}{\sqrt{n^2-(k_f\,R_1)^2}}\left(\frac{n^2}{k_fR_1}\right)\right]} \quad (7.16)$$

Combining Expr. 7.14 and 7.16 gives:

$$e^{\left[-\frac{\delta}{\sqrt{n^2-(k_f\,R_1)^2}}\left(\frac{n^2}{k_fR_1}-k_fR_1\right)\right]} \quad (7.17)$$

From this we infer that the values becomes negligibly small when:

$$\frac{\delta}{\sqrt{n^2-(k_f\,R_1)^2}}\left(\frac{n^2}{k_fR_1}-k_fR_1\right) \gg 1 \quad (7.18)$$

i.e if

$$n \gg \sqrt{\left(\frac{R_1}{d}\right)^2+(k_fR_1)^2} \quad (7.19)$$

and since $\nu = (n)(R_2/R_1)$ the condition for ν would be:

$$\nu \gg \frac{R_2}{R_1}\sqrt{\left(\frac{R_1}{d}\right)^2 + (k_f R_1)^2} \tag{7.20}$$

This condition is similar to the criterion for the convergence of the vector spherical wave expansion method of the near-field radiative transfer between two spheres which was shown in Section 7.3 to be of the form:

$$N_{conv} = 2\frac{R_2}{d} + e\pi\frac{D}{\lambda}, \tag{7.21}$$

This criterion was derived heuristically based on comparison with the convergence criterion for the near-field radiative transfer between planar bodies. Eq. 7.20 demonstrates explicitly the role of translation coefficients in attaining convergence of near-field radiative transfer calculations between two spheres. For our numerical calculations we have used Eq. 7.21 as the criterion for the number of vector spherical waves since it is typically of higher value than that represented in Eq. 7.20.

7.6 Conclusion

In this chapter, the numerical convergence of vector spherical wave expansion technique applied to near–field electromagnetic scattering has been investigated. The conclusions of this study are as follows:

1. The number of vector spherical waves required for numerical convergence of near–field radiative thermal conductance between two closely spaced spheres of equal size that support surface polaritons is given by $N_{conv} = C\frac{R}{d} + e\pi\frac{D}{\lambda}$, where C is a dimensionless number that depends on the desired accuracy.

2. Contributions from larger values of m decay exponentially with m and the summation over m can be truncated at a value of $m = M_{conv} \ll N_{conv}$.

3. The convergence criteria developed here are also applicable to other near–field scattering problems where a new length scale is introduced in lieu of d. For example, to

determine the LDOS at a point at a distance $z(\ll \lambda)$ from the surface of a sphere, the convergence criterion would be $N_{conv} = C\frac{R}{z} + e\pi\frac{D}{\lambda}$,

Chapter 8

Near-field conductance

8.1 Introduction

The changes to the numerical implementation of the theory of radiative transfer between two spheres that were described in Chapters 4, 5 and 6 have lead to the following improvements: (a) While gaps up to $d/R = 0.01$ for *equal* sized spheres is available in literature [36], this work extends to gaps up to $d/R = 0.001$ (b) Extension to lower gaps has lead to better understanding of near-field effects between two spheres and thus enabled us to better model the effect of curvature on near–field radiative transfer between spherical bodies. (c) It has also been possible to extend the computational analysis to a more general case of unequal sized spheres up to the limit $R_2 \gg R_1$ where R_2 and R_1 are the radii of the two sphere. Without the simplifications I have introduced, these calculations become infeasible due to computational demand. In this chapter the results from the computation of near-field radiative transfer between two spheres are presented and analyzed.

8.2 Computation of thermal radiative conductance

The radiative heat transfer is analyzed in terms of the linearized thermal conductance G (WK^{-1}) which has been defined earlier in Chapter 3. This reads as:

$$G = \lim_{T_1 \to T_2} \frac{Q(T_1, T_2)}{T_1 - T_2}, \qquad \text{(3.34 revisited)}$$

where $Q(T_1, T_2)$ is the rate of heat transfer between the two spheres at temperatures T_1 and T_2. The derivation of an expression for G in terms of the dyadic Green's function of the two-sphere configuration (which is computed using the vector spherical wave expansion method) has been explained in detail in Chapter 3. The expression for G used for computational purposes is given by Eq. 3.39. All computations have been conducted at 300 K.

For experimental validation of the enhancement of radiative transfer in the near-field, silica has been the material of choice for two reasons: (1) it can support surface phonon–polaritons in the frequency ranges from 0.055 to 0.07 eV and 0.114 to 0.16 eV, and (2) silica microspheres are easily available. Hence the heat transfer has been computed, using silica as the material, for the frequency range 0.041 eV to 0.16 eV. The optical properties of silica are taken from Ref. 20.

8.3 Discussion of results

8.3.1 Equal sized spheres

For the configuration of two equal spheres which has been shown in the inset of Fig. 8.1, numerical values of conductance are plotted as a function of gap to radius ratio d/R for different radii in Fig. 8.1. In Fig. 8.1, for every radius, two regions can be observed: (1) a region where conductance varies logarithmically (marked Region–A), and (2) a region where a deviation from logarithmic behavior is observed (marked Region–B).

To gain a deeper insight into this behavior, we compare the spectral variation of the conductance at different gaps in the two regions. The gaps chosen are $d/R = 0.01$, 0.03 and 0.05 for $R = 20$ μm (marked (a), (b) and (c) in Fig. 8.1). The gaps corresponding to $d/R = 0.03$, 0.05 fall in Region–A of Fig. 8.1, while $d/R = 0.01$ falls in Region–B. From the spectral variation plotted in Fig. 7.1, we note that most of the increase in the heat transfer for $d/R = 0.01$ is due to the contributions from surface phonon–polaritons alone. Hence we conclude that the contribution from surface phonon–polaritons to the conductance starts to become significant in Region–B.

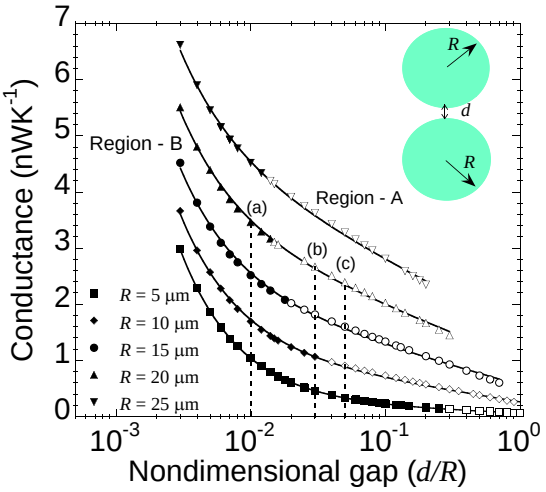

Figure 8.1: Conductance between the two spheres shown in the top right corner as a function of d/R for different radii. The open circles denote the conductance values which show a logarithmic variation with gap (marked Region–A) and the closed circles denote the conductance values which show a deviation from logarithmic behavior (marked Region–B). The spectral variation of the conductance at gaps marked (a), (b) and (c) for $R = 20$ μm spheres are shown in Fig. 8.2.

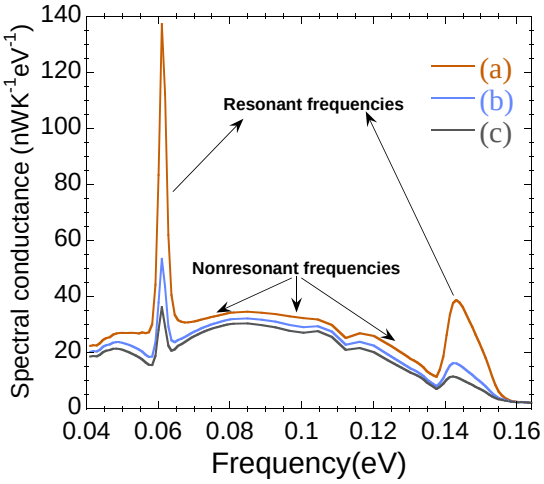

Figure 8.2: The spectral variation of conductance for $R = 20\,\mu$m for the different gaps (a), (b) and (c) marked in Fig. 8.1. The frequency regions marked "Resonant frequencies" ("Nonresonant frequencies") are where surface phonon–polaritons are present (absent).

The observation that contribution from surface phonon–polaritons to the conductance starts to become significant in Region–B necessitates us to understand the contribution from surface phonon–polaritons better. To this end, the contributions of conductance from the resonant and nonresonant frequencies are analyzed separately and are shown in Fig. 8.3. Remarkably, the analysis for the spectral conductance at a resonant frequency (0.061 eV) suggests that at gaps $d/R \lesssim 0.01$, the conductance is dependent only on the ratio d/R and is independent of the particular values of d and R. Furthermore, the slope of the data points being ≈ -1 suggests a R/d behavior at such gaps. A similar analysis for a nonresonant frequency (0.1005 eV), shown in the inset of Fig. 8.3, suggests that for $d/R \lesssim 0.01$ the rate of change of spectral conductance with gap is significantly lower than that for resonant frequencies.

Based on the behavior of resonant radiative transfer at small gaps and the observation of logarithmic behavior for larger gaps in Fig. 8.1, we have found that the numerical values of conductance can be modeled by a function of the form $C_1\,(R/d) + C_2 \ln(R/d) + C_3$, where

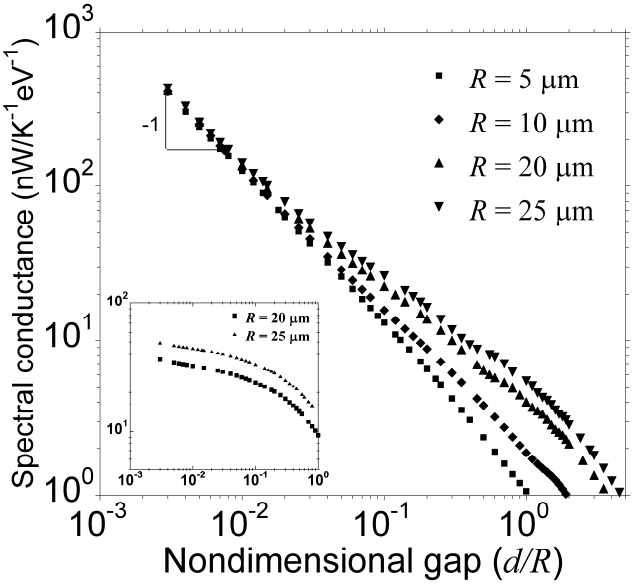

Figure 8.3: For different radii, the spectral conductance at a resonant frequency (0.061 eV) as a function of d/R. The conductance values for all radii attain a slope of -1 at low gaps. Inset: The spectral conductance at a nonresonant frequency (0.1005 eV) as a function of d/R (axes labels remain the same).

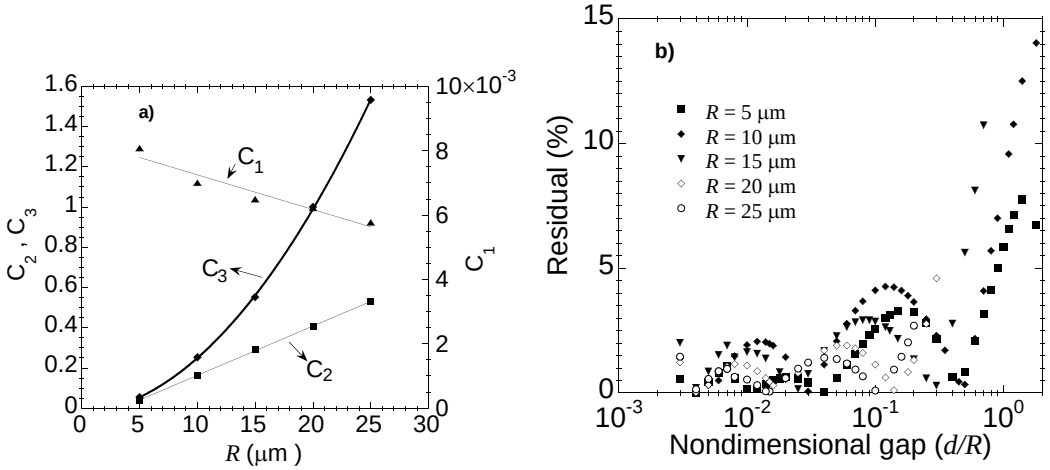

Figure 8.4: **(a)** Variation of the coefficients C_1, C_2 and C_3 with radius. **(b)** The residual for the curves plotted as a percentage of the conductance values.

C_1, C_2 and C_3 are radius–dependent constants. C_1, C_2 and C_3 are obtained by minimizing the square of error between the function and the numerical values of conductance. The fitted curves are shown in Fig. 8.1. The variation of C_1, C_2 and C_3 with radius is shown in Fig. 8.4(a). The equations of the curves used for fitting the values of the coefficients are given by: $C_1 = 8.33 - 0.11R$; $C_2 = -0.08 + 0.025R$; $C_3 = -0.024 + 0.004R + 0.002R^2$. The above equations can be made use of to calculate the conductances for intermediate radii. The residuals from the functional fit to the numerical conductance values are shown in Fig. 8.4(b). The residual is calculated as the difference between the numerical values and the values from the functional form and expressed as percentage of the numerical values.

8.4 Comparison between Classical Radiative Transfer Theory and Numerically obtained Conductance Values.

The expression for radiative conductance $G_c(d,T)$, according to the classical radiative transfer theory (RTT), between two objects of equal emissivity ϵ and surface area A is given by [87]:

$$G_c(d,T) = \frac{4\sigma A T^3}{2(1-\epsilon)/\epsilon + (1/F_{12})} \tag{8.1}$$

where F_{12} is the view factor between the two objects. Since the conductance between the two spheres has been simulated for a particular frequency range, for effective comparison, conductance from classical theory has to be computed for this frequency range too. Hence Eq. 8.1 needs to be modified to:

$$G_c(d,T) = \frac{4\sigma A T^3 \left(f\left(\lambda_2 T\right) - f\left(\lambda_1 T\right)\right)}{2(1-\epsilon)/\epsilon + (1/F_{12})} \tag{8.2}$$

where λ_1 and λ_2 are the two wavelengths between which the numerical simulation in this work has been performed ($\lambda_2 > \lambda_1$) and $f(\lambda T)$ is given by [1]:

$$f(\lambda T) = \frac{\int_0^{\lambda} \frac{\partial e_b(\lambda, T)}{\partial T}\, d\lambda}{\int_0^{\infty} \frac{\partial e_b(\lambda, T)}{\partial T}\, d\lambda} \tag{8.3}$$

where $e_b(\lambda, T)$ denotes the spectral hemispherical blackbody flux given by:

$$e_b(\lambda, T) = \frac{A_1}{\lambda^5 \left(\exp\left(\frac{A_2}{\lambda T}\right) - 1\right)} \tag{8.4}$$

with $A_1 = 4\pi^2\hbar c^2$ ($\approx 37,413$ Wμm^{4}cm^{-2}) and $A_2 = 2\pi\hbar c/k_B$ ($\approx 14,388$ μmK). In our simulations, the conductance between the two spheres has been computed for the wavelength range 7.57 μm (0.164 eV) to 30.3 μm (0.041 eV). For this range, $f(\lambda_2 T) - f(\lambda_1 T) = 0.721$. The comparison between conductance values determined from Eq. 8.2 and the numerically computed conductance values for $R = 20$ μm is shown in Fig. 8.5. The conductance values from RTT and numerical simulations follow a similar trend at large gaps ($1 \lesssim d/R \lesssim 10$). Even though view factor calculations are strictly valid only when the nominal size of objects are much larger than the characteristic thermal wavelength λ_T, it appears that they are valid for silica spheres as small as $R = 20\,\mu$m. The small deviations (less than 10 % at $d/R = 10$) between the numerical values and the predictions from RTT are possibly due to: (1) diffraction effects, (2) numerical errors due to finite number of frequency points used for the computation, and (3) non-validity of RTT for such small spheres.

8.4.1 Unequal sized spheres

By making use of the behavior of the normalized translation coefficients with varying radius ratios it is possible to compute the near-field radiative conductance between two spheres with large size disparities since, as explained in Chapter 6, for large radius ratios of the spheres only the elements in the first few rows ($\approx R_1/d$) of the translation coefficients are dominant. Hence only these need to be computed and utilized thereof. By making use of this simplification, radiative conductance G between two spheres for radius ratio 10, 20 and 40 has been computed and shown in Figure 8.6.

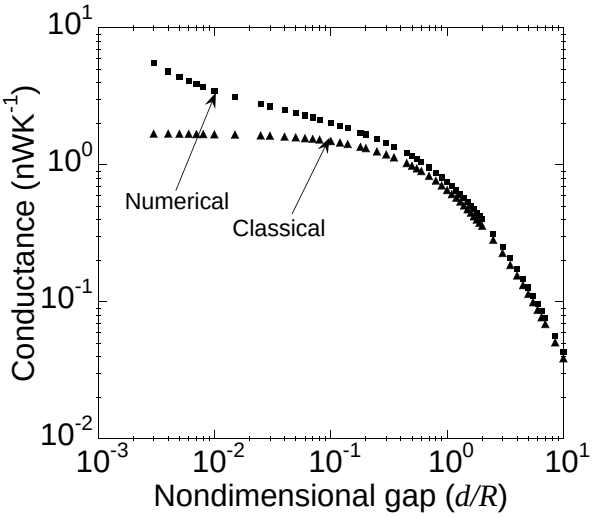

Figure 8.5: Comparison between the conductance values that are predicted using the classical radiative heat transfer with numerical data for $R = 20$ μm spheres.

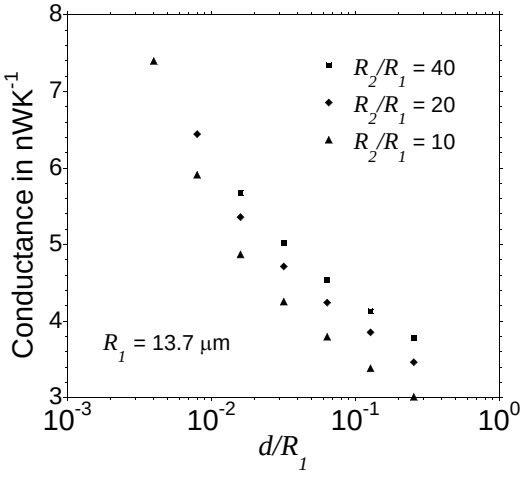

Figure 8.6: Variation of total conductance between two unequal sized spheres of varying radius ratio as a function of the non-dimensional gap d/R_1. The radius of the smaller sphere R_1 is kept constant at 13.7 μm

Further analysis of the radiative conductance between unequal sized spheres is presented in the next chapter in the context of proximity approximation method.

8.5 Conclusion

In summary, radiative heat transfer between two spheres has been analyzed in the near–field regime using flucutational electrodynamics formalism. We have shown that it varies as R/d as $d/R \to 0$ and as $\log(R/d)$ for larger values of d/R up to the far–field limit. The conductance values from unequal sized spheres was also presented for size ratios 10, 20 and 40.

Chapter 9

Modified proximity approximation

9.1 Introduction

While the results discussed in the Chapter 8 were obtained from first principles by taking into account the origin of radiative transfer from thermoelectric fluctuations in the material, it suffers from the disadvantage that the computational resources pose a limit on the closest gap between the two spheres that can be analyzed (notice from Eq. 7.21 in Chapter 7 that the number of vector spherical waves required for convergence $N_{max} \propto 1/d$ where d is the surface to surface gap at the point of closest approach). The computational method developed is also particular to the configuration of two spheres with centers translated along the z-axis and cannot be extended easily for computing near-field radiative transfer between objects of other geometrical shapes (like cylinders, cones or ellipsoids). In this chapter a discussion of an approximate method to compute the near-field radiative transfer between curved bodies has been provided which can be used for predicting near-field radiative transfer between bodies of arbitrary geometrical shape, and at much smaller gaps than possible from exact computations. This method, known as proximity approximation method, has been used in literature for predicting near-field *forces* between closely spaced curved bodies. We discuss the reasons why this theory has to be modified for radiative transfer theory and compare the computed values of near-field radiative conductance for both equal and unequal sized

spheres with the prediction from the modified form of proximity approximation theory.

9.2 Discussion

9.2.1 Features of proximity approximation theory

The importance of proximity approximation originates from the fact that it provides us with a facile way of approximating the interaction between two bodies with arbitrary curvature at small gaps by making use of the corresponding interaction between two infinite flat surfaces. This proximity approximation method (also called Derjaguin's approximation) was first proposed in 1934 by Derjaguin [88] while discussing interaction between colloidal particles, and has since been employed to estimate near-field forces, like van der Waals and Casimir force [89; 90; 91; 92; 93; 94], between closely spaced curved bodies. Some of the features of this proximity approximation method (as applicable for estimating near-field forces) has been listed below:

1. It can be applied to bodies with arbitrary curvature as has been shown by White [95]

2. It provides a first-order approximation for the force between the curved objects [95; 96]

3. It is applicable to not just the additive inverse power law potentials like the van der Waals/ Casimir interactions but for any type of functional form, whether attractive, repulsive or oscillatory [97, pg. 163], [96]

4. It is valid only when the interaction length and the minimum separation distance between the particles is much smaller than the curvature i.e for this approximation to be valid the interaction between the particles should only be in a small region around the point of closest approach [95; 98; 96; 89].

From Feature 4 listed above, if L_0 is the length scale over which the interaction reduces to zero, R_0 the minimum radius of curvature of the system, and d the minimum separation

between the two bodies at the point of closest approach, then we can write the sufficient conditions for the proximity approximation to be valid as [95]

$$\frac{L_0}{R_0} \ll 1; \tag{9.1}$$

and

$$\frac{d}{R_0} \ll 1 \tag{9.2}$$

There have been attempts to estimate the error from adopting the proximity approximation to predict near-field forces between the experimentally feasible geometry of sphere and a plate. Gies et al. [89] applied worldline numerics to this configuration to calculate the Casimir energy from scalar field in vacuum with Dirichlet boundary conditions. They determined that the proximity approximation is accurate up to 1% error when $d/R \leq 0.00755$. Here, d is the minimum separation distance between the sphere and the plate and R is the radius of the sphere. Fosco et al. [99], by expanding the electrostatic energy using a gradient expansion in the local separation between the surfaces, determined that the proximity approximation gives accurate values up to 1% for $d/R \lesssim 0.017$ for estimating the electrostatic forces between the sphere and the plane. Teo et al. [100] compared the proximity approximation results with numerical calculations of the Casimir energy from the electromagnetic field in vacuum between a sphere and a plate and determined that the proximity approximation gives accurate results up to a accuracy of 5% for $d/R \lesssim 0.03$ and up to 1% error for $d/R \lesssim 0.006$. Identical figures were also arrived at by Bimonte et al. [101], who used a similar gradient expansion technique proposed by Fosco et al. [99], to arrive at an expression for the Casimir energy from electromagnetic field in vacuum. There has also been at attempt to determine the accuracy of the proximity approximation experimentally. Krause et al. [102] measured the Casimir force between a gold-coated plate and gold-coated spheres of varying radii, ranging from 10.5 μm to 148.2 μm and determined that the error at 95% confidence level due to the proximity approximation will be less than 1% when $d/R \lesssim 0.017$. This confidence level was determined only for gaps $d \lesssim 300$ nm.

To illustrate the application of proximity approximation, consider two bodies with arbitrary curvature separated by a gap d at the point of closest approach as shown in Fig. 9.1.

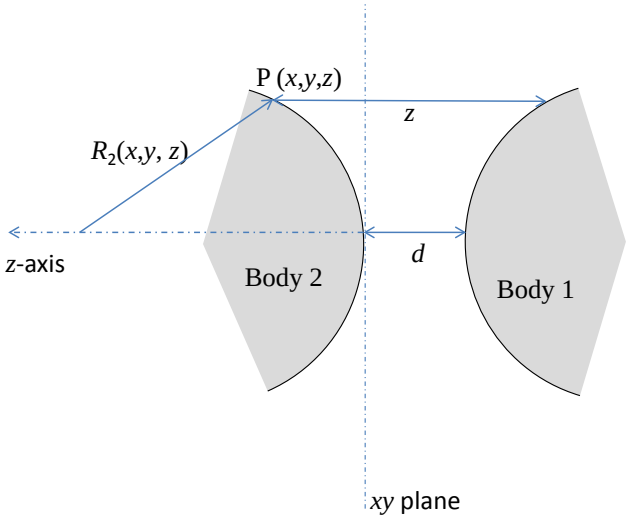

Figure 9.1: Interaction between two bodies separated by a gap d at the point of closest approach

The bodies are assumed to be smooth in the vicinity of the the point of closest approach. Consider an element area dS at the point $P(x, y, z)$ on the surface of body 2. *Provided that the radius of curvature of the two bodies is large compared to the distance d*, then the element area dS can be approximated to be an element area of a half-space with the same properties as body 2, parallel to and separated by a second half-space with properties of body 1 by a distance z. In such a scenario the interaction energy of the element area dS with body 1, dV, can be written as

$$dV = E(z)\, dS \tag{9.3}$$

where, $E(z)$ is the interaction energy per unit area between the two half-spaces separated by a gap z. It must be noted that $E(z)$ must decay rapidly with distance z so that contributions from area elements far-away from the point of closest approach is minimal and Eq. 9.3 is valid. The total interaction energy between the two bodies can then be written as:

$$V = \int_{S_1} E(z) dS \tag{9.4}$$

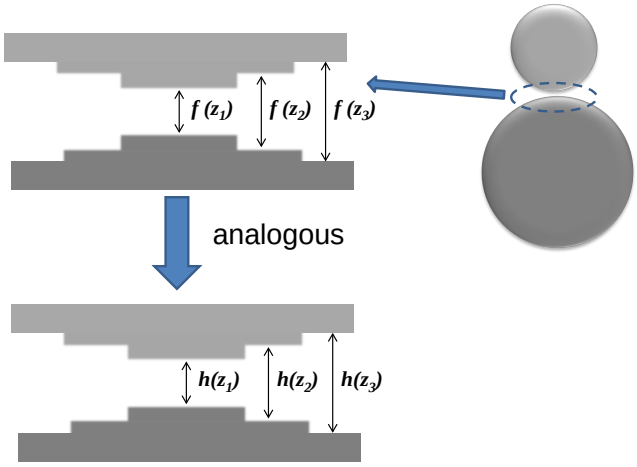

Figure 9.2: Extension of proximity approximation in Casimir theory to approximating the near-field radiative heat transfer between two spheres. $f(z)$ denotes the Casmir/van der Waals pressure between two plates with gap z and $h(z)$ is the radiative heat transfer coefficient between two plates with gap z

The area element can to a leading order of the *inverse of radius of curvature* (= 0 for planar surfaces) be replaced by the projected area on the xy plane to give:

$$V = \int_x \int_y E(z)\, dx\, dy \tag{9.5}$$

9.2.2 Application of proximity approximation to near-field radiative transfer

Because of similarity in the origin of near-field forces and the near-field radiative transfer (both are induced by the fluctuation of charges inside bodies at finite temperature) a similar technique has been extended to the case of estimating near-field radiative heat transfer between curved bodies [20; 36], i.e radiative conductance (defined in Eq. 3.34) between curved surfaces can be estimated from the known solutions for near–field radiative transfer coefficient between parallel surfaces using the proximity approximation, as has been depicted (for the configuration of two spheres) in Fig. 9.2.

Analytically, this is equivalent to:

$$G(d,T) = \int_0^R h(z)\, 2\pi r\, dr, \tag{9.6}$$

where $z = d + 2R - 2\sqrt{R^2 - r^2}$ is the local gap between the two spheres as shown in Fig. 9.3(b) and $h(z)$ is the heat transfer coefficient between two parallel surfaces at that gap z. This form has been used by Rousseau et al. [20] to compare with experimental observations. $h(z)$ for two flat silica surfaces is plotted as a function of gap z in Fig. 9.3(a). $h(z)$ can be split as follows:

$$h\,(z) = h_{nf}\,(z) + h_\infty, \tag{9.7}$$

where h_∞ is the contribution from propagating waves and h_{nf} contains contributions from all other effects. In other words Eq. 9.7 indicates that $h(z)$ has contributions from both the near–field effects and from propagating waves, and thus includes all contributions to radiative heat transfer. As can be seen from Fig. 9.3(a), h_{nf} falls off rapidly to zero as z increases beyond λ_T and h_∞ attains a constant value for $z \gg \lambda_T$.

Measurements from the Chen group [18; 19] between a silica microsphere and a silica substrate in the range 30 nm to 10 μm did not agree with the proximity approximation. Rousseau et al. [20], based on their measurements between a silica microsphere and a silica substrate, concluded that near–field radiative transfer agreed with the proximity approximation in the range 30 nm to 2.5 μm. There are no experiments between two silica spheres reported in literature. Though the phenomena of van der Waals force (including Casimir force) and near–field radiative transfer are fluctuation–induced, there are important differences. Radiative transfer has contributions from the infra–red (IR) portion of the electromagnetic spectrum whereas forces have larger contributions from the visible and higher frequencies. Dispersion forces obey a power law behavior and decay rapidly to zero as gap between the interacting bodies increases, while radiative transfer has a finite value due to propagating waves at large gaps too. Because of these differences, it is not clear whether the proximity approximation, as it is used to compute dispersion forces, can be used to predict near–field radiative heat transfer between spherical surfaces.

Recently, a higher order expansion of the proximity approximation method to estimate better the near-field radiative heat transfer between two bodies has been proposed [103]. This method is similar to the gradient expansion in the local gap z of the electrostatic and Casimir energy [99; 101] used to arrive at higher order expansion of the proximity approximation method for estimating the near-field forces. However, the results in Ref. [103] were presented under the assumption that the radiative heat transfer between two half-spaces varies as $1/z^2$. This assumption is valid only in the interaction region where the local gap between arbitrary shaped bodies is small.

To understand why we can expect the proximity approximation, as given in Eq. 9.6, to fail to predict accurately the radiative heat transfer between finite objects, observe that in Fig. 9.3(a), $h_{nf} \gg h_\infty$ is satisfied only for gaps $z \lesssim 400$ nm. For sizes of spheres currently used in experiments ($R \gtrsim 5$ μm) there will be significant contribution from the propagating waves at the outer regions of the spheres where the local gap $z \gtrsim \lambda_T$ even when the minimum gap at the point of closest approach $d \ll \lambda_T$. This suggests that for gaps under consideration in Region–B of Fig. 8.1 in Chapter 8 there will be contributions to the radiative transfer *from propagating waves as well as near–field effects*. While Eq. 9.6 might provide a reasonable approximation to the contribution from near–field effects to the radiative transfer, it overestimates the contribution from propagating waves at the outer regions of the spheres. To see this, consider the large–gap limit where the heat transfer coefficient $h(z)$ from Eq. 9.7 attains a constant value, h_∞. Eq. 9.6 predicts conductance between the spheres to be $\pi R^2 h_\infty$, irrespective of the gap and does not take into account the variation of view factor [87] between the two spheres with distance. It must be pointed out, however, that for the configuration adopted in Ref. [20] the view factor does not change with gap between the sphere and the plane.

In order to preserve the continuity between the radiative transfer in the large–gap limit and the smaller gaps, we propose that the proximity approximation, in the form that is used to determine Casimir or van der Waals forces between spherical surfaces, be used to predict only the contribution to conductance from h_{nf}. The contribution from propagating

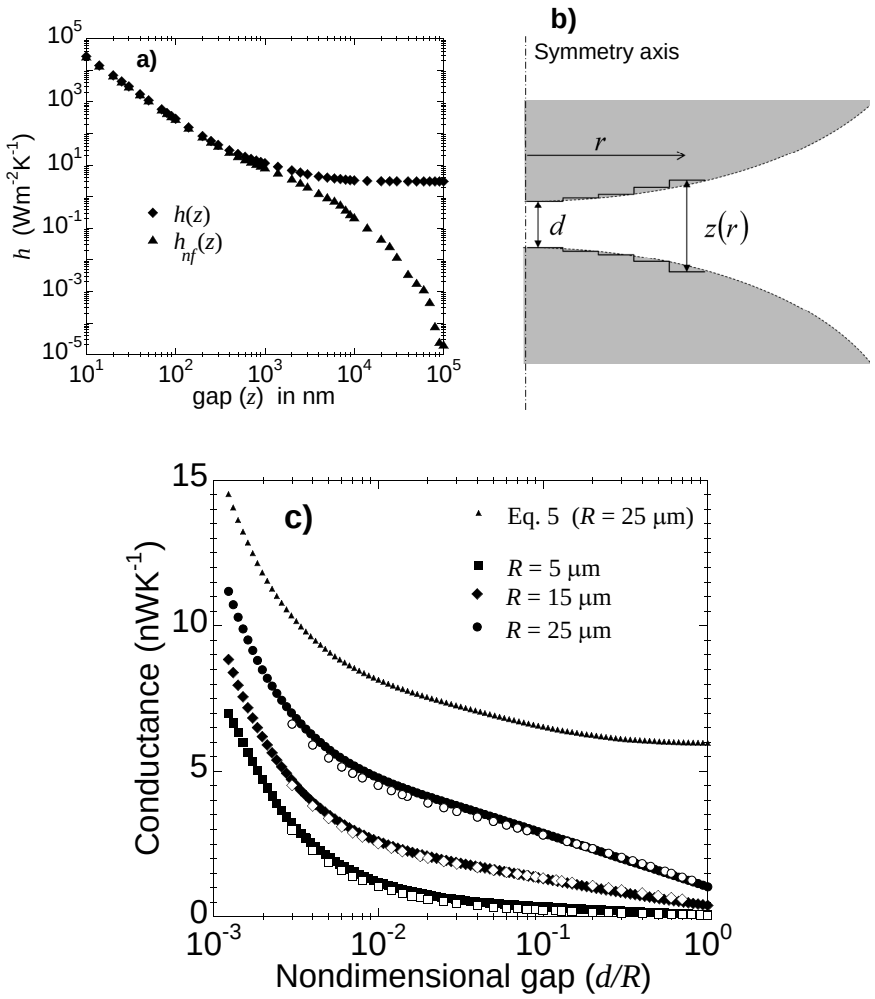

Figure 9.3: **(a)** Variation of $h(z)$ and $h_{nf}(z)$ with gap between two flat silica surfaces. **(b)** Proximity approximation – the conductance between two spheres is calculated by summing the local contributions of the heat transfer coefficient between two parallel planes. **(c)** Comparison between the conductance values obtained numerically and using proximity approximation. The open circles denote the numerical values while the closed circles denote the proximity approximation predictions using Eq. 9.8. Proximity approximation using Eq. 9.6 for $R = 25$ μm has been included for comparison.

waves to the near–field conductance is computed according to RTT by taking into account the variation of view factor with distance between the two spheres. This correction to the proximity approximation formulation is not necessary while calculating Casimir or van der Waals force, since they decay rapidly with distance ($1/d^4$ and $1/d^3$ respectively). The modified form of proximity approximation (MPA) to determine the conductance between two equal sized spheres is given by:

$$G_1^{\mathrm{MPA}}(d,T) = \int_0^R h_{nf}(z) 2\pi r \, dr \; + \; G_c^{(1)}(d,T), \tag{9.8}$$

where $G_c^{(1)}(d,T)$ can be approximated by the conductance value from classical radiative transfer theory when diffraction effects are negligible. $G_c^{(1)}(d,T)$ for two objects of equal emissivity ϵ and surface area A is given by Eq. 8.1 (repeated here for convenience):

$$G_c^{(1)}(d,T) = \frac{4\sigma A T^3}{2(1-\epsilon)/\epsilon + (1/F_{12})}; \tag{8.1 revisited}$$

where F_{12} is the view factor between the two objects. Conductance values computed using Eq. 9.8 and Eq. 8.1 are in greater agreement with the numerically computed values than the prediction of Eq. 9.6 as shown in Fig. 9.3(c). Numerical values of the gap dependent view factor between the two spheres is taken from Ref. [55]. Since the conductance between the two spheres has been simulated for a particular frequency range, for effective comparison, conductance from classical theory has to be properly adjusted to reflect this, as explained in Section 8.3 of Chapter 8.

9.3 Verification of modified proximity approximation for spheres with large size disparities

The MPA was first developed to ensure continuity in the radiative transfer between two equal sized spheres in the far-field and the near-field limits as explained in Section 9.2. Hence it would be of interest to also study the relevance of the MPA when the radius of one of the spheres R_2 is increased such that $R_2 \gg R_1$ where R_1 is the radius of the smaller sphere,

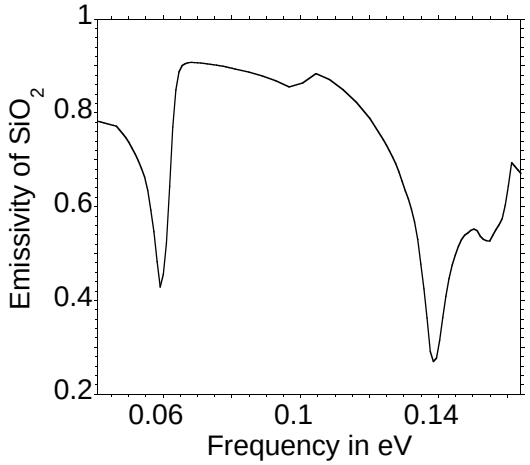

Figure 9.4: The plot of spectral emissivity for a silica half-plane as a function of frequency in eV which is used in the form of MPA (Eq. 9.9) to predict the far-field contribution to the conductance

since when $R_2/R_1 \to \infty$ it reduces to the sphere-plane configuration that has been commonly adopted for experimental verification.

The form of MPA for *unequal sized spheres* is given by:

$$G_2^{\mathrm{MPA}}(d,T) = \int_0^{R_1} h_{nf}(z)\, 2\pi r\, dr \; + \; G_c^{(2)}(d,T), \tag{9.9}$$

where R_1 is the radius of the smaller sphere, $z = d + R_1 + R_2 - \sqrt{R_1^2 - r^2} - \sqrt{R_2^2 - r^2}$ is the gap at distance r from the symmetry axis as shown in Fig. 9.3(b). $G_c^{(2)}(d,T)$ for two unequal spheres of equal emissivity ϵ and temperature T is given by [87]:

$$G_c^{(2)}(d,T) = \frac{4\sigma T^3\,(4\pi R_1^2)}{((1-\epsilon)/\epsilon)\,(1 + R_1^2/R_2^2) + (1/F_{12})}, \tag{9.10}$$

where F_{12} is the gap dependent view factor between the two spheres [104]. The emissivity for a silica half-space has been computed and plotted as a function of frequency in eV in Fig. 9.4(b). The conductance values have been computed for the frequency range 0.041 eV to 0.164 eV, and the value of $G_c^{(2)}(d,T)$ has been appropriately adjusted to reflect this.

The predicted conductance from MPA, G_2^{MPA}, from Eq. 9.9 is compared with exact computations developed from first-principles, G, (Sec. 8.3 of Chapter 8) in Fig. 9.5(a) for

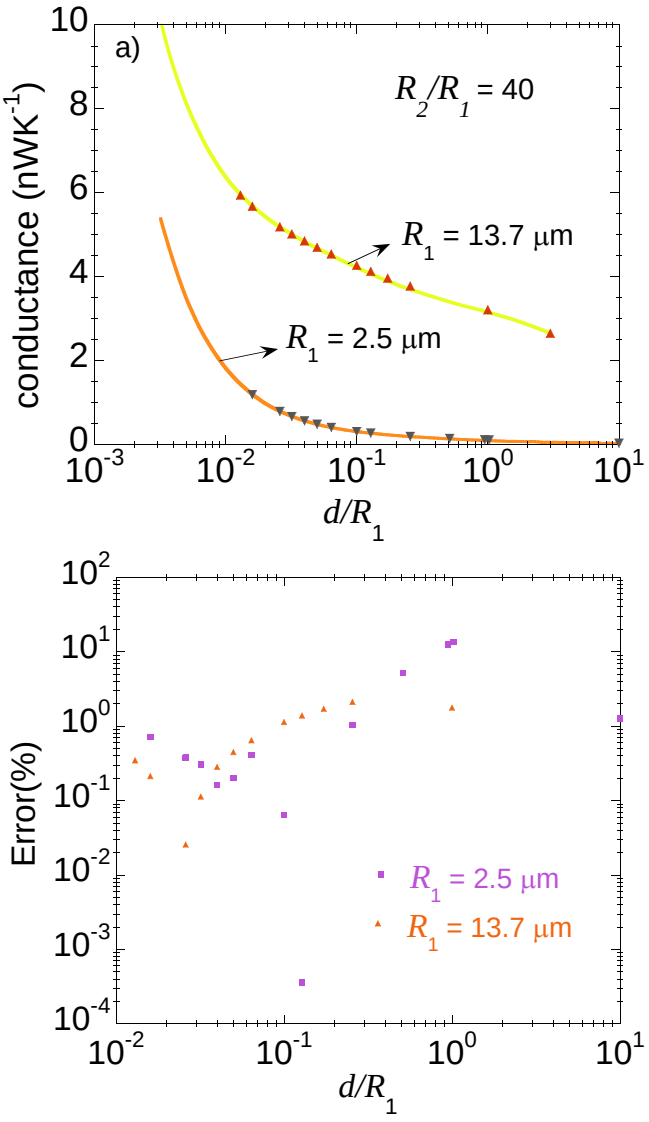

Figure 9.5: (a) Plot of computed values of the total conductance and the MPA as a function of the non-dimensional gap d/R_1 for two spheres with $R_2/R_1 = 40$. The study has been performed for $R_1 = 13.7$ μm and 2.5 μm (b) The % error between the computed values and values from the MPA as a function of d/R_1

two spheres with $R_1 = 13.7\ \mu$m and $2.5\,\mu$m and $R_2 = 40R_1$. The error between G and G^{MPA} is plotted in Fig. 9.5(b). For gaps $d/R_1 < 0.1$ MPA is observed to be able to predict the exact computed values of the conductance with errors less than 1%.

Since the total radiative conductance between the two spheres has contribution from frequencies, where there is a resonant enhancement from surface phonon polaritons as well as non-resonant frequencies where radiative conductance is not due to surface phonon polaritons (see Fig. 7.1 in Chapter 8), it would be of interest to observe if the MPA accurately predicts the contribution from both these regions. The computed values of the spectral conductance G_ω at a single resonant (0.061 eV) and a non-resonant (0.081 eV) frequency and the values predicted by the MPA for these frequencies have been plotted in Fig. 9.6(a) and Fig. 9.7(a). The contribution from the far-field radiative conductance $G_c(d,T)$ in Eq. 9.9 has to be appropriately modified to reflect spectral conductance. From proximity approximation theory, at gaps $d/R_1 \approx 0$, the spectral conductance $G_\omega(d)$ for two spheres of unequal radii R_1 and R_2 is expected to vary as [105]:

$$G_\omega(d) = \left(\frac{R_1 R_2}{R_1 + R_2}\right)\frac{1}{d} \approx \frac{R_1}{d}\ (\text{for } R_2 \gg R_1) \tag{9.11}$$

Since $R_2 \gg R_1$ (here $R_2 = 40R_1$) this characteristic R_1/d behavior is observed for the resonant frequency contributions shown in Fig. 9.6(a) for $d/R_1 \lesssim 0.02$. However such behavior is not observed for the non-resonant frequency contributions shown in Fig. 9.7(a).

The error between G_ω and the spectral conductance predicted by MPA, G_ω^{MPA}, for the resonant and non-resonant frequency contributions are shown in Fig. 9.6(b) and Fig. 9.6(b). In the far-field region ($d/R_1 \gtrsim 2$ for $R_1 = 13.7\,\mu$m, and $d/R_1 \gtrsim 10$ for $R_1 = 2.5\,\mu$m) where the enhancement due to tunneling of waves (surface waves at the resonant frequency and evanescent waves at non-resonant frequency) is negligible, the form of MPA in Eq. 9.9 predicts that the variation in G_ω with gap is primarily due to the changing view factor between the spheres with gap. As observed from Fig. 9.6(b) and Fig. 9.7(b) there is good agreement with the exact computed values of the conductance at such gaps. For intermediate gaps ($2 \lesssim d/R_1 \lesssim 0.07$, for $R_1 = 13.7\,\mu$m) the variation of G_ω with gap is dependent on both the changing view factor with gap as well as increased tunneling of waves. For gaps

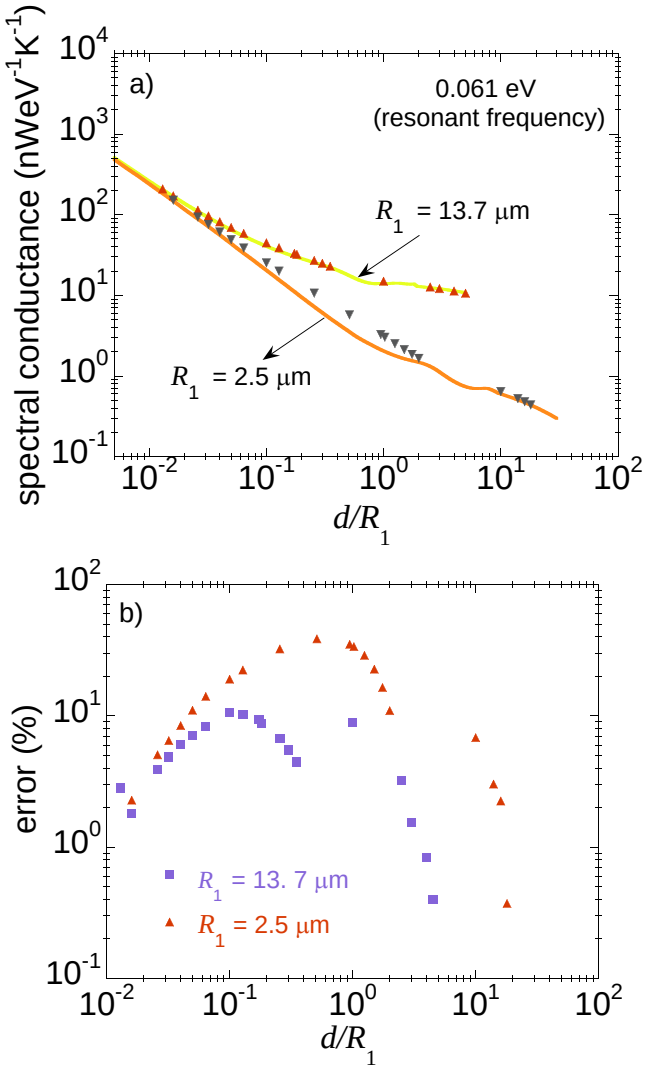

Figure 9.6: (a) Comparison between the computed values of G_ω at a resonant frequency (0.061 eV) and G_ω^{MPA} as a function of the non-dimensional gap d/R_1 for two spheres of radius $R_1 = 2.5$ μm, 13.7 μm and $R_2 = 40R_1$ (b) The % error between G_ω and G_ω^{MPA} as a function of d/R_1

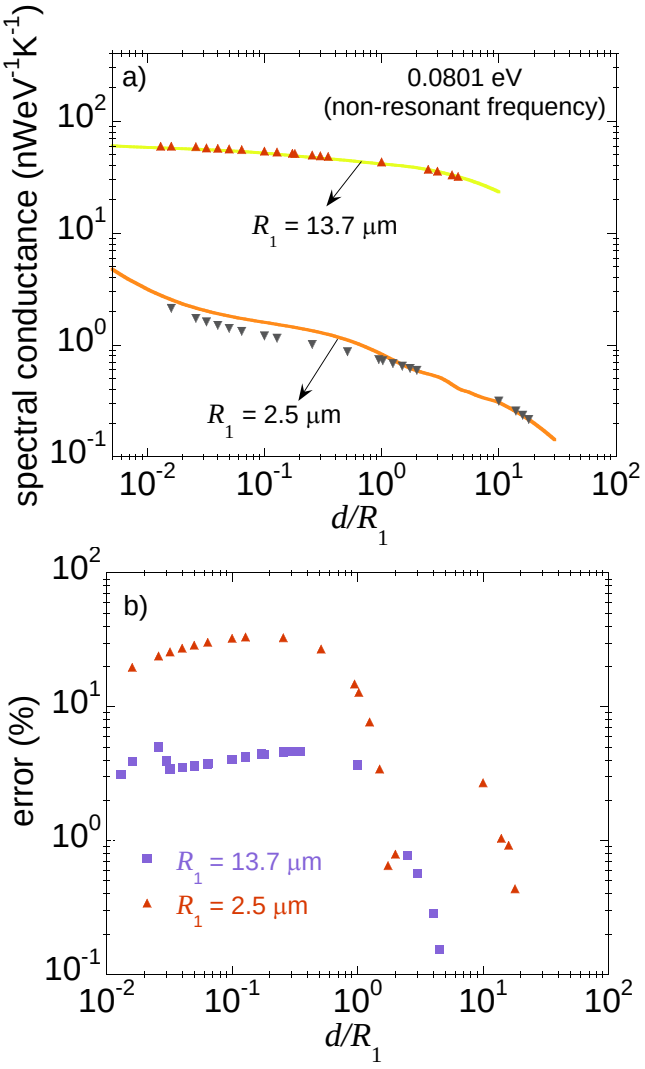

Figure 9.7: (a) Comparison between the computed values of G_ω at a non-resonant frequency (0.0801 eV) and G_ω^{MPA} as a function of the non-dimensional gap d/R_1 for two spheres of radius $R_1 = 2.5\ \mu$m, $13.7\,\mu$m and $R_2 = 40R_1$ (b) The % error between G_ω and G_ω^{MPA} as a function of d/R_1

$d/R_1 \lesssim 0.07$ (below which the view factor increases by less than 1%) the enhanced radiative transfer with decreasing gap can be attributed entirely due to increased tunneling of waves. At such small gaps MPA is able to model the enhancement at the resonant frequency within $\approx$ 5% errors irrespective of the value of R_1, whereas at the non-resonant frequency the error is observed to be greater than 10% when $R_1 = 2.5\,\mu$m. Despite such high errors at the non-resonant frequencies, MPA is successful in predicting the overall conductance when $R_1 = 2.5\ \mu$m with error less than 1% for $d/R_1 \lesssim 0.1$ as observed in Fig. 9.5. This apparent discrepancy is explained in detail in Sec. 9.4.

9.4 Validation of modified proximity approximation with experimental results

In this section, both the predictions from MPA and the exact computed values are compared with experimental measurements of near-field radiative transfer between a sphere and a plane available in literature [106]. Since at the gaps used for experiments the change in radiative conductance is mainly due to near-field effects and not due to changing view factors, the exact computed values as well as the predictions from MPA should be appropriately modified to reflect this. The form of the MPA that is appropriate for comparing with the near-field enhancement in radiative transfer for the sphere-plane case would be:

$$G^{\mathrm{MPA}}(d,T) = \int_0^R h_{nf}(z)\, 2\pi r\, dr \tag{9.12}$$

where R is the radius of the sphere and $z = d + R - \sqrt{R^2 - r^2}$. The experimental measurements between a sphere and a planar substrate can be compared with the exact computations of radiative transfer between unequal sized spheres only if the size ratio between the two spheres is such that $R_2 \gg R_1$. The following paragraph expands on this observation.

First consider the variation of conductance, $G(d)$, with non-dimensional gap d/R_1 where R_1 is the radius of the smaller sphere (in this case $R_1 = 13.7\ \mu$m) for varying values of R_2/R_1 (radius ratio) as shown in Figure 9.8(a). From these values of $G(d)$, variation of $G(d) - G(d_{max})$ for $d_{max} = 2364.5$ nm (which is the gap below which the enhanced radiative

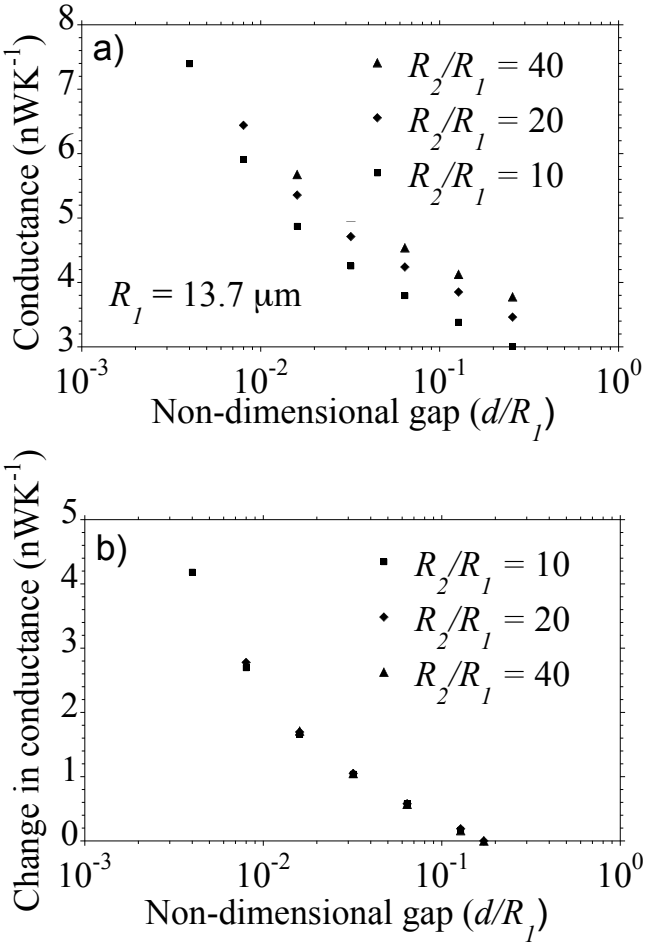

Figure 9.8: Near-field conductance between two spheres of varying R_2/R_1 as a function of non-dimensional gap d/R_1. (a) Conductance $G(d)$ between a sphere $R_1 = 13.7$ μm and another sphere of radius R_2 such that $R_2/R_1 = 10$, 20, and 40. (b) Change in conductance, $G(d) - G(d_{max})$, where $d_{max} = 2364.5$ nm.

transfer due to near-field effects can be experimentally measured) with non-dimensional gap d/R_1 gives us the near-field enhancement due to near-field effects for small gaps. This is shown in Fig. 9.8(b). The values are observed to change by less than 0.5 % on increasing the radius ratio from 20 to 40. Thus we can conclude that though the conductance between the two spheres is not identical to the conductance between a sphere and a plane, the change in near-field radiative transfer with gap (which is what we are measuring experimentally) is identical as long as $R_2 \gtrsim 20R_1$. In the simulations, we have set $R_2 = 40R_1$ ($R_1 = 2.5$ μm or 13.76 μm).

The discussion in the above paragraph paves the way for comparison of both the MPA and the exact computed values of conductance between two unequal size spheres with the experimental measurements of near-field enhancement in radiative transfer between a sphere and a plane. This is shown in Fig. 9.9(a) and (b) where the following quantities are compared: (a) $G_{th}^{ex}(d) - G_{th}^{ex}(d_{max})$ (subscript th stands for *theory* and ex stands for *exact*) denotes the conductance from exact computations between two unequal sized spheres with $R_1 = 2.5\,\mu$m or $13.7\,\mu$m and $R_2 = 40\,R_1$ (b) $G_{th}^{\mathrm{MPA}}(d)$ which denotes the predictions from MPA and (c) G_{expt} which denotes the conductance obtained from experimental measurements between a silica sphere of radius $R = 2.5\,\mu$m or $R = 13.7\,\mu$m and a planar silica substrate (the experimental readings were taken by my colleague Ning Gu. More details about the experimental technique can be found in Ref. [106]). Excellent conformation is observed between the three quantities. The predictions from MPA (Eq. 9.12) for the sphere-plane configuration can be further compared with the values of $G_{th}^{ex}(d) - G_{th}^{ex}(d_{max})$ from Fig. 9.9 by comparing the error between the two approximations. This is shown in Figure 9.10 where the variation of fractional difference between the values $G(d) - G(d_{max})$ and the MPA, with non-dimensional gap d/R_1 for $R_2/R_1 = 40$ is shown for both $R_1 = 2.5$ μm and $R_1 = 13.7$ μm. For $d/R_1 < 0.1$ the error between the two quantities is less than 5%.

To understand why the modified proximity approximation seems to explain experimental data even when $R_1 < \lambda_T$, we plot in Fig. 9.11 [106] $\Delta G_{th}^{ex}(\omega, d) = G_{th}^{ex}(\omega, d) - G_{th}^{ex}(\omega, d_{max})$ i.e the spectral contributions to the change in conductance at d from that at $d_{max} = 2364.5$

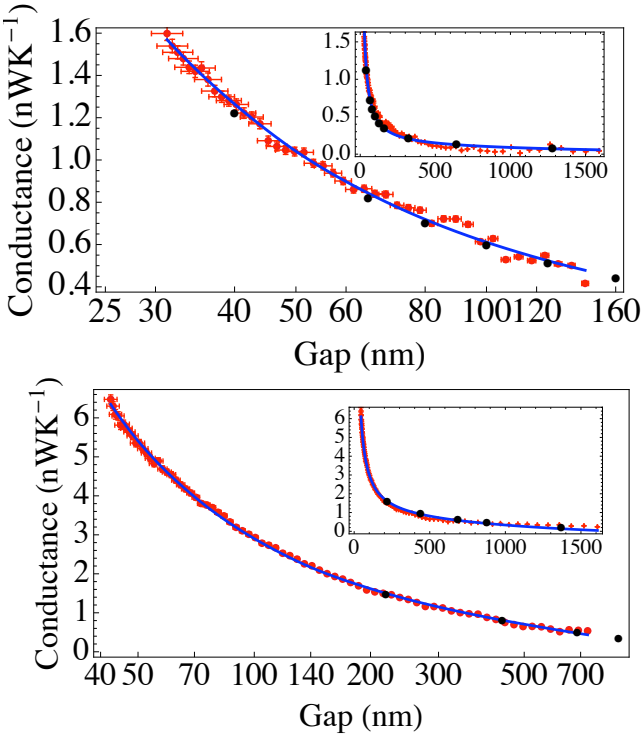

Figure 9.9: Conductance as a function of separation d for the $R = 2.5$ μm and $R = 13.76$ μm spheres are shown in (a) and (b) respectively (red points with error bars). Only the data for $d/R \lesssim 0.05$ is shown in the main figures. The entire data up to $d = 1500$ nm is shown in the inset. The thick blue line is obtained from applying the modified proximity approximation to the near-field contribution to radiative transfer between two half planes. The black circles are obtained from exact calculations.

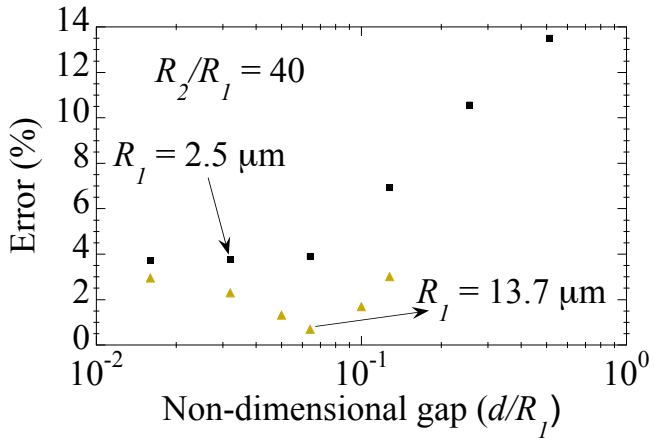

Figure 9.10: Near-field conductance between two spheres of varying radius ratios (R_2/R_1) as a function of non-dimensional gap d/R_1

nm for $R_1 = 2.5$ μm (Fig. 9.11a) and $R_1 = 13.7$ μm (Fig. 9.11b). Surface phonon polariton resonances are responsible for the two prominent features between 0.052 eV - 0.072 eV and between 0.1335 eV - 0.16 eV in the spectrum of $\Delta G_{th}^{ex}(\omega, d)$. At rest of the frequencies, the enhancement is non-resonant, i.e. it is not due to surface phonon polaritons. Though it can be concluded qualitatively from the behavior of $\Delta G_{th}^{ex}(\omega, d)$ that resonant frequencies contribute more to $\Delta G_{th}^{ex}(d)$ for the smaller sphere, a better way to quantify it is by plotting $\overline{\Delta G}_{th}^{ex}(\omega, d) = \int_0^{\omega} \Delta G_{th}^{ex}(\omega', d)d\omega' / \int_0^{\infty} \Delta G_{th}^{ex}(\omega', d)d\omega'$, the normalized cumulative spectral contribution to $\Delta G_{th}^{ex}(d)$, as we have done in the insets in Fig. 9.11a and Fig. 9.11b. Over the entire frequency range, surface phonon polariton resonances contribute to ≈ 90 % and ≈ 60 % for $R_1 = 2.5$ μm and $R_1 = 13.76$ μm spheres respectively. Our analysis has shown that the error in $G(\omega, d) - G(\omega, d_{max})$ between the exact numerical calculations and the modified proximity approximation: (1) is smaller at resonant frequencies compared to non-resonant frequencies, and (2) decreases as R_1 increases (See Fig. 3c). The reason modified proximity approximation is valid even when $R_1 < \lambda_T$ is because the increase in error with decreasing R_1 is balanced by the relatively higher contribution from resonant frequencies.

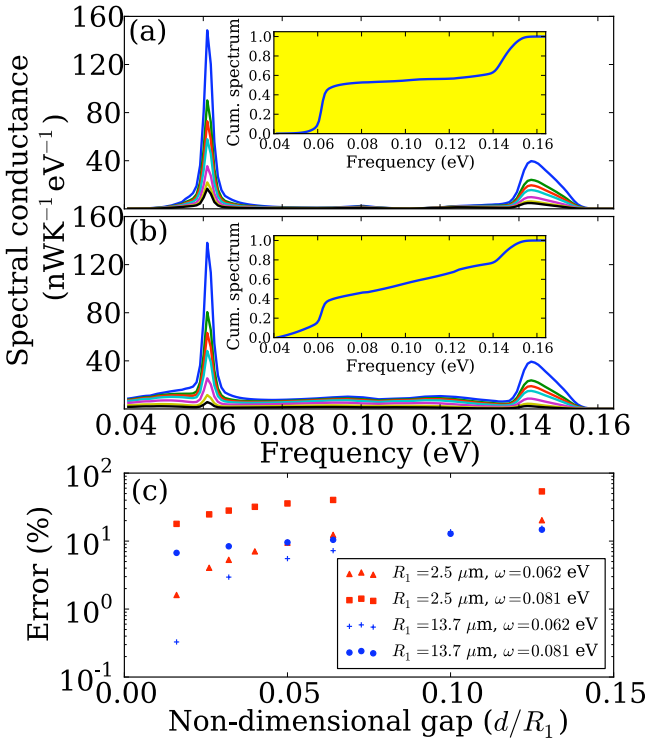

Figure 9.11: Exact numerical prediction for $\Delta G_{th}^{ex}(\omega, d) = G_{th}^{ex}(\omega, d) - G_{th}^{ex}(\omega, d_{max})$ for $d_{max} = 2364.5$ nm . (a) $R_1 = 2.5$ μm, $R_2 = 40R_1$, and (b) $R_1 = 13.76$ μm, $R_2 = 40R_1$. The lines in (a) and (b) correspond to $d/R_1 = 0.016$ (blue line), 0.026 (green), 0.032 (red), 0.04 (cyan), 0.064 (magenta), 0.1 (yellow), and 0.128 (black). The normalized cumulative spectral contribution, $\overline{\Delta G}(\omega, d)$, for $d/R_1 = 0.016$ is shown in the inset to (a) and (b). (c) Error between exact calculation and modified proximity approximation at $\omega = 0.062$ eV (resonant frequency) and $\omega = 0.081$ eV (non-resonant frequency).

9.5 Conclusion

We have also shown that the proximity theorem, in the form that is used to compute dispersive forces cannot be used to determine near–field heat transfer and a modification is needed to take into account the contributions from propagating waves. We have also shown the predictive capability of the modified form of proximity approximation for the more general configuration of unequal sized spheres with large size disparities as well. We have validated the predictions of this modified proximity approximation (MPA) with experimental values available in literature for the sphere-plane configuration. We have also provided a reason for the validity of MPA for the case of sub-wavelength spheres. Such predictive capabilities will be useful in applications like heat–assisted magnetic recording [107] to approximate the near–field radiative transfer between the curved surface of the near–field transducer and the recording medium.

Chapter 10

Summary and future work

10.1 Summary of the main contributions

The primary aim of this work was to understand the effect of curvature on near-field radiative transfer. To this end, I have listed below some of the contributions from this work.

1. The computational model for computing the near-field radiative transfer between two spheres was simplified which enabled us to probe lower gaps than available in literature for the case of two equal sized spheres. While gaps till $d/R = 0.01$ are available in literature, we have now been able to go down till gaps of $d/R = 0.001$ (R being the radius of the spheres and d the surface to surface gap). Based on these computations at lower gaps we were able to show that the contribution to radiative heat transfer from frequencies where the surface phonon polaritons are active varies as R/d as $d/R \to 0$

2. A modified form of proximity approximation theory has been proposed for the case of radiative exchange between two equal sized spheres to ensure continuity condition between far-field and near-field radiative transfer between finite objects.

3. A simplified form of translation addition theorem valid for general near-field electromagnetic scattering problems has been proposed. And the limit at which this form is valid is discussed. The recursion relations for computing the translation coefficients

using this simplified form of translation addition theorem is computationally faster (about 10 times faster) than using the recursion relations for the exact forms

4. A general formula was derived for finding the number of terms required for attaining convergence in the computation of near-field radiative heat transfer via vector spherical wave expansion method. This was expressed in terms of the spatial parameters in the configuration like the radius of the spheres, the surface to surface gap, and the wavelength of radiation.

5. Based on the observed dependence of the normalized translation coefficient on the radius ratio of the two spheres, the near-field radiative transfer between unequal sized spheres with large size disparities has also been computed. For radius ratio $R_2/R_1 = 40$ it has been possible to go down till a gap of $d/R_1 = 0.013$. For any radius ratio R_2/R_1, it is possible to compute radiative heat transfer for gaps until $d/R_1 \approx (R_2/R_1)/3000$. The relevance of the modified proximity approximation has been shown for this more general case as well.

6. The accuracy of the modified proximity approximation method for different frequencies has also been analyzed and the reason why this method is seen to hold true for the case of sub-wavelength spheres has been explained. This method has also been validated by comparing with experimental results available in literature.

10.2 Future work

1. The theoretical method outlined to compute the near-field radiative transfer between two spheres assumes that the surfaces are smooth. However, in practice, experimental measurements of near-field radiative transfer is influenced by surface effects like surface roughness characteristics. Since the scale of the roughness in commercially available silica spheres is roughly the same order as the minimum gap we go down to, the effect of roughness in the measured radiative transfer is expected to be significant. Hence corrections to the measured radiative heat transfer should be arrived at to take into

account the influence of surface roughness. The influence of roughness on the near-field heat transfer between two planar surfaces has been studied by using second-order perturbation theory [108]. However no such study has been undertaken for the case of curved bodies.

2. It would be of interest to know if we can find an exact analytical expression for the radiative heat transfer between two spheres in the asymptotic limit of $d \to 0$, where d is the the separation distance between the two spheres at the point of closest approach. In this limit the vector translation coefficients can be shown to reduce to simple expressions with the contributions from higher order modes reaching a constant value. Perhaps this can be made use of to arrive at an analytical expression for the near-field radiative heat transfer between two spheres.

3. The modified proximity approximation was first proposed in this work for the configuration of two equal sized spheres separated by a small gap. This was later shown to hold true for a more general case of two unequal sized spheres with large size disparities. The validity of MPA can be further tested with curved surfaces other than spherical surfaces, for e.g. cylindrical, conical or ellipsoidal surfaces.

Part III

Bibliography

Bibliography

[1] M. Brewster, *Thermal radiative transfer and properties*. Wiley-Interscience, 1992.

[2] S. M. Rytov, *Theory of Electric Fluctuations and Thermal Radiation*. Bedford, MA: Air Force Cambridge Research Center, 1959.

[3] A. Everest, "Kirchhoff-gustav robert 1824-1887," *Physics Education*, vol. 4, no. 6, p. 341, 1969.

[4] J. Stefan, *Über die Beziehung zwischen der Wärmestrahlung und der Temperatur*. Sitzungsberichte der mathematisch-naturwissenschaftlichen Classe der kaiserlichen Akademie der Wissenschaften, Bd. 79 (1879), S. 391-428., 1879.

[5] M. Planck, "On the law of distribution of energy in the normal spectrum," *Annalen der Physik*, vol. 4, no. 553, p. 1, 1901.

[6] L. Hu, A. Narayanaswamy, X. Chen, and G. Chen, "Near-field thermal radiation between two closely spaced glass plates exceeding plancks blackbody radiation law," *Applied Physics Letters*, vol. 92, no. 13, pp. 133106–133106, 2008.

[7] S. Shen, A. Narayanaswamy, and G. Chen, "Surface phonon polaritons mediated energy transfer between nanoscale gaps," *Nano Letters*, vol. 9, no. 8, pp. 2909 – 2913, 2009.

[8] A. N. A. Narayanaswamy, S. Shen, L. Hu, X. Chen, and G. Chen, "Breakdown of the planck blackbody radiation law at nanoscale breakdown of the planck blackbody radiation law at nanoscale gaps," *Appl. Phys. A*, vol. 96, pp. 357–362, 2009.

[9] W. Challener, C. Peng, A. Itagi, D. Karns, W. Peng, Y. Peng, X. Yang, X. Zhu, N. Gokemeijer, Y.-T. Hsia, *et al.*, "Heat-assisted magnetic recording by a near-field transducer with efficient optical energy transfer," *Nature Photonics*, vol. 3, no. 4, pp. 220–224, 2009.

[10] A. Kittel, W. Muller-Hirsch, J. Parisi, S.-A. Biehs, D. Reddig, and M. Holthaus, "Near-field heat transfer in a scanning thermal microscope," *Phys. Rev. Lett.*, vol. 95, p. 224301, 2005.

[11] G. Domoto, R. Boehm, and C. Tien, "Experimental investigation of radiative transfer between metallic surfaces at cryogenic temperatures," vol. 92, pp. 412–417, 1970.

[12] C. Hargreaves, "Radiative transfer between closely spaced bodies," *Philips Res. Rep. Suppl.*, vol. 5, pp. 1–80, 1973.

[13] R. Ottens, V. Quetschke, S. Wise, A. Alemi, R. Lundock, G. Mueller, D. Reitze, D. Tanner, and B. Whiting, "Near-field radiative heat transfer between macroscopic planar surfaces," *Physical Review Letters*, vol. 107, no. 1, p. 014301, 2011.

[14] T. Kralik, P. Hanzelka, M. Zobac, V. Musilova, T. Fort, and M. Horak, "Strong near-field enhancement of radiative heat transfer between metallic surfaces," *Physical review letters*, vol. 109, no. 22, p. 224302, 2012.

[15] W. Müller-Hirsch, A. Kraft, M. T. Hirsch, J. Parisi, and A. Kittel, "Heat transfer in ultrahigh vacuum scanning thermal microscopy," vol. 17, pp. 1205–1210, 1999.

[16] A. Kittel, U. Wischnath, J. Welker, O. Huth, F. Rüting, and S.-A. Biehs, "Near-field thermal imaging of nanostructured surfaces," *Applied Physics Letters*, vol. 93, p. 193109, 2008.

[17] L. Worbes, D. Hellmann, and A. Kittel, "Enhanced near-field heat flow of a monolayer dielectric island," *Physical review letters*, vol. 110, no. 13, p. 134302, 2013.

[18] A. Narayanaswamy, S. Shen, and G. Chen, "Near–field radiative heat transfer between a sphere and a substrate," *Phys. Rev. B*, vol. 78, p. 115303, 2008.

[19] S. Shen, A. Narayanaswamy, and G. Chen, "Surface phonon polaritons mediated energy transfer between nanoscale gaps," *Nano Lett.*, vol. 9, pp. 2909–2913, 2009.

[20] E. Rousseau, A. Siria, G. Jourdan, S. Volz, F. Comin, J. Chevrier, and J.-J. Greffet, "Radiative heat transfer at the nanoscale," *Nat. Photonics*, vol. 3, pp. 514–517, 2009.

[21] S. Shen, A. Mavrokefalos, P. Sambegoro, and G. Chen, "Nanoscale thermal radiation between two gold surfaces," *Applied Physics Letters*, vol. 100, no. 23, pp. 233114–233114, 2012.

[22] P. van Zwol, L. Ranno, and J. Chevrier, "Tuning near field radiative heat flux through surface excitations with a metal insulator transition," *Physical Review Letters*, vol. 108, no. 23, p. 234301, 2012.

[23] E. G. Cravalho, C. L. Tien, and R. P. Caren, "Effect of small spacings on radiative transfer between two dielectrics," vol. 89, pp. 351–358, 1967.

[24] D. Polder and M. Van Hove, "Theory of radiative heat transfer between closely spaced bodies," *Phys. Rev. B*, vol. 4, pp. 3303–3314, 1971.

[25] J. J. Loomis and H. J. Maris, "Theory of heat transfer by evanescent electromagnetic waves," *Phs. Rev. B*, vol. 50, p. 18517, 1994.

[26] J.-P. Mulet, K. Joulain, R. Carminati, and J.-J. Greffet, "Enhanced radiative transfer at nanometric distances," *Microscale Thermophys. Eng.*, vol. 6, pp. 209–222, 2002.

[27] K. Joulain, J. Drevillon, and P. Ben-Abdallah, "Noncontact heat transfer between two metamaterials," *Physical Review B*, vol. 81, no. 16, p. 165119, 2010.

[28] S. J. Petersen, S. Basu, and M. Francoeur, "Near-field thermal emission from metamaterials," *Photonics and Nanostructures-Fundamentals and Applications*, 2013.

[29] S.-A. Biehs, P. Ben-Abdallah, F. S. Rosa, K. Joulain, J.-J. Greffet, *et al.*, "Nanoscale heat flux between nanoporous materials," *Optics express*, vol. 19, no. S5, pp. A1088–A1103, 2011.

[30] S.-A. Biehs, F. S. Rosa, and P. Ben-Abdallah, "Modulation of near-field heat transfer between two gratings," *Applied Physics Letters*, vol. 98, no. 24, pp. 243102–243102, 2011.

[31] S.-A. Biehs and J.-J. Greffet, "Influence of roughness on near-field heat transfer between two plates," *Physical Review B*, vol. 82, no. 24, p. 245410, 2010.

[32] A. I. Volokitin and B. N. J. Persson, "Radiative heat transfer between nanostructures," *Physical Review B*, vol. 63, p. 205404, 2001.

[33] G. Domingues, S. Volz, K. Joulain, and J.-J. Greffet, "Heat transfer between two nanoparticles through near-field interaction," *Phys. Rev. Lett.*, vol. 94, no. 8, pp. 085901 –, 2005. Nanoparticles;Near field interactions;Thermal conductance;Coulomb interactions;.

[34] J. Pendry, "Radiative exchange of heat between nanostructures," *Journal of Physics: Condensed Matter*, vol. 11, p. 6621, 1999.

[35] J.-P. Mulet, K. Joulain, R. Carminati, and J.-J. Greffet, "Nanoscale radiative heat transfer between a small particle and a plane surface," *Appl. Phys. Lett.*, vol. 78, pp. 2931–2933, 2001.

[36] A. Narayanaswamy and G. Chen, "Thermal near-field radiative transfer between two spheres," *Physical Review B*, vol. 77, no. 7, p. 075125, 2008.

[37] C. Otey and S. Fan, "Numerically exact calculation of electromagnetic heat transfer between a dielectric sphere and plate," *Phys. Rev. B*, vol. 84, p. 245431, 2011.

[38] M. Krüger, T. Emig, and M. Kardar, "Nonequilibrium electromagnetic fluctuations: Heat transfer and interactions," *Physical Review Letters*, vol. 106, no. 21, p. 210404, 2011.

[39] P. Ben-Abdallah, S.-A. Biehs, and K. Joulain, "Many-body radiative heat transfer theory," *Physical Review Letters*, vol. 107, no. 11, p. 114301, 2011.

[40] R. Messina and M. Antezza, "Scattering-matrix approach to casimir-lifshitz force and heat transfer out of thermal equilibrium between arbitrary bodies," *Physical Review A*, vol. 84, no. 4, p. 042102, 2011.

[41] A. W. Rodriguez, M. H. Reid, and S. G. Johnson, "Fluctuating-surface-current formulation of radiative heat transfer for arbitrary geometries," *Physical Review B*, vol. 86, no. 22, p. 220302, 2012.

[42] A. Narayanaswamy and Y. Zheng, "A green's function formalism of energy and momentum transfer in fluctuational electrodynamics," *Journal of Quantitative Spectroscopy and Radiative Transfer*, 2013.

[43] A. Narayanaswamy and G. Chen, "Surface modes for near field thermophotovoltaics," *Appl. Phys. Lett.*, vol. 82, pp. 3544–3546, 2003.

[44] S. Basu, Z. Zhang, and C. Fu, "Review of near-field thermal radiation and its application to energy conversion," *International Journal of Energy Research*, vol. 33, no. 13, pp. 1203–1232, 2009.

[45] O. Ilic, M. Jablan, J. D. Joannopoulos, I. Celanovic, and M. Soljačić, "Overcoming the black body limit in plasmonic and graphene near-field thermophotovoltaic systems," *Optics express*, vol. 20, no. 103, pp. A366–A384, 2012.

[46] M. Laroche, R. Carminati, and J.-J. Greffet, "Near-field thermophotovoltaic energy conversion," *Journal of Applied Physics*, vol. 100, no. 6, pp. 063704–063704, 2006.

[47] C. R. Otey, W. T. Lau, and S. Fan, "Thermal rectification through vacuum," *Phys. Rev. Lett*, vol. 104, no. 15, p. 154301, 2010.

[48] B. Lee, Y.-B. Chen, and Z. Zhang, "Confinement of infrared radiation to nanometer scales through metallic slit arrays," *Journal of Quantitative Spectroscopy and Radiative Transfer*, vol. 109, no. 4, pp. 608–619, 2008.

[49] Y. De Wilde, F. Formanek, R. Carminati, B. Gralak, P.-A. Lemoine, K. Joulain, J.-P. Mulet, Y. Chen, and J.-J. Greffet, "Thermal radiation scanning tunnelling microscopy," *Nature*, vol. 444, no. 7120, pp. 740–743, 2006.

[50] B. Guha, C. Otey, C. B. Poitras, S. Fan, and M. Lipson, "Near-field radiative cooling of nanostructures," *Nano letters*, vol. 12, no. 9, pp. 4546–4550, 2012.

[51] W. Chew, "A derivation of the vector addition theorem," *Microwave and Optical Technology Letters*, vol. 3, no. 7, pp. 256–260, 1990.

[52] C. F. Bohren and D. R. Huffman, *Absorption and Scattering of Light by Small Particles*. Wiley-Interscience, 1998.

[53] J. H. Bruning and Y. Lo, "Multiple scattering by spheres," Tech. Rep. Antenna Laboratory Report No. 69-5, University of Illinois, Urbana, Illinois, 1969.

[54] N. W. Ashcroft and N. D. Mermin, "Solid state physics (holt," *Rinehart and Winston, New York*, vol. 19761, 1976.

[55] E. Palik, *Handbook of Optical Constants of Solids,*. Academic Press, 1985.

[56] M. A. Ordal, R. J. Bell, R. Alexander Jr, L. Long, M. Querry, *et al.*, "Optical properties of fourteen metals in the infrared and far infrared: Al, co, cu, au, fe, pb, mo, ni, pd, pt, ag, ti, v, and w.," *Applied Optics*, vol. 24, no. 24, pp. 4493–4499, 1985.

[57] D. L. Mills and E. Burnstein, "Polaritons: The electromagnetic modes of media," *Rep. Prog. Phys.*, vol. 37, pp. 817–926, 1974.

[58] *Near-field radiative transfer: Thermal radiation, thermophotovoltaic power generation and optical characterization.* PhD thesis.

[59] R. E. Collin, *Field theory of guided waves*, vol. 2. IEEE press New York, 1991.

[60] C. Lin and L. A. Segel, *Mathematics Applied to Deterministic Problems.* SIAM, 1974.

[61] W. C. Chew, *Waves and Fields in Inhomogeneous Media.* Piscataway, NJ: IEEE Press, 1995.

[62] H. Levine and J. Schwinger, "On the theory of electromagnetic wave diffraction by an aperture in an infinite plane conducting screen," *Communications on Pure and Applied Mathematics*, vol. 3, no. 4, pp. 355–391, 1950.

[63] L. Tsang, J. A. Kong, and K. H. Ding, *Scattering of Electromagnetic Waves.* Wiley, 2000.

[64] J. A. Kong, *Electromagnetic Wave Theory.* EMW, 2000.

[65] C.-T. Tai, *Dyadic Green functions in electromagnetic theory*, vol. 272. IEEE press New York, 1994.

[66] H. Nyquist, "Thermal agitation of electric charge in conductors," *Physical review*, vol. 32, no. 1, pp. 110–113, 1928.

[67] H. B. Callen and T. A. Welton, "Irreversibility and generalized noise," *Physical Review*, vol. 83, no. 1, pp. 34–40, 1951.

[68] S. Rytov, "Theory of electrical fluctuations and thermal radiation, ussr academy of sciences, moscow (1953); english translation by us air force cambridge research center, bedford, massachusetts, rept. no," tech. rep., AFCRC-TR-59-162, 1959.

[69] L. D. Landau, E. M. Lifshitz, and L. P. Pitaevskii, *Electrodynamics of Continuous Media.* Pergamon Press, 1984.

[70] L. Landau and E. Lifshitz, *Statistical Physics, Part 1 (Vol. 5, Landau and Lifschitz Course of Theoretical Physics), translated by JB Sykes and MJ Kearsley.* Pergamon Press, New York, 1980.

[71] J.-P. Mulet, K. Joulain, R. Carminati, and J.-J. Greffet, "Enhanced radiative heat transfer at nanometric distances," vol. 6, pp. 209–222, 2002.

[72] J. E. Sipe, "New green-function formalism for surface optics," *JOSA B*, vol. 4, no. 4, pp. 481–489, 1987.

[73] W. C. Chew, "Efficient ways to compute the vector addition theorem," *J. of Electromagnet. Wave*, vol. 7, pp. 651–665, 1993.

[74] M. Abramowitz and I. Stegun, *Handbook of Mathematical Functions: With Formulas, Graphs, and Mathematical Tables.* New York: Dover Publications, 1965.

[75] W. C. Chew, "Derivation of the vector addition theorem," *Microwave and Optical Technology Letters*, vol. 3, pp. 256 – 260, 1990.

[76] W. C. Chew, "Recurrence relations for three-dimensional scalar addition theorem," *J. of Electromagnet. Wave*, vol. 6, pp. 133–142, 1992.

[77] A. Cuyt, *Handbook of continued fractions for special functions.* Springer, 2008.

[78] E. Rothwell, "Computation of the logarithm of bessel functions of complex argument," *Communications in numerical methods in engineering*, vol. 21, no. 10, pp. 597–605, 2005.

[79] K. T. Kim, *Symmetry Relations of the Translation Coefficients of the Spherical Scalar and Vector Multipole Fields*, vol. 48 of *Progress In Electromagnetic Research*, ch. 3, pp. 45–66. EMW Publishing, 2004.

[80] W. Wiscombe, "Mie scattering calculations: advances in technique and fast, vector-speed computer codes," tech. rep., NCAR Technical Note, 1996.

[81] W. Chew, E. Michielssen, J. Song, and J. Jin, *Fast and efficient algorithms in computational electromagnetics*. Artech House, Inc., 2001.

[82] N. A. Gumerov and R. Duraiswami, "Computation of scattering from n spheres using multipole reexpansion," *J. Acoust. Soc. Am.*, vol. 112, pp. 2688 – 2701, 2002.

[83] M. Quinten, A. Pack, and R. Wannemacher, "Scattering and extinction of evanescent waves by small particles," *Applied Physics B: Lasers and Optics*, vol. 68, no. 1, pp. 87–92, 1999.

[84] V. Yannopapas and N. Vitanov, "Spontaneous emission of a two-level atom placed within clusters of metallic nanoparticles," *Journal of Physics: Condensed Matter*, vol. 19, p. 096210, 2007.

[85] J. Stratton, *Electromagnetic theory*. Wiley-IEEE Press, 2007.

[86] A. Narayanaswamy and G. Chen, "Direct computation of thermal emission from nanostructures," *Annual Reviews of Heat Transfer*, vol. 14, no. 14, 2005.

[87] R. Siegel and J. Howell, *Thermal radiation heat transfer*. Taylor & Francis, 2002.

[88] B. Derjaguin, "Untersuchungen über die Reibung und Adhäsion, IV," *Colloid & Polymer Science*, vol. 69, no. 2, pp. 155–164, 1934.

[89] H. Gies and K. Klingmüller, "Casimir effect for curved geometries: Proximity-force-approximation validity limits," *Physical Review Letters*, vol. 96, p. 220401, 2006.

[90] J. Blocki, J. Randrup, W. J. Swiatecki, and C. F. Tsang, "Proximity forces," *Annals of Physics*, vol. 105, pp. 427–462, 1977.

[91] C. Genet, A. Lambrecht, and S. Reynaud, "The casimir effect in the nanoworld," *The European Physical Journal-Special Topics*, vol. 160, no. 1, pp. 183–193, 2008.

[92] B. A. Todd and S. J. Eppell, "Probing the limits of the derjaguin approximation with scanning force microscopy," *Langmuir*, vol. 20, no. 12, pp. 4892–4897, 2004.

[93] S. K. Lamoreaux, "Demonstration of the casimir force in the 0.6 to $6\mu m$ range," *Physical Review Letters*, vol. 78, pp. 5–8, Jan 1997.

[94] U. Mohideen and A. Roy, "A precision measurement of the casimir force between 0.1 to $0.9\mu m$," *Phys. Rev. Lett.*, vol. 81, pp. 4549–4552, 1998.

[95] L. R. White, "On the deryaguin approximation for the interaction of macrobodies," *Journal of colloid and interface science*, vol. 95, no. 1, pp. 286–288, 1983.

[96] S. Bhattacharjee and M. Elimelech, "Surface element integration: A novel technique for evaluation of dlvo interaction between a particle and a flat plate," *Journal of colloid and interface science*, vol. 193, no. 2, pp. 273–285, 1997.

[97] J. Israelachvili, *Intermolecular and Surface Forces*. New York: Academic Press, 1991.

[98] S. Rentsch, R. Pericet-Camara, G. Papastavrou, and M. Borkovec, "Probing the validity of the derjaguin approximation for heterogeneous colloidal particles," *Physical Chemistry Chemical Physics*, vol. 8, no. 21, pp. 2531–2538, 2006.

[99] C. D. Fosco, F. C. Lombardo, and F. D. Mazzitelli, "Proximity force approximation for the casimir energy as a derivative expansion," *Physical Review D*, vol. 84, no. 10, p. 105031, 2011.

[100] L. Teo, M. Bordag, and V. Nikolaev, "Corrections beyond the proximity force approximation," *Physical Review D*, vol. 84, no. 12, p. 125037, 2011.

[101] G. Bimonte, T. Emig, R. L. Jaffe, and M. Kardar, "Casimir forces beyond the proximity approximation," *EPL (Europhysics Letters)*, vol. 97, no. 5, p. 50001, 2012.

[102] D. Krause, R. Decca, D. López, and E. Fischbach, "Experimental investigation of the casimir force beyond the proximity-force approximation," *Physical review letters*, vol. 98, no. 5, p. 050403, 2007.

[103] V. A. Golyk, M. Krüger, A. P. McCauley, and M. Kardar, "Small distance expansion for radiative heat transfer between curved objects," *EPL (Europhysics Letters)*, vol. 101, no. 3, p. 34002, 2013.

[104] N. Juul, "Investigation of approximate methods for calculation of the diffuse radiation configuration view factor between two spheres," *Letters in Heat and Mass Transfer*, vol. 3, no. 6, pp. 513–521, 1976.

[105] B. E. Sernelius, *Surface modes in physics*. Wiley-Vch, 2011.

[106] N. Gu, Z. Y. Sasihithlu, Karthik, and A. Narayansawamy, "Proximity approximation and radiative transfer between sub-wavelength spheres and planar surfaces," *Nanoletters*, under review (2013).

[107] W. A. Challener, C. Peng, A. V. Itagi, D. Karns, W. Peng, Y. Peng, X. Yang, X. Zhu, N. J. Gokemeijer, Y.-T. Hsia, G. Ju, R. E. Rottmayer, M. A. Seigler, and E. C. Gage, "Heat-assisted magnetic recording by a near-field transducer with efficient optical energy transfer," *Nat. Photonics*, vol. 3, pp. 220–224, 2009.

[108] S. Biehs and J. Greffet, "Influence of roughness on near-field heat transfer between two plates," *Physical Review B*, vol. 82, no. 24, p. 245410, 2010.